Piezoelectric ZnO nanostructures, synthesis and application for energy harvesting

Dissertation
zur Erlangung des Doktorgrades
der Naturwissenschaften

vorgelegt von
Farzaneh Fattahi Comjani
aus Esfahan

genehmigt von der
Fakultät für Natur- und Materialwissenschaften
der Technischen Universität Clausthal

Tag der mündlichen Prüfung:
24.07.2014

Vorsitzender der Prüfungskommission.....Prof. Dr. H. Fritze
Hauptberichterstatter.....Prof. Dr. W. Schade
Berichterstatter.....Prof. Dr. D. Schaadt

Die vorliegende Arbeit wurde im Zeitraum vom Oktober 2007 bis August 2013 am Institut für Energieforschung und Physikalische Technologien der Technischen Universität Clausthal und teilweise von August 2011 bis März 2013 am Fraunhofer Heinrich Hertz Institut in Goslar angefertigt.

To my parents

Abstract

Zinc oxide (ZnO) is a II-VI compound semiconductor with its unique optical, electrical, mechanical, thermal and chemical properties. The morphology of ZnO nanostructures has been proven to be the richest one among inorganic semiconductors. Based on the remarkable properties of ZnO and the motivation to miniaturize devices, large efforts have been recently focused on the synthesis, characterization and applications of nanostructures of ZnO in nanoscale technology and devices. This work in one part focuses on the synthesis of well aligned piezoelectric ZnO nanowires and their application as nanogenerator for harvesting energy from the environment. Here it is indicated that a Schottky contact at the ZnO-metal interface is not a necessity for the operation of a ZnO nanogenerator, as believed by now. However a Schottky contact leads to a more effective energy harvesting. In the other part of this work a new recipe for the synthesis of ZnO comblike-nanostructures by manipulating the Vapor-liquid-solid method is reported. These nanostructures are recently applied as nanocantilevers, UV nanolaser arrays, optical nanogratings and nanopolarizers. Moreover, a theoretical model for the growth of these structures is developed that explains for the first time the formation of these interesting nanostructures on the base of the piezoelectric property of ZnO. Applying the perturbation theory, the elasticity theory and using the Fourier expansion of mechanical stress exerted in the material under the growth kinetics, the induced piezoelectric charge in the nanostructure is approximated. The periodic distribution of the induced piezoelectric charge explains the periodic growth of nanowire branches of ZnO nanocombs on the polar +(0001) surface as a consequence of a self catalytic growth process. The Simulations show a good agreement between theoretical and experimental results.

Zusammenfassung

Zinkoxid (ZnO) ist ein II-VI Verbindungs-Halbleiter mit einzigartigen optischen, elektrischen, mechanischen, thermischen und chemischen Eigenschaften. Die Morphologie der ZnO-Nanostrukturen hat sich als die reichste unter den anorganischen Halbleitern herausgestellt. Basierend auf den bemerkenswerten Eigenschaften von ZnO und der Motivation, Geräte zu miniaturisieren, sind in letzter Zeit große Anstrengungen zur Synthese, Charakterisierung und Anwendung von ZnO-Nanostrukturen in Nanotechnologie und Nanogeräten unternommen worden. Diese Arbeit konzentriert sich in einem Teil auf die Synthese von gut ausgerichteten piezoelektrischen ZnO-Nanodrähten und ihre Anwendungen als Nanogenerator für die Energiegewinnung aus der Umwelt. Hier wird angedeutet, dass ein Schottky-Kontakt an der ZnO-Metall-Grenzfläche keine Notwendigkeit für den Betrieb eines ZnO-Nanogenerators ist, wie bis heute angenommen wurde. Allerdings führt ein Schottky-Kontakt zu einer effektiveren Energiegewinnung. Im anderen Teil dieser Arbeit wird ein neues Rezept für die Synthese von kammförmigen ZnO-Nanostrukturen durch Manipulation der Vapor-Liquid-Solid-Methode berichtet. Solche Nanostrukturen wurden vor kurzem als Nanocantilever, UV-Nanolaser-Arrays, optische Nanogitter und Nanopolarisatoren angewendet. Darüber hinaus wird ein theoretisches Modell für das Wachstum dieser Strukturen entwickelt, das zum ersten Mal die Bildung dieser interessanten Nanostrukturen auf Basis der piezoelektrischen Eigenschaft von ZnO erklärt. Durch Anwenden der Störungstheorie und der Elastizitätstheorie und mit Hilfe der Fourierentwicklung für die im Material unter der Wachstumskinetik ausgeübte mechanische Spannung wird die induzierte piezoelektrische Ladung in der Nanostruktur angenähert. Die periodische Verteilung der induzierten piezoelektrischen Ladung erklärt das periodische Wachstum von Nanodraht-Zinken des ZnO-Nanokamms auf der polaren +(0001) Oberfläche als Folge eines selbstkatalytischen Wachstumsprozesses. Die Simulationen zeigen eine gute Übereinstimmung zwischen theoretischen und experimentellen Ergebnissen.

Contents

1 Introduction

Zinc oxide (ZnO) is a II-VI compound semiconductor that has attracted intensive interest in research efforts. Its unique optical, electrical, mechanical, thermal and chemical properties enable versatile applications of ZnO in optoelectronic, piezotronic and piezophotonic devices. For example, ZnO has been used as an active channel in thin film transistors (TFTs) to achieve much higher field effect mobility than commercial amorphous silicon TFTs for display applications [BJN03, JN03]. As well, because of its large exciton binding energy of E=60 meV, ZnO can act as highly efficient and low lasing threshold UV emitter at room temperature [PY02]. Moreover, ZnO has been used as gas sensor for inflammable or toxic gases such as H_2, NH_3, C_2H_2OH, CO, and NO_2 [HWR03, XF10, DFP00, DG03, WJM02], also as pH sensor [BSK05] and optical sensor/photodetector [JDP08]. Furthermore, ultrasonic transducer arrays using ZnO thin films for operation at ν=100 MHz have been fabricated [YI92, YI95].

In addition to the pure ZnO, doped ZnO has recently attracted considerable attention due to its ferromagnetic and ferroelectric properties. For example, by introducing Mn as dopant in bulk ZnO, ferromagnetic ordering with Curie temperatures well above T=152 ℃ could be observed [PS03]. Vanadium doped ZnO films also have demonstrated ferromagnetic characteristics with a Curie temperature higher than T=77 ℃ [HS01]. Even in a recently published work the ferromagnetic nature of submicron sized nanorods of pure ZnO has been reported, which may be caused by singly charged oxygen vacancies in the nanorods [AK13]. Moreover, ferroelectric characteristics have been observed in Li doped ZnO thin films [MJ99, Dha06].

Based on these remarkable physical properties of ZnO and the motivation to miniaturize devices, large efforts have been focused on the synthesis, characterization and applications of nanostructures of ZnO in nanoscale technology and devices. The morphology of ZnO nanostructures has been proven to be the richest one among inorganic semiconductors [XF08]. Until now, abundant configurations such as nanowires, nanotubes, nanorings, nanohelices, nano-tetrapods, nanobelts, nanobridges, nanonails,

nanocombs and nanoplates have been successfully grown via a variety of methods including chemical vapor deposition [YFH10, JJW02], catalyst-driven molecular-beam-epitaxy [GPZ07], metal organic chemical vapor deposition [BPZ03, KO03], pulsed-laser deposition [AR07], sol-gel method [BBL97], electrodeposition [BP08], wet chemical methods [JXW06, YX09, JBB06], vapor-solid [BDY03, XYK03, GZS06] and vapor-liquid-solid methods [GZ12, MHH01b, PXG03, CJL02, SYL03]. These nanostructures, especially aligned ZnO nanowires have applications in optoelectronic devices [WYW11] and sensors [DP10]. The well aligned ZnO nanowires are promising optical resonance cavities which greatly facilitate highly directional UV lasing at room temperature [PY02, JCJ03, MHH01a, CL03]. Moreover, a ZnO nanowire is naturally a candidate as optical waveguide [Boe08] due to its nearly cylindrical geometry and large refractive index of $n \sim 2.0$. Furthermore, ordered ZnO nanowires have found applications for the fabrication of hybrid solarcells due to their unique semiconducting and optical properties.

Since 2006 a new potential application of ZnO nanostructures based on the piezoelectric effect for harvesting energy from the environment is introduced, which has been proposed as a promising means for self-powered nanosystems, in particular, for wireless nanodevices, nanosensors and biosensors. This is a key step towards developing an independent, reliable and sustainable unit for use in environments in which a dynamic compressive strain is available, such as in shoe pads, vehicle tires, under carpets or floors, in ocean waves [SX10], and even for use in the human body which provides also numerous potential mechanical energy, such as body movement, muscle stretching, blood vessel contraction, body fluid and blood flow.

Based on these remarkable potential applications the author was motivated to focuse on the synthesis of well aligned piezoelectric ZnO nanowires, their application as nanogenerator for harvesting energy from the environment and developement of new concepts for piezoelectric nanogenerators. On the way to achieve these aims, a new recipe for the synthesis of ZnO nanocombs was also obtained [FFC13a]. These nanostructures have application in nanoscale functional devices such as nanocantilevers [ZLW03], UV nanolaser arrays [HY03], optical nanogratings and nanopolarizers [ZWP05, KY08a]. Moreover, a model for the growth of these structures was developed that explains the formation of these interesting nanostructures on the base of the piezoelectric property of ZnO too [FFC13b].

The piezoelectric effect as the basic phenomenon on which the present work is constructed and the fundamental relations describing the electromechanical interaction in ZnO nanostructures are explained in chapter 2. The crystal and band structures of ZnO are

also reviewed in this chapter to provide a deeper understanding of the electromechanical interaction processes in the material. Among the numerous synthesis methods mentioned above, three ones including the vapor-liquid-solid (VLS), the electrochemicaldeposition (ECD), and the wet chemical methods were used in this work to produce ZnO nanostructures. These are explained in chapter 3. Especially, the wet chemical method is studied in more detail in chapter 3 because of its promising advantages over the other methods. This method was also advanced for the fabrication of ZnO nanogenerators and is later described in chapter 5. In chapter 4, the common methods for the synthesis of ZnO nanocombs are introduced. Then the synthesis of these structures by the VLS methode with a non-conventional molar ratio of the source material (ZnO: C) is reported. Moreover, a model for the growth of nanocombs based on the piezoelectric property of ZnO is developed. This model gives further insight into the interaction between the growth parameters, which may be important to control the growth process of nanocombs and consequently to develop the nanoscale functional devices based on them. In chapter 5, at first the current concepts of piezoelectric ZnO nanogenerators, their reported fabrication methods and proposed working mechanisms are introduced. Then the fabrication of new ZnO nanogenerators by the advanced wet chemical method is reported. The advantages of this fabrication method, especially for the control of transport properties of the ZnO-metal contacts are also discussed [FFC14]. At the end, the achieved results in this work are summerized in chapter 6 and an outlook for further studies and new potential applications of ZnO nanostructures is given.

2 Basic properties of ZnO Nanostructures

In this chapter, the basic properties of ZnO nanostructures are described. An insight into the crystal and band structure of ZnO allows a deeper understanding of the electromechanical interaction processes in ZnO as a piezoelectric material. Here the piezoelectric effect is considered. The fundamental piezoelectric relations describe the behavior of electromechanically interacting ZnO nanostructures and explain the experimental measurements in the next chapters. Since the fundamental piezoelectric relations are derived from thermodynamic considerations, the thermoelectric (pyroelectric) and thermoelastic coupling are considered in this chapter too.

2.1 Crystal and band structure

Zinc oxide (ZnO) is a `II-VI` compound semiconductor. Most of the group `II-VI` compound semiconductors crystallize in either cubic zinc blende or hexagonal wurtzite structure where each anion is surrounded by four cations at the corners of a tetrahedron, and vice versa. This tetrahedral coordination is typical of sp^3 covalent bonding nature, but these materials also have a substantial ionic character that tends to increase the bandgap beyond the one expected from the covalent bonding [HM09]. In other words, the chemical bonding in these materials has a mixed covalent/ionic nature. As schematically shown in Figure 2.1, ZnO can crystallize in wurtzite, zinc blende, and rocksalt (or Rochelle salt) phases.

The wurtzite structure with C_{6v}^4 crystal symmetry, is the thermodynamically stable phase of the ZnO crystal and energetically favorable compared to the zinc blende and rocksalt forms. Figure 2.2a shows the wurtzite structure of ZnO, which consists of hexagonal Zn and O basal planes stacked alternately along the c-axis. The lattice constants are $a = 0.325$ nm and $c = 0.521$ nm [OD02]. The internal parameter u ($u = b/c$) is defined as the length b of the anion-cation bond divided by the lattice constant c ($u = 0.375$ in an ideal wurtzite structure [HM09]). The important surfaces and directions in the wurtzite phase are shown in Figure 2.2b.

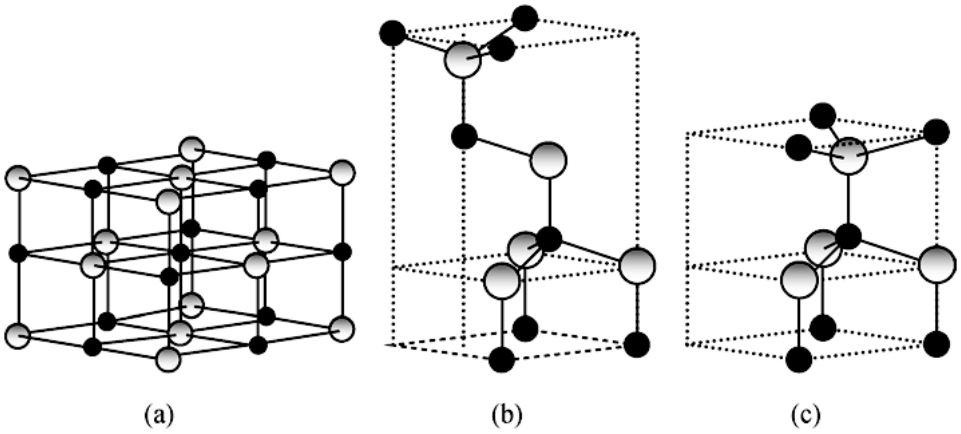

Figure 2.1: Representation of ZnO crystal structures: (a) cubic rocksalt, (b) cubic zinc blende, and (c) hexagonal wurtzite. Shaded gray and black spheres denote Zn and O atoms, respectively [HM09].

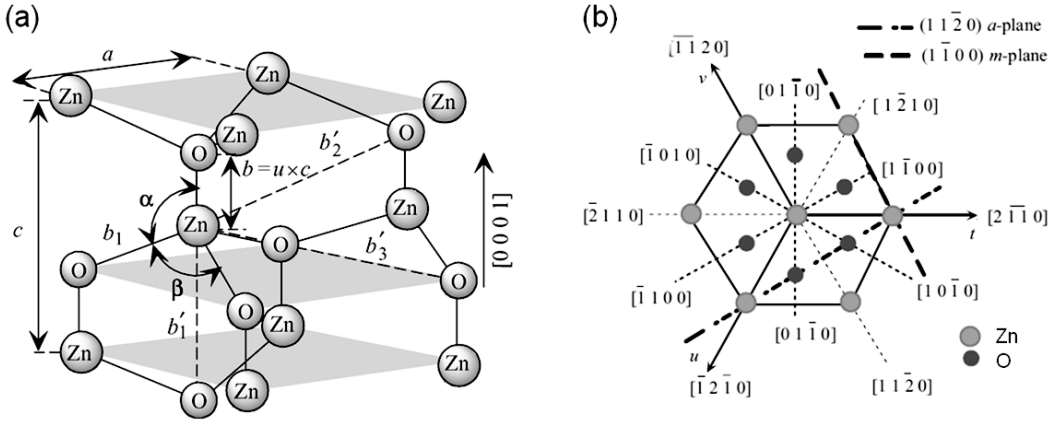

Figure 2.2: (a) Schematic representation of the wurtzite structure of ZnO. a and c are the lattice constants in the basal plane and in the basal direction, respectively. b is the nearest-neighbor distance or the bond length and b'_1, b'_2, and b'_3 show the three types of second-nearest-neighbor distances. The bond angles are shown with α and β (109.47° in an ideal crystal). (b) Common orientations in the wurtzite phase. The $(11\bar{2}0)$ and $(1\bar{1}00)$ planes and associated directions are shown as projections on the (0001) basal plane [HM09].

ZnO in zinc blende structure (Figure 2.1b) with T_d^2 crystal symmetry is metastable. ZnO in zinc blende form can be stabilized by heteroepitaxial growth on cubic substrates, such as Pt, Ti, Si and SiO_2 [SKK03]. The wurtzite and zinc blende structures differ only in the bond angle of the second-nearest neighbors and, therefore, in the stacking sequence of close-packed diatomic planes. The wurtzite structure consists of triangularly arranged alternating basal planes (0001) along the [0001] direction. In contrast, the zinc blende structure exhibits a 60° rotation along the $[11\bar{2}1]$ direction and, therefore, consists of triangularly arranged alternating planes along the $[11\bar{2}1]$ direction.

The rocksalt or Rochelle salt (NaCl) structure (Figure 2.1a) with O_h^5 crystal symmetry is a metastable phase of ZnO. Wurtzite ZnO can be transformed to the rocksalt structure at enough external hydrostatic pressures. This is connected to the covalent/ionic nature of the chemical bond in ZnO. Actually, the reduction of the lattice dimensions raises the ionic contribiution to the chemical bonding [HK96]. However, the rocksalt structure cannot be stabilized by epitaxial growth. The pressure-induced phase transition from the wurtzite to the rocksalt phase occurs in the range of 9 GPa for increasing pressure and causes a large decrease in volume of about 17% [Des98]. Energy-dispersive X-ray diffraction (EDXD) measurements have shown that when the external pressure is released a fraction of the rocksalt metastable phase is retained even at zero pressure [JMR98]. The phase transition shows a hysteresis behavior. The transition pressure (from the wurtzite to the rocksalt) is about 9 GPa for increasing pressure whereas that is (from the rocksalt to the wurtzite) about 2 GPa for decreasing pressure [Des98]. Theoretical calculations suggest that ZnO would undergo another phase transformation from the cubic rocksalt (NaCl) to the cubic cesium chloride (cubic CsCl) structure at sufficiently high pressures. However, the CsCl phase has yet to be experimentally observed. The transition pressure from NaCl phase to CsCl phase was predicted for 260 GPa [JEJ00] or 352 GPa [AZ02].

None of the three crystal structures described above have an inversion center. The (0001) basal planes differ from $(000\bar{1})$ in the hexagonal wurtzite structure (see Figure 2.2) and therefore, ZnO exhibits a crystallographic polarity along the [0001] direction. In the cubic zinc blende and rocksalt structures the close-packed $(11\bar{2}1)$ planes differ from the $(\bar{1}\bar{1}2\bar{1})$, and therefore, ZnO shows a polarity along the $[11\bar{2}1]$ direction. Many properties of the material depend also on its polarity, for example, growth, defect generation, elasticity, pyro- and piezoelectricity. The wurtzite ZnO is energetically favorable compared to zinc blende and rocksalt forms. Hence most commonly ZnO grows in the wurtzite structure. In addition, ZnO wurtzite crystals grow anisotropically due to the different surface energies

of the crystal planes [OD02, BM03]. The surface/cleavage energy for the basal planes of wurtzite ZnO are given in Table 2.1. A comparison between the surface energies suggests that the polar (0001) planes are the least stable faces of wurtzite ZnO. Therefore, most commonly the ZnO nanostructures grow fastest in direction [0001] and have only small polar (0001) surfaces.

The simplified band structure of wurtzite ZnO is schematically represented in Figure 2.3. The valence band consists of three closely spaced states named the A, B, and C bands, resulting from the spin-orbit coupling and crystal field [BKM04, AM95]. As shown in Figure 2.3, there is a direct bandgap of E_G=3.4376 eV between the upper valence band A and the conduction band [DCR99, BKM04]. A more complex band structure of wurtzite ZnO is also represented in Figure 2.4a. The first two conduction band states (in the range of E=0 eV–E=8 eV) are strongly Zn localized and correspond to empty Zn 3s levels. The bottom 10 valence bands (in the range of E=-7 eV–E=-5 eV) shown as a dashed band in this Figure, correspond to Zn 3d levels and the upper 6 valence bands (in the range of E=-5 eV–E=0 eV), including the C, B, and A bands, correspond to O 2p bonding states. As mentioned already, ZnO in the wurtzite phase has a bandgap of E_G=3.4376 eV. The bandgap shrinks with increasing temperature [REM06, KPD91], but shows a sublinear increase with increasing hydrostatic pressure [AM95].

Jaffe et al. [JEJ00] have calculated the band structure of ZnO for different phases (Figure 2.4). When wurtzite ZnO is compressed, the peak at the top of the upper valence band is slightly flattened and shifted down in energy, the O 2s- and Zn 3d-derived peaks are slightly broadened and shifted up in energy, and a splitting appears in the Zn 3d states. At the transition pressure p_{T1} from wurtzite to rocksalt (NaCl) structure, significant changes occur. In particular, the peak near the valence band maximum is greatly reduced in height. Further compression of the NaCl phase in the range p_{T1} to p_{T2} results in a large splitting of the Zn 3d peak. The O 2s-derived band moves greatly down in energy and broadens and, therefore, the fundamental bandgap increases with increasing pressure. At

Table 2.1: Surface/cleavage energy of basal planes of wurtzite ZnO [BM03].

Basal plane	Polarization	Surface energy (J/m^2)
(0001)	polar	4.3
$(11\bar{2}0)$	nonpolar	2.5
$(10\bar{1}0)$	nonpolar	2.3

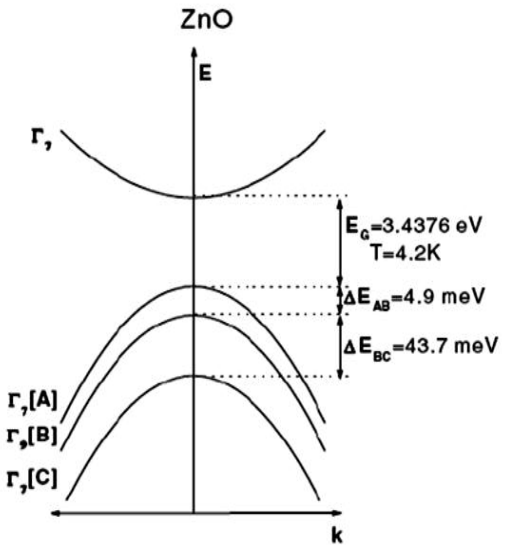

Figure 2.3: Band structure of hexagonal wurtzite ZnO. The splitting into three valence bands (A, B, C) is caused by crystal field and spin-orbit splitting [BKM04].

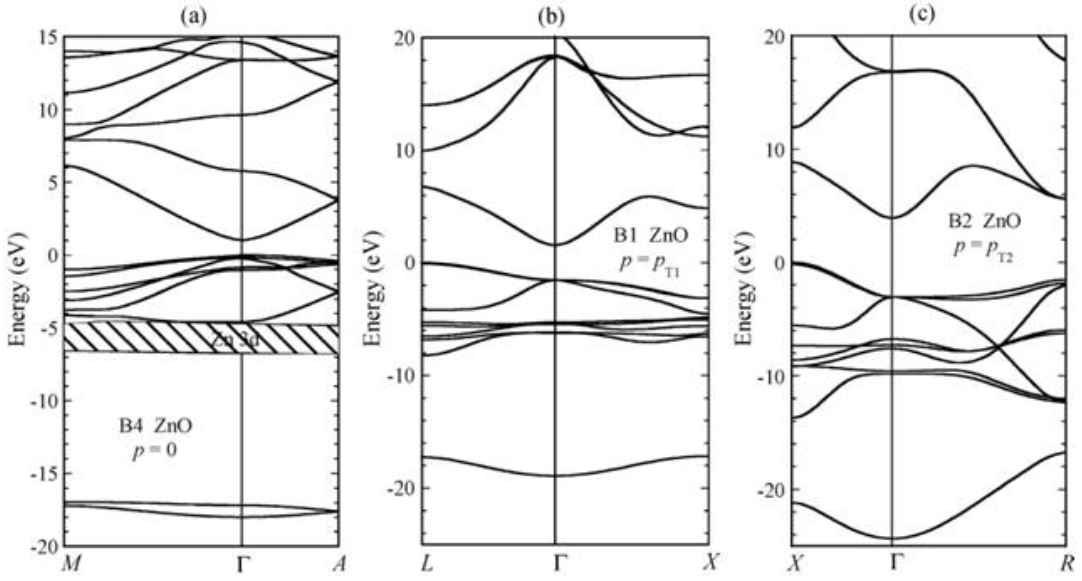

Figure 2.4: Band structure for ZnO: (a) Wurtzite structure without hydrostatic pressure, (b) NaCl structure at $p = p_{T1}$, (c) CsCl structure at $p = p_{T2}$ [JEJ00].

the transition pressure p_{T2} from NaCl to CsCl structure, the upper valence bandwidth remains almost unchanged but the peak near the valence band maximum reappears. The structure of the Zn 3d states changes radically with the O 2p-derived states because of heavy hybridization, and the O 2s-derived states broaden further and shift up in energy [HM09].

In addition to the pressure dependence, the bandgap of wurtzite ZnO depends also on the size of the crystal structure. The bandgap increases with decreasing diameter of the ZnO nanowire [Hei10]. This suggests that the dielectric constant of ZnO decreases with decreasing diameter of the ZnO nanowire too. Yang et al. [YY12] observed a decrease of the dielctric constant from k=6.4 to $k = 2.7$ with diameters decreasing from D=285 nm to D=85 nm using scanning conductance microscopy (SCM). These values are much smaller than that of bulk ZnO (k=8.66) [YY12].

2.2 Piezoelectricity

Piezoelectricity is a linear interaction between electrical and mechanical systems. The piezoelectric effect can convert a mechanical vibration into an electric signal or vice versa. Pierre and Jacques Curie first observed the direct and inverse piezoelectric effect in 1880 and 1881 [Ike90]. In the direct piezoelectric effect, an electric polarization is produced by mechanical stress at an ionic crystal lacking a center of symmetry. In the inverse piezoelectric effect, the crystal becomes strained when an electric field is applied. A simplified model of piezoelectricity involves the concept of anions and cations moving in opposite directions under the influence of an electric field or mechanical force. This motion leads to deformation of the crystal lattice.

As mentioned already, ZnO forms a wurtzite structure with the C_{6v}^4 crystal symmetry. Thus it possesses no center of symmetry which is required for piezoelectric materials. Figure 2.5a shows schematically what happens when a tetrahedrally coordinated cation-anion unit of the wurtzite structure is deformed. As a mechanical stress is applied to the unit, the anions and cations are shifted and hence a potential difference develops. ZnO is a semiconductor material, which has a relatively high electromechanical coupling coefficient. This makes ZnO an excellent material to use in a wide variety of piezoelectric applications. The piezoelectric coefficient of an individual (0001) surface dominated zinc oxide nanobelt was measured by Zhao et al. [MHZ04] by atomic force microscopy using a conductive tip. On the basis of references of bulk (0001) ZnO and x-cut quartz, the effective piezoelectric

coefficient d_{33} of ZnO nanobelts with typical dimension of tens of nanometers in thickness, hundreds of nanometers in width, and tens of micrometers in length was found to be frequency dependent and varied from d_{33}=14.3 pm/V to d_{33}=26.7 pm/V (Figure 2.5b), which is much larger than the value for bulk (0001) ZnO of d_{33}=9.93 pm/V. This suggests applications of ZnO nanobelts as nanosensors and nanoactuators.

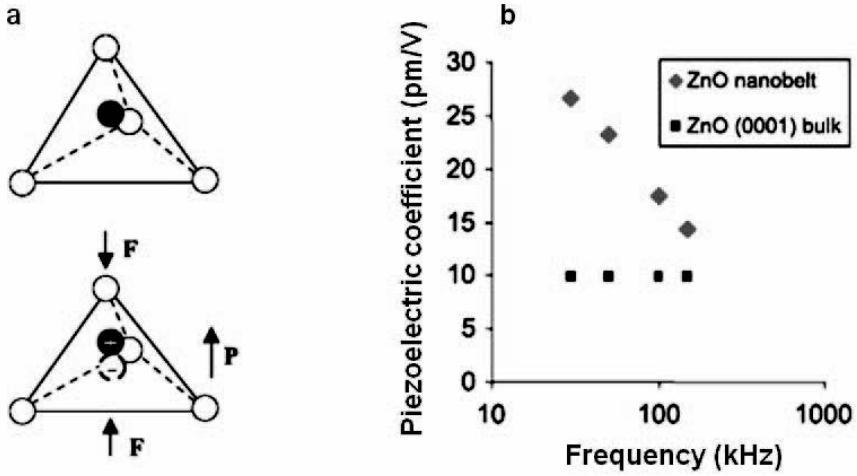

Figure 2.5: (a) Schematics showing piezoelectric effect in a tetrahedrally coordinated cation-anion unit [Wan07]. (b) Experimentally measured piezoelectric coefficient d_{33} for ZnO and its comparison to that of the bulk [MHZ04].

2.3 Pyroelectricity

Pyroelectricity is a linear interaction between electrical and thermal systems. This effect was observed before the discovery of the piezoelectricity in 1824 by Brewster. In the direct pyroelectric effect, an electric polarization is produced by heating certain crystals. Crystals can only be pyroelectric if they possess no center of symmetry. The pyroelectric effect can convert thermal vibrations into electric signals and vice versa. In the inverse effect named the electrocaloric effect, the crystal becomes heated when an electric field is applied.

ZnO is also a pyroelectric matrial due to its crystal symmetry. Yang et al. [YY12] have reported pyroelectric current and voltage coefficients of 1.2-1.5 nC/cm^{2}K and $2.5 - 4.0 \times 10^4$V/mK for an array of ZnO nanowires, respectively. The former value is larger than those reported for ZnO bulk (0.94 nC/cm^{2}K) and film (1.0 nC/cm^{2}K) materials [Lan05, Coo62]. The enhancement of the pyroelectric coefficients in ZnO nanowire arrays as

compared to that in bulk ZnO is likely due to the single crystalline structures with the same preferred orientations along the c-axis and less dislocation density [YY12]. Pyroelectric ZnO nanowire arrays can be used for harvesting thermal energy in our environment for applications such as wireless sensors, temperature imaging, medical diagnostics, and personal microelectronics [YY12].

Pyroelectricity can be considered as a secondary piezoelectric effect and a thermal expansion too. Figure 2.6 (Heckmann-Diagramm) shows possible linear interaction processes between any two of the three electrical, mechanical, and thermal systems [Ike90]. Quantities that do not depend on the system size or the amount of material in the system (temperature Θ, mechanical stress $\vec{T}$, electric Field $\vec{E}$) are shown at the vertices of the outer triangle and those dependent on the respective system (entropy σ, mechanical strain $\vec{S}$, electric displacement field $\vec{D}$) at the vertices of the inner triangle. A line connecting either two indicates coupling between the respective variables. An unprimed notation indicates a direct effect and a primed one a inverse effect.

The fundamental piezoelectric relations describing the electromechanical coupling in systems can be derived from thermodynamic considerations:

The state equation of a thermal system with no coupling with another mechanical or electrical system, is expressed as

$$\delta\sigma = (\rho C/\Theta)\delta\Theta \tag{2.1}$$

where C is specific heat per unit mass and ρ is density. The state equation of an electrical system is given by

$$D_i = \varepsilon_{ij} E_j \quad or \quad E_i = \beta_{ij} D_j \tag{2.2}$$

where ε and β are second-rank tensors of dielectric constant and dielectric impermeability, respectively. For a mechanical system, the state equation is given by

$$T_{ij} = c_{ijkl} S_{kl} \quad or \quad S_{ij} = s_{ijkl} T_{kl} \tag{2.3}$$

here c is the elastic stiffness constant and s is the elastic compliance coefficient. The constants c and s are fourth-rank tensors and both $\vec{T}$ and $\vec{S}$ are polar tensors of second rank. In the interaction processes, the above constants are not independent any more and the coupling systems are described with a set of constitutive relations. The Gibbs free

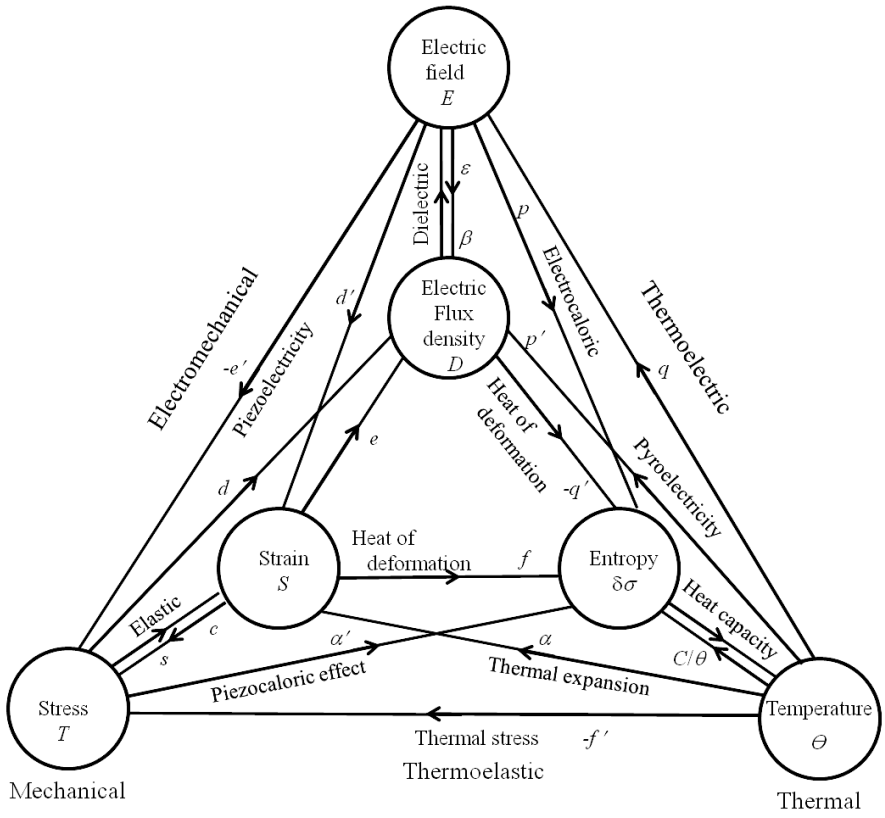

Figure 2.6: Interaction processes between the electrical, mechanical, and thermal systems [Ike90].

energy G per unit volume is expressed as

$$G = U - \Theta\sigma - T_{ij}S_{ij} - E_n D_n \tag{2.4}$$

where the internal energy U is a function of σ, $\vec{S}$, and $\vec{D}$. The exact differential of the Gibbs energy density is written as

$$dG = -\sigma d\Theta - S_{ij}dT_{ij} - D_n dE_n \tag{2.5}$$

From this equation one obtains [Ike90]

$$\sigma = -\left[\frac{\partial G}{\partial \Theta}\right]_{T,E}, \quad S_{ij} = -\left[\frac{\partial G}{\partial T_{ij}}\right]_{\Theta,E}, \quad D_n = -\left[\frac{\partial G}{\partial E_n}\right]_{\Theta,T} \tag{2.6}$$

here indices represent the relevant constant variables. By expanding the function G (equation (2.4)) with respect to $\delta\Theta$, T_{ij}, and E_n and using equation (2.6) one obtains the following constitutive relations

$$\delta\sigma = (\rho C^{T,E}/\Theta)\delta\Theta + \alpha_{ij}^{E} T_{ij} + p_m^T E_m, \tag{2.7}$$

$$S_{ij} = \alpha_{ij}^{E}\delta\Theta + s_{ijkl}^{E,\Theta} T_{kl} + d_{mij}^{\Theta} E_m, \tag{2.8}$$

$$D_n = p_n^T\delta\Theta + d_{nkl}^{\Theta} T_{kl} + \varepsilon_{nm}^{T,\Theta} E_m \tag{2.9}$$

in which

$$s_{ijkl}^{E,\Theta} = \left[\frac{\partial S_{ij}}{\partial T_{kl}}\right]_{E,\Theta}, \qquad \varepsilon_{nm}^{\Theta,T} = \left[\frac{\partial D_n}{\partial E_m}\right]_{T,\Theta}, \qquad \frac{\rho C^{T,E}}{\Theta} = \left[\frac{\partial \sigma}{\partial \Theta}\right]_{T,E}, \tag{2.10}$$

and the piezoelectric coefficient d, the pyroelectric coefficient p, and the thermal expansion coefficient α are defined as

$$d_{nij}^{\Theta} = \left[\frac{\partial D_n}{\partial T_{ij}}\right]_{E,\Theta} = \left[\frac{\partial S_{ij}}{\partial E_n}\right]_{T,\Theta}, \tag{2.11}$$

$$\alpha_{ij}^{E} = \left[\frac{\partial S_{ij}}{\partial \Theta}\right]_{T,E} = \left[\frac{\partial \sigma}{\partial T_{ij}}\right]_{E,\Theta}, \tag{2.12}$$

$$p_n^T = \left[\frac{\partial D_n}{\partial \Theta}\right]_{T,E} = \left[\frac{\partial \sigma}{\partial E_n}\right]_{T,\Theta}. \tag{2.13}$$

The three constitutive relations (equations (2.7)-(2.9)) are the fundamental equations describing the coupling processes in systems. For a pure electromechanical coupling ($\delta\sigma = 0$ and $\delta\Theta = 0$) these are simplified to the common piezoelectric equations

$$S_{ij} = s_{ijkl}^{E,\Theta} T_{kl} + d_{mij}^{\Theta} E_m, \tag{2.14}$$

$$D_n = d_{nkl}^{\Theta} T_{kl} + \varepsilon_{nm}^{T,\Theta} E_m. \tag{2.15}$$

These equations will be used in section 4.3, where a model for the growth of ZnO comb-like nanostructures based on the piezoelectric effect is developed and explain also the function mechanism of ZnO nanogenerators reported in chapter 5.

3 Synthesis of ZnO nanostructures

ZnO nanostructures with abundant configurations [Wan04] such as nanowires, nanotubes, nanohelices, nanobelts, and nano-tetrapods can be synthesized by various methods, including chemical vapor deposition (CVD) [YFH10, JJW02], catalyst-driven molecular-beam-epitaxy (MBE) [GPZ07], metal organic chemical vapor deposition (MOCVD) [BPZ03, KO03], pulsed-laser deposition [AR07], sol-gel methods [BBL97], electrodeposition [BP08], wet chemical methods [JXW06, YX09, JBB06], vapor-solid (VS) [BDY03, XYK03, GZS06] and vapor-liquid-solid (VLS) methods [GZ12, MHH01b, PXG03, CJL02, SYL03]. In this chapter, the synthesis of ZnO nanostructures by vapor-liquid-solid (VLS), electrochemical deposition (ECD), and wet chemical methods are reported, which were available within the facilities at the Clausthal University of Technology. The main focus is on the wet chemical method, due to its promising advantages, specially, for advancement of the ZnO nanogenerators explained in chapter 5.

3.1 Vapor-liquid-solid method

The most common method to synthesize ZnO nanostructures utilizes a vapor transport process. Vapor transport processes can be categorized into the catalyst free vapor-solid (VS) and catalyst assisted vapor-liquid-solid (VLS) process. In a typical VS or VLS process, ZnO powder reduces to oxygen and Zn vapor at about T_2=1400 ℃. A carrier gas (Ar or N_2) transports the vapors and nanostructures are deposited on a substrate in a low temperature zone at T_3=400 ℃–T_3=500 ℃ (Figure 3.1).

A rich variety of nanostructures, including nanowires, nanorods, nanohelixes and nanobelts can be synthesized by the VS process [XYK03, BDY03, GZS06]. However, the VS method provides little control on the morphology, position and alignment of synthesized ZnO nanostructures. Controlled growth of ZnO nanostructures were achieved by catalyst assisted VLS processes [PY02, SYL03, MHH01b, JS05]. Various nanoparticles or nanoclusters of Au [MHH01b], Cu [SYL03], Sn [PXG03] and Co [CJL02] were used as

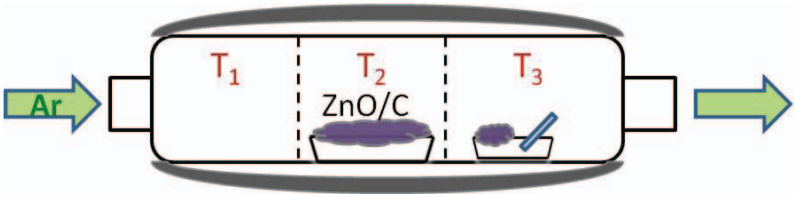

Figure 3.1: Schematic of the VLS process to synthesize ZnO nanowires in a horizontal three-zone furnace. The ZnO or ZnO/C powder mixture reduces to Zn and O_2/CO vapor in the center of the furnace at the temperature T_2. The Ar carrier gas transports the vapors and ZnO crystalizes on the substrate in the downstream zone at the temperature T_3 (T_3<T_2).

catalysts by the VLS method. The catalyst nanoparticles are the preferential nucleation centers for the growth of ZnO nanostructures on the substrates. Figure 3.2 shows a schematic of a typical VLS process.

Usually ZnO powder is mixed with graphite powder with a molar ratio ZnO: C (1: 1) as source material. The graphite significantly lowers the decomposition temperature of ZnO. At temperatures above T_2=800 ℃–T_2=1300 ℃, graphite reduces ZnO to Zn and CO vapor. Zn vapor and Au nanoparticles form an eutectic liquid alloy. After saturation of Zn in the alloy particles, Zn and CO react and ZnO nuclei crystallize under the alloy particles on the substrate. The following chemical reactions take place during the growth

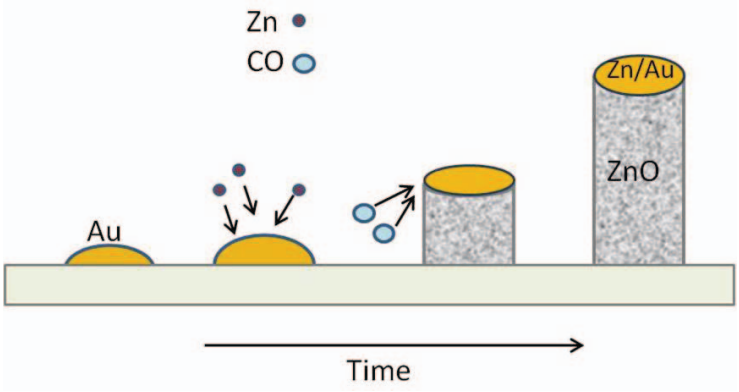

Figure 3.2: Schematic of the VLS growth process for synthesis of ZnO nanowires (with inspiration from ref. [Boe08]).

process by the VLS method [SYL03]:

$$ZnO + C \rightarrow Zn + CO, \tag{3.1}$$

$$Zn + CO \rightarrow ZnO + C. \tag{3.2}$$

By the VLS process the metal catalyst nanoparticles usually stay at the tips of the synthesized ZnO nanostructures. The size of catalyst nanoparticles determines the diameter of the nanowires. Hence using different sizes of catalyst nanoparticles one can control the size of grown nanowires [PY02]. In addition, choosing proper epitaxy substrates and using patterning techniques such as photolithography, electron beam lithography, and shadow masks one can control the position, orientation and alignment of the grown nanowires on the substrates [HC02, HJF04, ECG04]. Figure 3.3 shows a sapphire (0001) substrate, which is patterned in squares of 6 µm × 6 µm of Au catalyst using the photolithography technique. Then ZnO nanowires were grown from the patterned catalysts by the VLS process in the three-zone furnace at T_2 =1130 ℃ for t=35 minutes (see Figure 3.1 too). The quality of the alignment of ZnO nanowires is mainly determined by the lattice mismatch between ZnO and the substrate [PY02, HJF04]. Figure 3.4 shows the aligned ZnO nanowires grown on sapphire $(11\bar{2}0)$, SiO_2 (0001), and Si $(11\bar{2}1)$ substrates. Due to its small lattice mismatch of 0.08% [CJL02], sapphire $(11\bar{2}0)$ is a more suitable epitaxy substrate for the vertical growth of ZnO nanowires than the other ones.

Vertically aligned ZnO nanowires have promising applications such as UV nanolaser array [HY03, PY02], field-effect transistor, and nanogenerators. The VLS process is the dominant synthesis method for growing ZnO nanowires. However, due to its high synthesis temperature (typically about T_2=1300 ℃), the growth process is limited to certain substrates, which have a high melt temperature above the synthesis temperature. In the next sections, two other growth methods will be introduced, which provide the possibility of synthesis of ZnO nanostructures at low temperatures, and therefore, more options of substrate material and low energy consumption.

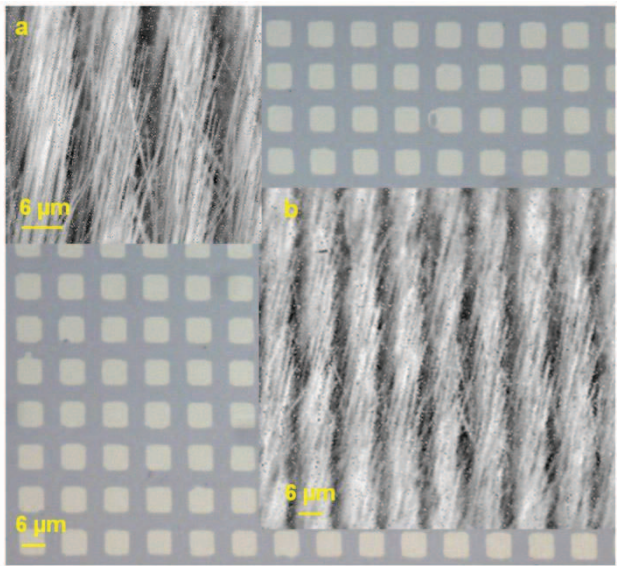

Figure 3.3: ZnO nanowire array grown on a patterned Au-catalyzed sapphire (0001) substrate by the VLS method in the three-zone furnace at T_2 =1130 ℃ for t=35 minutes. a and b are top view of SEM images of the grown nanowires in two enlargements.

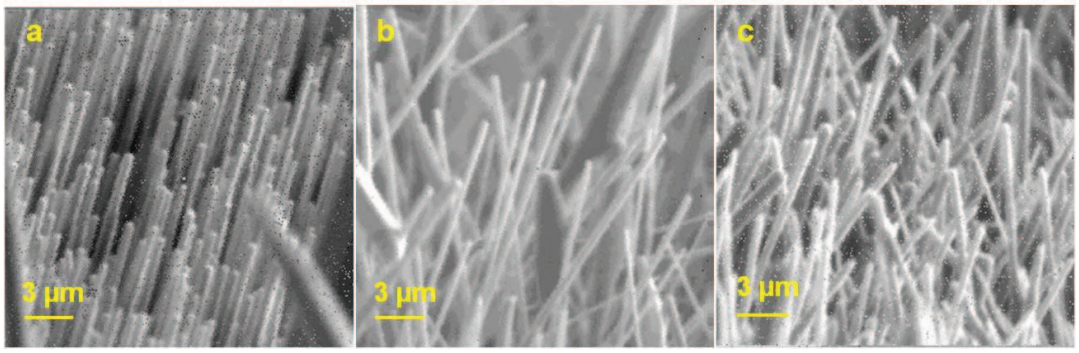

Figure 3.4: SEM images of aligned ZnO nanowires synthesized by the VLS method on a (a) sapphire $(11\bar{2}0)$ (b) SiO_2 (0001) and (c) Si $(11\bar{2}1)$ substrate. The substrates were tilted by 30°.

3.2 Electrochemical deposition process

Among numerous deposition techniques, electrochemical deposition (ECD) has attracted considerable attention for the growth of ZnO nanowires and nanotubes due to its simplicity, relative low synthesis temperatures, possibility of large-area deposition, and cost-efficiency. Wurtzite ZnO nanowires were grown at low temperatures (typically T=85 °C) on a transparent conducting oxide (TCO) such as ITO film [OL10, MG08] and SnO_2 : F film [JE07] on glass substrates for photovoltaic applications or on sapphire [KK04] and GaN [TP06] films for UV laser emitters.

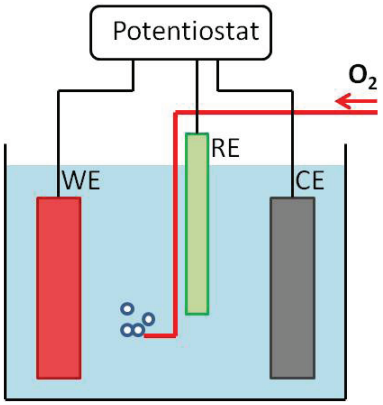

Figure 3.5: Schematic of three-electrode electrochemical cell for the electrochemical deposition of ZnO nanowires. The potentiostat creates a constant electric potential between the cathode (WE) and anode (CE). No current flows through the reference-electrode (RE).

Figure 3.5 schematically shows the three-electrode electrochemical cell for the electrochemical deposition of ZnO nanowires at temperatures below T=100 °C. Using a potentiostat/galvanostat a constant electric potential between the work-electrode (WE) and counter-electrode (CE) can be established. The potential of the reference-electrode (RE) stays constant and no current flows through it during the growth process. An aqueous solution from zinc chloride ($ZnCl_2$) and potassium chloride (KCl) is employed as electrolyte. The electrolyte is saturated with pure oxygen by bubbling before starting the electrolysis and continuously during of the growth process [OL10]. The growth mechanism of ZnO nanowires on the cathode surface is schematically shown in Figure 3.6 [JE08]. In the electrolyte, O_2 molecules diffuse to the cathode (WE) and reduce to OH^- ions by a two or a four electron process, as a function of the electrolyte and cathode properties. Then

Zn^{2+} and OH^- ions react together and ZnO deposites on the cathode surface. The crystal growth of ZnO nanowires involves the following chemical reactions [JE07, JE08, MG08]:

$$O_2 + 2H_2 + 4e^- \rightarrow 4OH^-, \tag{3.3}$$

$$O_2 + 2H_2O + 2e^- \rightarrow H_2O_2 + 2OH^-, \tag{3.4}$$

$$Zn^{2+} + 2OH^- \rightarrow ZnO + H_2O, \tag{3.5}$$

$$Zn^{2+} + 2OH^- \rightarrow Zn(OH)_2, \tag{3.6}$$

$$Zn(OH)_2 \rightarrow ZnO + H_2O. \tag{3.7}$$

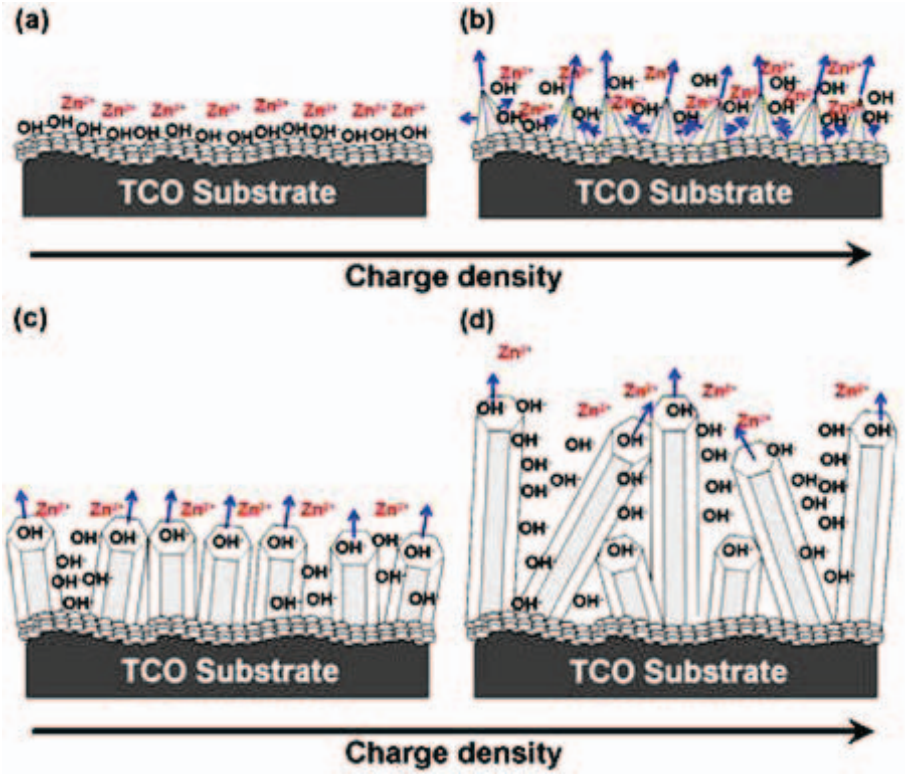

Figure 3.6: Schematic of the growth mechanism of ZnO nanowires by the ECD process. The blue arrows indicate the growth direction. In (b) the length of the arrows is proportional to the growth rate. The charge density increases during the growth process from (a) to (b), (c), and (d), respectively [JE08].

Figure 3.7b shows SEM images of grown ZnO nanowires on a FTO glass (fluorine doped tin oxide glass) in an electrolyte from 0.5 mM $ZnCl_2$ and 0.1 M KCl at an electric potential

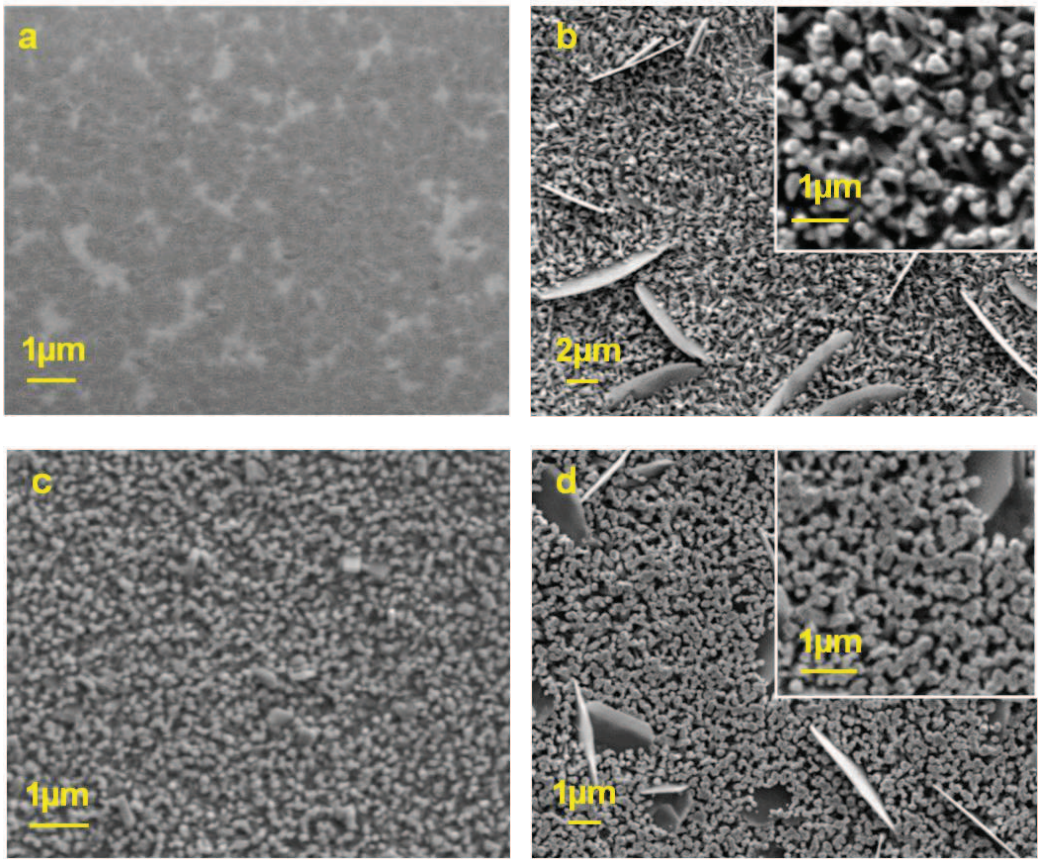

Figure 3.7: SEM images of (a) spin coated seed layer of ZnO nanoparticles on a FTO glass. (b) Grown ZnO nanowires by the ECD method on the nanoparticle seed layer of (a). (c) Seed layer of ZnO nanowires synthesized by the wet chemical method on a FTO glass. (d) Grown ZnO nanowires by the ECD method on the nanowired seed layer of (c). The quality of the alignment of ZnO nanowires is determined by the seed layer.

of U= -0.7 V. The temperature was T=82 ℃ during the growth process for t=11500 seconds. Before starting the electrodepositon process, the substrate was coated with a seed layer of ZnO nanoparticles, which results in the growth of better aligned and denser ZnO nanowires. The seed layer was realized by spin coating 10 µl of a 0.01 M nanoparticle solution from lithium hydroxide (LiOH) and zinc acetate dihydrate $[Zn(CH_3COO)_2]2H_2O$ in ethanol on the substrate with a surface area of 1 cm × 1 cm and a rotation velocity of 30 rpm for t=3 minutes. The nanoparticles form a relative inhomogeneous seed layer, as shown in Figure 3.7a. The quality of the alignment of ZnO nanowires is mainly determined

by the seed layer [JE07]. Figure 3.7d shows the vertically aligned ZnO nanowires grown by the ECD process on a seed layer of small ZnO nanowires. The small ZnO nanowires with an average diameter of D=100 nm and length of L=300 nm were synthesized by another wet chemical methode (refer to the next section) on the FTO glass substrate (Figure 3.7c). For this the substrate was put in a 0.1 M aqueous solution from zinc nitrate hexahydrate ($Zn(NO_3)_26H_2O$) and hexamin at T=88 ℃ for t=3 hours. Then the substrate was washed with distilled water and dried under a flow of nitrogen gas. The as-grown ZnO nanowires form a relative homogeneous seed layer for the homoepitaxy by the following ECD process. However, besides the ZnO nanowires, ZnO sheets also grow on both seed layers. This could be caused by relative low conductivity of the FTO glass substrate with a surface resistance of 25 Ωcm^{-1}. The controlling of growth parameters, i.e., process temperature, electrolyte concentration, electrodeposition potential, and electrodeposition time result in different sizes and morphologies of grown nanowires [JE07, KK04, OL10, TP06, MG08].

Although the electrochemical deposition is an attractive method for growing ZnO nanowires due to its advantages of large-area deposition, low synthesis temperature, and therefore cost-efficiency, it is limited to certain conductive substrates, which are chemically stable in the electrolyte solution. Thus for example, the ECD growth of ZnO nanowires on a silver (Ag) substrate is not possible because of its solvability in the electrolyte solution. Silver is a suitable material as electrode for application in ZnO nanogenerators (refer to chapter 5), due to its ohmic electric contact with ZnO nanostructures [LJB11, NKR07]. In the following section, an alternative growth method will be introduced, which is a simple promising growth method for a large group of substrate materials.

3.3 Wet chemical method

The wet chemical process is a very simple method for the growth of ZnO nanowires. The low growth temperature, low cost, adaptability to mass production, and suitability to the chemical properties of a large group of conductive and non-conductive substrate materials, are the advantages of this growth method. Figure 3.8 shows ZnO nanostructures synthesized by the wet chemical method at temperatures below T=100 ℃ on flexible (a print foil) as well as on hard substrates (glass). As shown in this figure, ZnO nanostructure can be synthesized on both conductive (Si, Ag) and non-conductive (foil, glass) substrate materials.

Figure 3.9 schematically represents the growth and processing steps in this method.

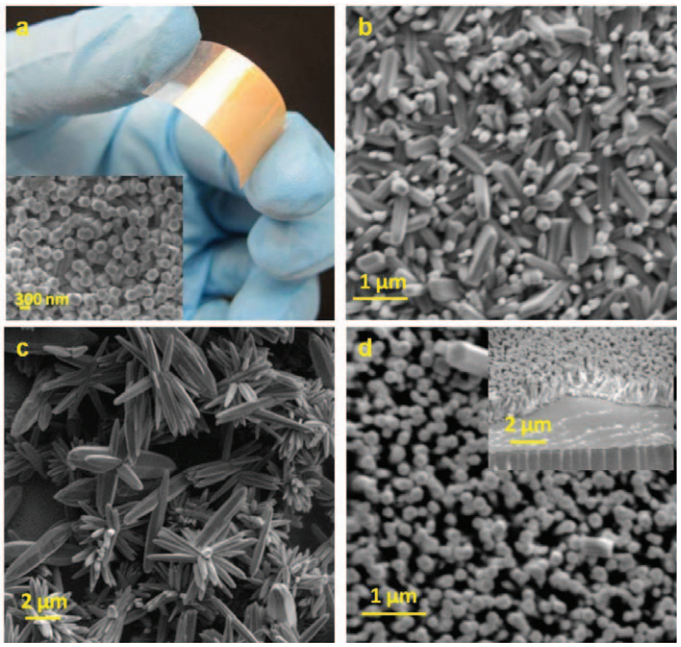

Figure 3.8: SEM images of ZnO nanostructures synthesized by the wet chemical method on (a) flexible print foil, (b) Ag-film, (c) Si, and (d) glass substrate. The wet chemical method enables the growth of different ZnO nanostructures at temperatures below T=100℃ on a large group of conductive and non-conductive, as well flexible and hard substrates.

Usually before starting the wet chemical growth process, the substrate is coated with a seed layer of ZnO nanoparticles. The quality of the alignment and density of grown ZnO nanowires is mainly determined by the seed layer [QL10]. The ZnO nanowires grow at temperatures between T=65 ℃–T=100 ℃ in an aqueous zinc solution of zinc nitrate hexahydrate [$Zn(NO_3)_26H_2O$] and hexamethylenetetramine or hexamine ($C_6H_{12}N_4$), with the $Zn(NO_3)_2/C_6H_{12}N_4$ molar ratio of 1 : 1. The crystal growth of ZnO nanowires involves the following chemical reactions [YX09, JXW06, CLH12].

$$(CH_2)_6N_4 + 6H_2O \rightarrow 6CH_2O + 4NH_3, \tag{3.8}$$

$$(CH_2)_6N_4 + Zn^{2+} \rightarrow [Zn(CH_2)_6N_4]^{2+}, \tag{3.9}$$

$$NH_3 + H_2O \rightarrow NH_4^+ + OH^-, \tag{3.10}$$

$$Zn^{2+} + 4NH_3 \rightarrow Zn(NH_3)_4^{2+}, \tag{3.11}$$

$$Zn^{2+} + 4OH^- \rightarrow Zn(OH)_4^{2-}, \tag{3.12}$$

$$Zn(NH_3)_4^{2+} + 2OH^- \rightarrow ZnO + 4NH_3 + H_2O, \tag{3.13}$$

$$Zn(OH)_4^{2-} \rightarrow ZnO + 2H_2O + 2OH^-, \tag{3.14}$$

$$[Zn(CH_2)_6N_4]^{2+} + 2OH^- \rightarrow ZnO + H_2O + (CH_2)_6N_4. \tag{3.15}$$

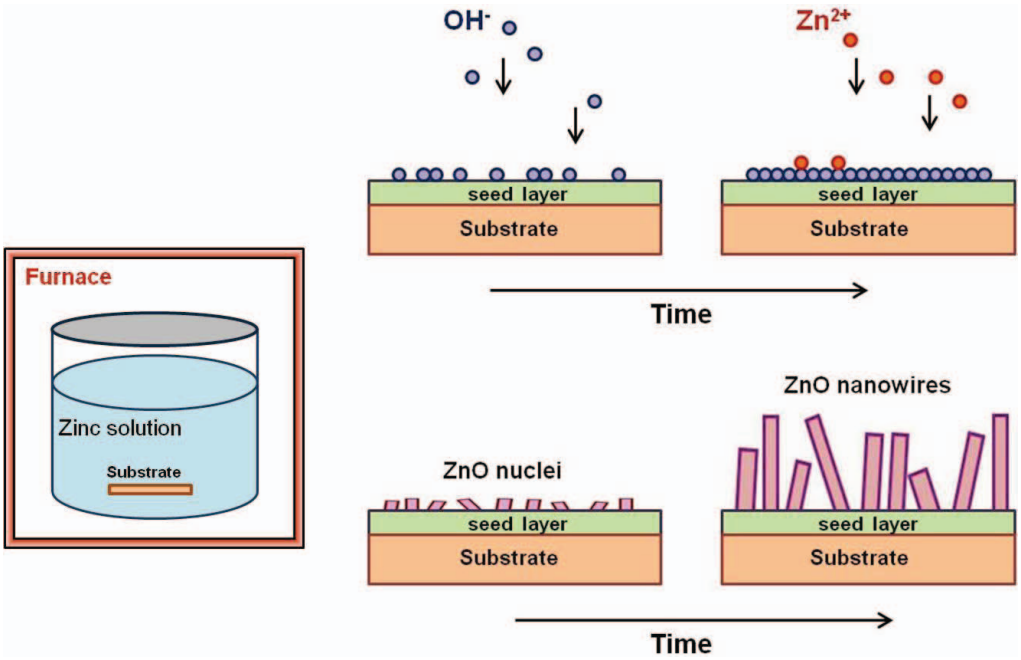

Figure 3.9: (left) Schematic of growth cell in a conventional furnace and (right) Schematic of the growth mechanism of ZnO nanowires by the wet chemical process.

In this work, the influence of growth parameters on morphology, density, orientation and alignment of the ZnO nanowires was studied. This resulted in the advancement of the wet chemical method for ZnO nanogenerators and will be explained in section 5.2.

Different substrates of Si $(10\bar{1}0)$, Si $(11\bar{2}1)$, sapphire (0001), sapphire $(11\bar{2}0)$, kapton

foil, glass, Ag- and Au-coated glass were used. These substrates were separately cleaned with distilled water, acetone and isopropyl in an ultrasonic cleaner for t=10 min, and then baked at T=100 ℃ for at least t=10 min to remove moisture. A 0.01 M solution of lithium hydroxide (LiOH) and zinc acetate dihydrate $[Zn(CH_3COO)_2]2H_2O$ in ethanol was prepared as ZnO nanoparticle solution. Figure 3.10 shows the transmission electron microscopy (TEM) images of the nanoparticles deposited on a copper foil. As shown in this figure, the nanoparticles had an average diameter of D=4 nm. The corresponding electron diffraction pattern (inset in Figure 3.10a) indicates the polycrystalline structure of the film of nanoparticles. Most nanoparticles were grown in the a-axis direction. This is concluded from the distance of about d=0.3 nm between the alternating crystal planes in the nanoparticles, which is matchable with the lattice constant a= 0.325 nm of the hexagonal structure of ZnO (Figure 3.10b). Figure 3.11a indicates the X-ray diffraction (XRD) spectrum of the synthesized nanoparticles deposited on a glass substrate, which can be indexed to the hexagonal crystal structure of ZnO too. Seed layers of these ZnO nanoparticles were deposited on the substrates. For this 5-40 µl/cm^2 of the nanoparticle solution were dispersed on the substrates using a spin coater with a rotation velocity of 30-40 rpm for t=1 min–t=3 min. The ZnO nanostructures were grown at T=75℃–T=104℃ in the zinc solution of 0.001-0.12 M for t=2 h–t=16 h. All substrates were washed with distilled water and dried under a flow of nitrogen. The synthesized structures were characterized using scanning electron microscopy (SEM) and X-ray diffraction (XRD). The XRD spectra of the synthesized nanostructures indicated the hexagonal crystal structure of ZnO, with a better crystalline quality as compared to that of the ZnO nanoparticles seed layer. A typical XRD spectrum of grown ZnO nanowires on a glass substrate is shown in Figure 3.11b. A comparision between SEM images of the synthesized ZnO nanostructures under different growth parameters resulted in the following conclusions:

The influence of seed layer: The seed layer of ZnO nanoparticles influences the morphology, density, and orientation of the nanostructures grown on the substrates. The pre-modified ZnO nanoparticles on a substrate help to form the ZnO nanocrystalline nuclei in the initial stages, in which the growth rate of ZnO is relatively low [MG08]. After the initial stages, the growth rate of nanowires from the ZnO nuclei increases and the nanowires grow clearly faster, denser, and better aligned on the seed layered substrate as compared to a bare substrate. This can be exemplarily seen in Figure 3.12a and 3.12b for nanostructures grown on non-conductive substrates (glass), as well as in Figure 3.12c-f

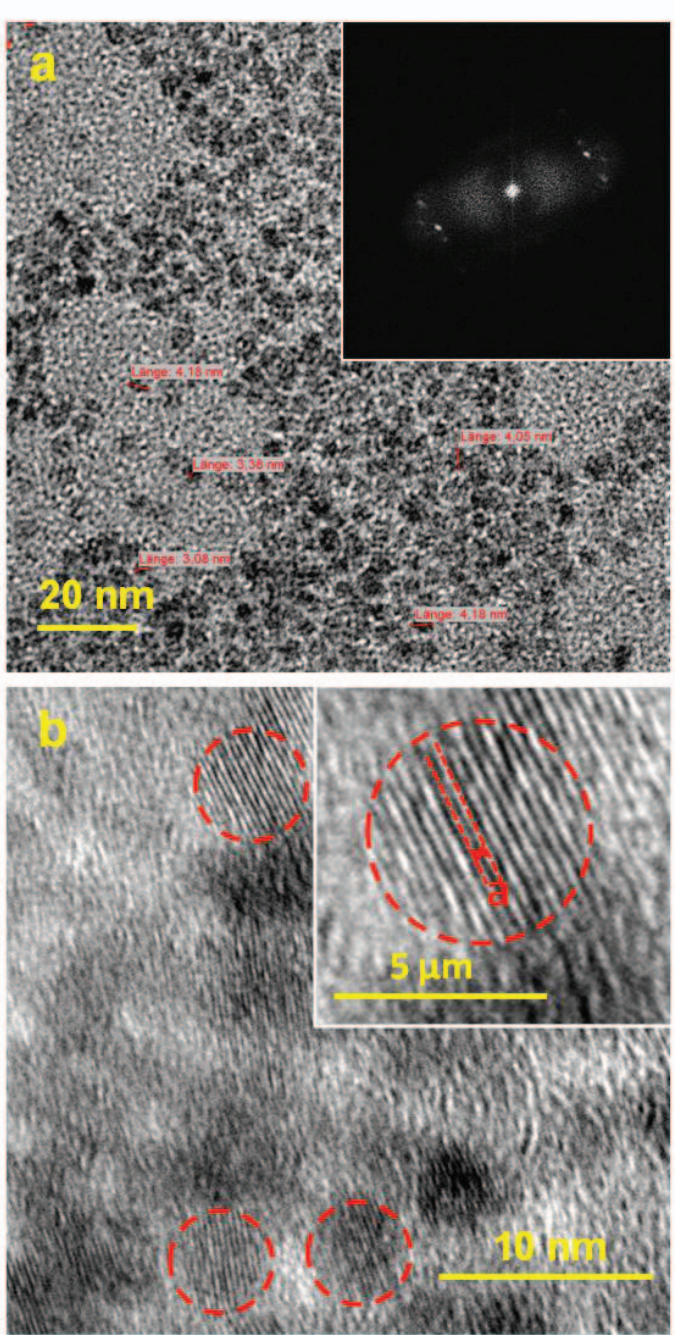

Figure 3.10: (a) TEM image of ZnO nanoparticles of the 0.01 M solution of LiOH and zinc acetate dihydrate. Inset: The corresponding electron diffraction pattern. (b) The enlargement of the ZnO nanoparticles. The red dashed circles indicate the size of corresponding nanoparticles. Inset: The red dashed lines indicate the alternating crystal planes along the growth direction with a distance of a = 0.3 nm.

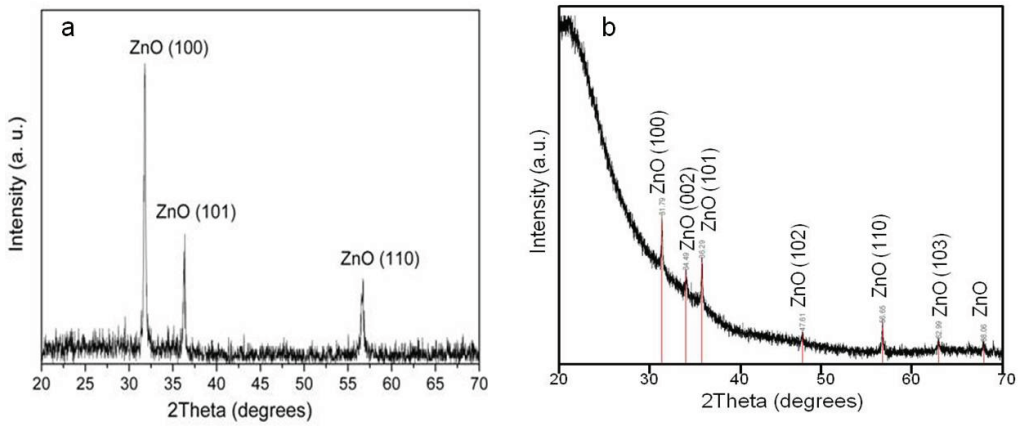

Figure 3.11: (a) XRD-Pattern of ZnO nanoparticles dispersed on a glass substrate. (b) Powder XRD-Pattern of ZnO nanowires grown on a glass substrate.

for nanostructures grown on conductive substrates (Si, Ag). Moreover, one can control the growth of ZnO nanowires on substrates by patterning the seed layers. Figure 3.13 shows an Ag-coated glass substrate, on which both Ag-film and nanoparticle seed layer are patterned in bands with an average width of 30 µm using the photolithography technique. The ZnO nanowires were grown on the patterned seed layer at T=95 ℃ in 0.1 M zinc solution for t=3 h.

The influence of substrate material: As mentioned already, the lattice mismatch between ZnO and the substrate determines the quality of alignment and orientation of grown nanowires. However, by the wet chemical process the substrate has a minor effect because of the used ZnO nanoparticle seed layer as an intermediate layer. In fact the small lattice mismatch between hexagonal wurtzite ZnO and the polycrystalline ZnO seed layer enables the growth of relative vertically aligned ZnO nanowires on different substrate materials. A systematic study for the influence of glass, Ag and Au substrate materials showed that ZnO nanowires grow thicker and better aligned on glass substrates than on metal Ag- or Au-films. Moreover, the grown nanowires on Ag-films were thicker and better aligned than those on Au-films. This can be seen in Figure 3.14 for nanowires synthesized under different growth parameters as examples.

The influence of growth temperature: The deposition rate of Zn^{2+} ions in the

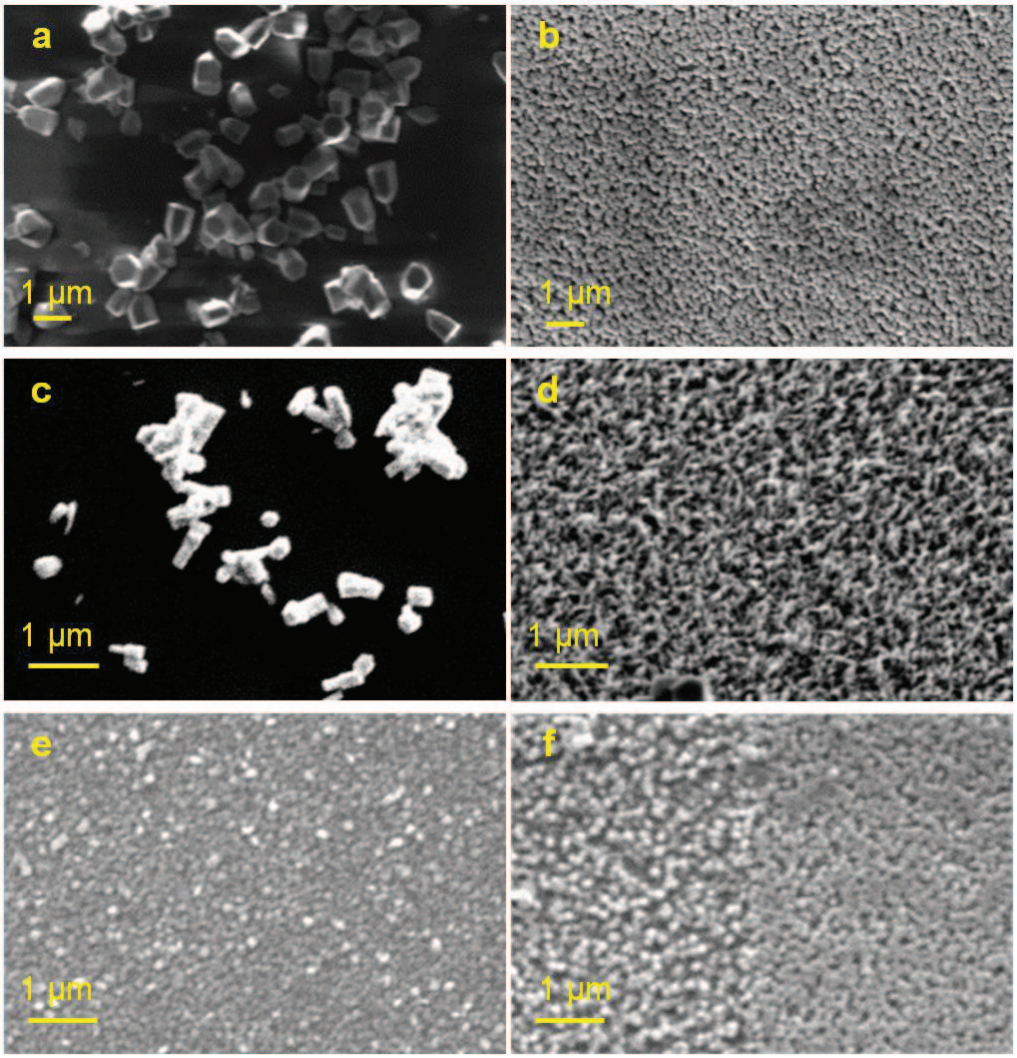

Figure 3.12: ZnO nanostructures grown by the wet chemical method on different seed layered substrates. In (a) 5 µl and (b) 10 µl of nanoparticle solution were spin coated on glass substrates with a surface area of 1 cm × 1 cm. Then ZnO nanostructures were grown at T=98 ℃ in 0.1 M zinc solution for t=5 h. (c) and (d) show grown ZnO nanostructers at T=94 ℃ in 0.07 M zinc solution on bare and seed layered Si subtrates for t=16 h, respectively. In (d) the substrate with a surface area of 1 cm × 1 cm was spin coated with 10 µl of nanoparticle solution. In (e) a seed layer was grown at T=78 ℃ in diluted nanoparticle solution on an Ag-coated glass substrate for t=3 h before starting the growth process. In (f) the left and rigth halfs of an Ag-coated glass substrate were dip-coated with diluted and undiluted nanoparticle solutions, respectively. Then ZnO nanowires were grown at T=95 ℃ in 0.1 M zinc solution on the substrates for t=2: 30 h.

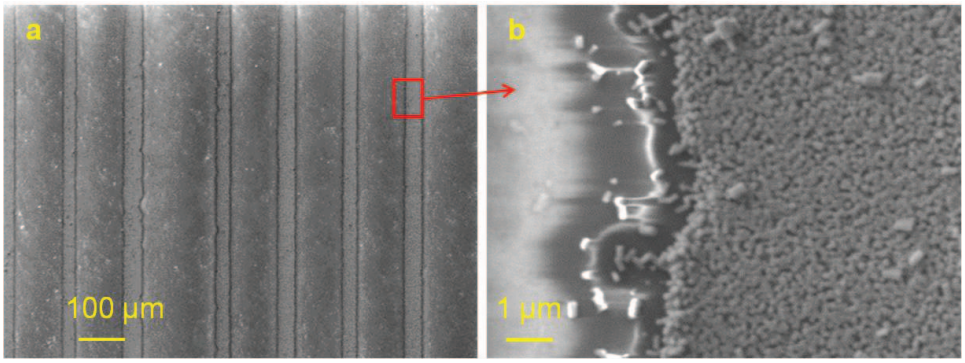

Figure 3.13: (a) ZnO nanowires array grown on an Ag-coated glass substrate. Both Ag-film and nanoparticle seed layer are patterned using the photolithography technique. (b) The enlargement of the red squared zone. The nanowires are grown well-aligned and dense only on the seed layered zones.

zinc solution increases as the temperature increases. This could improve the supply of adequate reactants for the reactions 3.11 and 3.12. Moreover, the production rate of ZnO in the reactions 3.13 and 3.14 increases. Hence, the growth rate of ZnO nanowires, and therefore, the average diameter and the length of nanowires increases as the growth temperature increases. As mentioned already in section 2.1, the longitudinal growth of wurtzite ZnO nanowires is faster than the lateral one, due to the different surface energy of the crystal planes. This suggests a higher growth rate of the nanowire length than that of the nanowire diameter. A systematic study also indicated that the diameter distribution of ZnO nanowires becomes wider and the alignment quality of vertically grown nanowires decreases when the growth temperature increases. Figure 3.15 exemplarily shows ZnO nanowires synthesized at temperatures T=75 ℃–T=100 ℃ on glass and Ag-coated glass substrates in a 0.1 M zinc solution for t=5 h. For example, the nanostructures synthesized on glass substrates at a low temperature of T=75 ℃ were smaller than those synthesized at a higher temperature of T=98 ℃ (Figure 3.15a and b) and those synthesized on Ag-films at a temperature of T=85 ℃ were better alined with nearly the same length and diameter than those synthesized at high temperature of T=100 ℃ (Figure 3.15c and d).

The influence of Zn concentration: The formation of ZnO structures depends strongly on the zinc ions concentration in the zinc solution. For a high zinc solution concentration a large number of zinc ions is deposited at the substrate surface. The reactions 3.11 and 3.12 may be accelerated and consequently the growth rate becomes higher. This

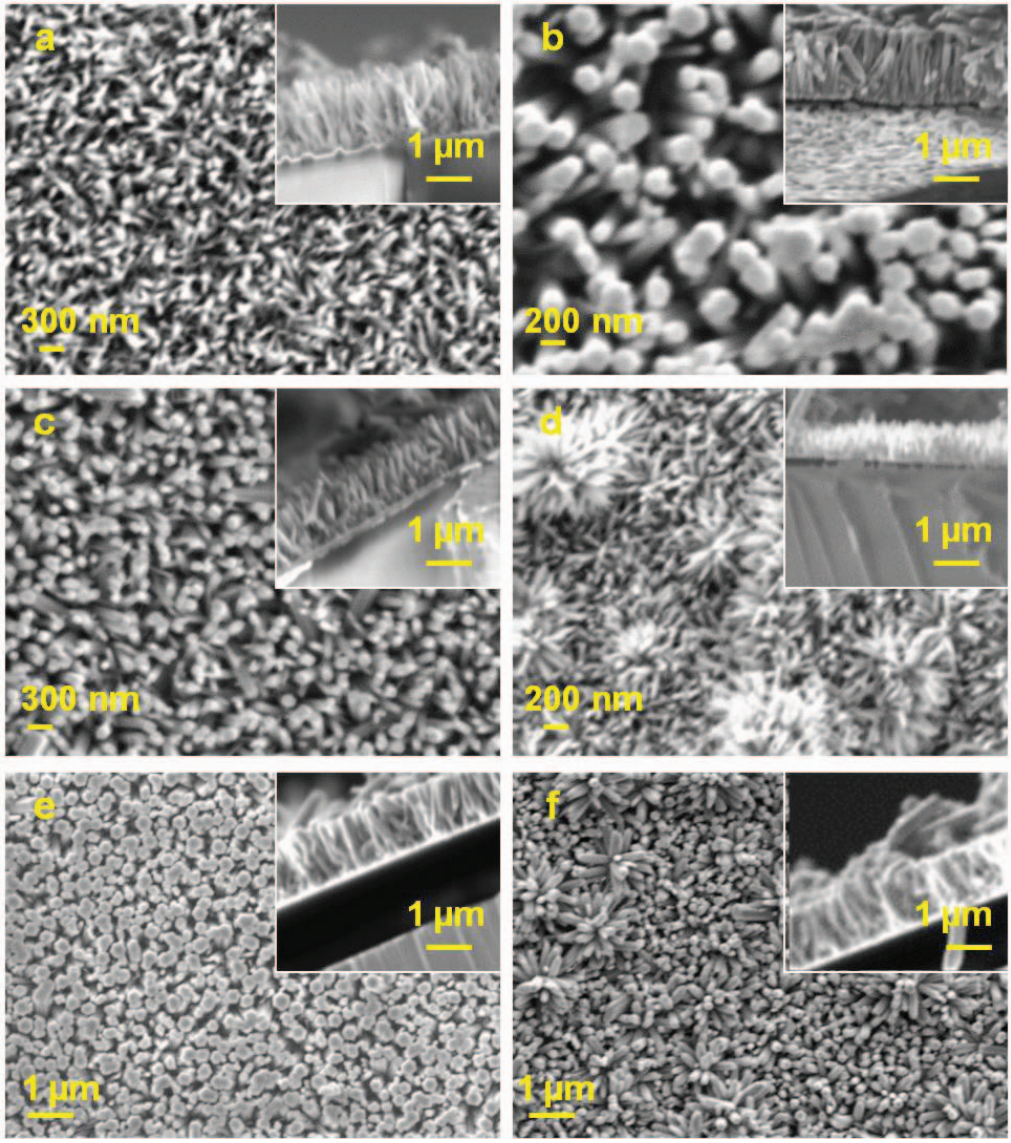

Figure 3.14: (a) and (b) SEM images of ZnO nanowires grown by the wet chemical method at T=98 ℃ in 0.07 M zinc solution on seed layered Au-film and glass substrate, respectively. (c) and (d) SEM images of ZnO nanowires grown at T=95 ℃ in 0.08 M zinc solution on seed layered Ag- and Au-film, respectively. (e) and (f) SEM images of ZnO nanowires grown at T=95 ℃ in 0.1 M zinc solution on seed layered Ag- and Au-film, respectively.

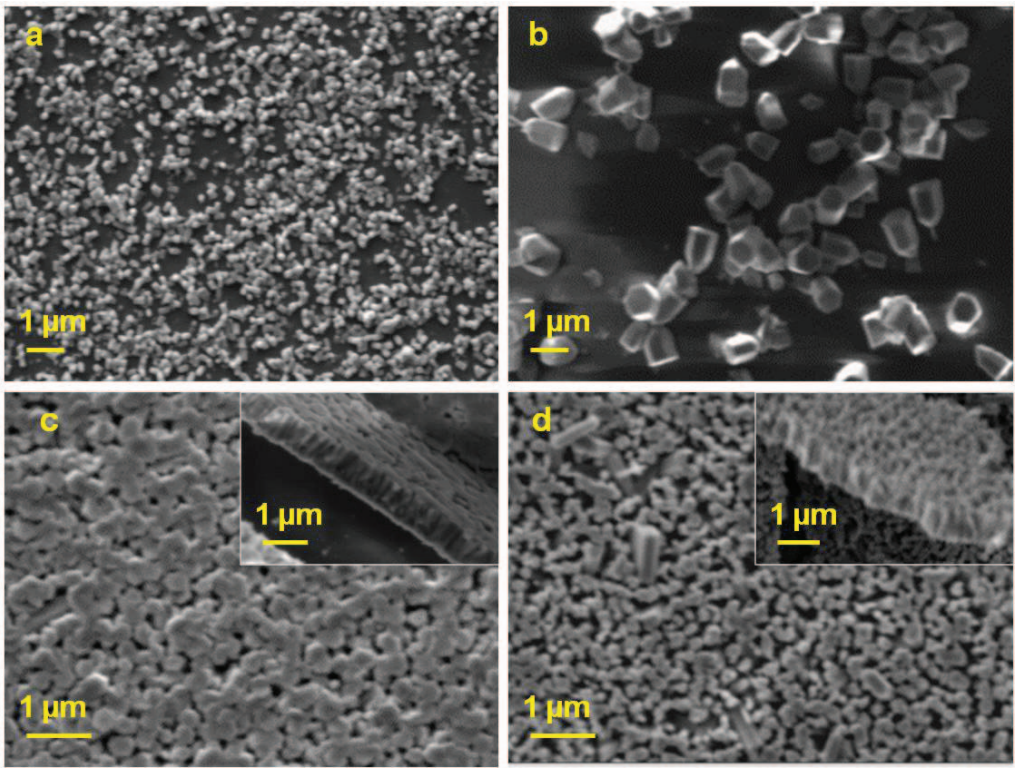

Figure 3.15: SEM images of ZnO nanowires grown by the wet chemical method at (a) T=75 ℃ and (b) T=98 ℃ in 0.1 M zinc solution on glass subtrates for t=5 h. Both substrates with surface areas of 1 cm × 1 cm were spin coated with 5 µl of ZnO nanoparticle solution. (c) and (d) SEM images of ZnO nanowires grown at (c) T=85℃ and (d) T=100℃ in 0.1 M zinc solution on Ag-coated glass subtrates for t=5 h. Both substrates with surface areas of 1 cm × 1 cm were spin coated with 10 µl of ZnO nanoparticle solution.

suggests an increase of the nanowire diameter with increasing Zn^{2+} concentration. Figures 3.14c-f show the ZnO nanowires synthesized by the wet chemical method at T=95 ℃ on Ag- and Au-coated glass substrates in 0.08 and 0.1 M zinc solutions for t=6 : 45 h. One can see the average diameter of synthesized nanowires increases when the concentration of zinc solution increases. In addition, the diameter distribution of ZnO nanowires becomes narrower and the alignment quality of vertically grown nanowires inrceases when the zinc concentration increases. That means well aligned ZnO nanowires with uniform diameters can be synthesized at high zinc solution concentration. It seems that the length of grown ZnO nanowires depends only weakly on the zinc concentration, but strongly on the growth temperature as mentioned already.

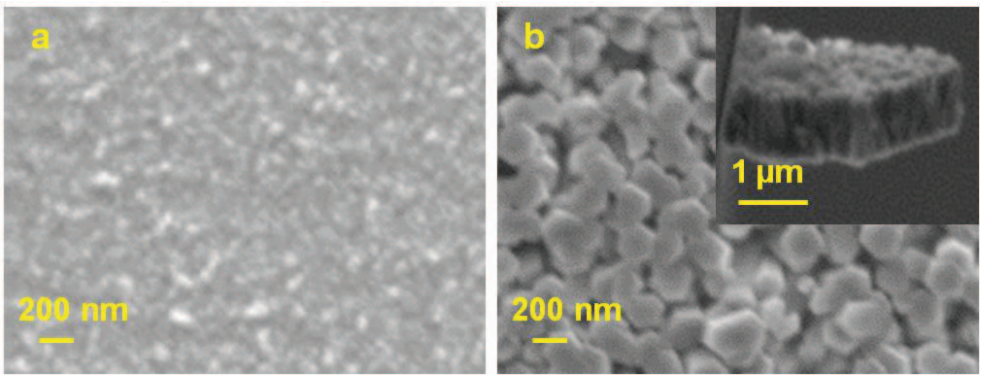

Figure 3.16: SEM images of ZnO nanowires synthesized by the wet chemical method at T=80 ℃ in 0.1 M zinc solutions on Ag-coated glass substrates for (a) t=2 h and (b) t=6 h. The grown ZnO nanowires are in (a) ∼ 50 nm thick and ∼ 70 nm long (measured with a profile meter) and (b) ∼ 180 nm thick and ∼ 1 µm long as shown in the inset.

The influence of growth time: The average diameter and length of grown nanowires increase when the growth time increases. During the total growth process the zinc ions concentration does not stay constant. The decrease of zinc ions concentration restricts the progress of ZnO production in the reactions 3.11 and 3.12. Hence, the growth rate of ZnO nanowires is limited. Figure 3.16 shows, as an example, the SEM images of ZnO nanowires synthesized by the wet chemical method at T=80 ℃ in 0.1 M zinc solutions on Ag-coated glass substrates for t=2 h and t=6 h. The nanowires grown for t=6 h were about 14 times longer and 3.5 times thicker than those grown for t=2 h. Moreover, it seems that growth times longer than 5 h result mainly in the formation of ZnO clusters on the substrate surfaces while the size of nanowires does not increase any more. Figure 3.17 shows exemplarily ZnO nanowires and clusteres synthesized on metal substrates for t=5 h and t=16 h.

The formation of ZnO clusters on the nanowires film surface: In addition to the ZnO nanowires, clusters of small ZnO nanostructures were always synthesized on the substrates by the wet chemical process (see Figure 3.17). The morphology, size and density of these structures depend on the growth parameters. Generally, more ZnO clusters were produced on the substrates by higher zinc solution concentration, higher growth temperature, and longer growth time. In addition, more ZnO clusters were produced on Au-films than on Ag-films and less on glass substrates under the same growth conditions.

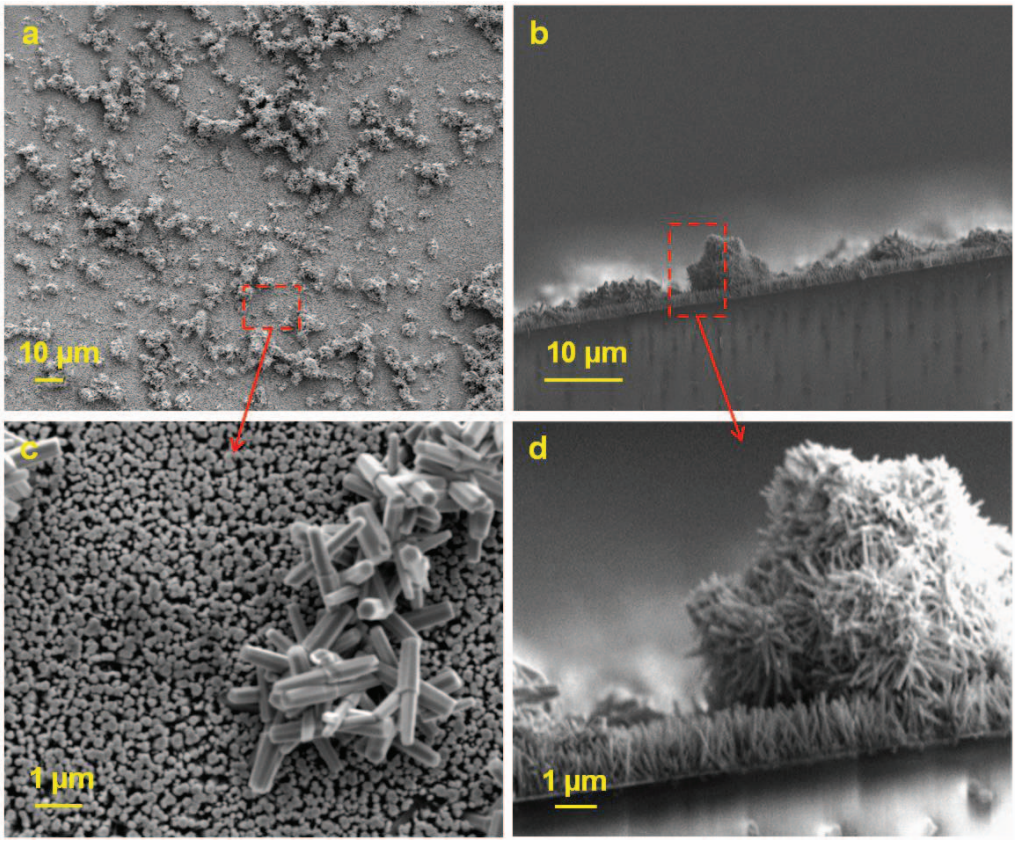

Figure 3.17: (a) Top view and (b) cross-sectional view of typical ZnO clusters formed on synthesized ZnO nanowires films by the wet chemical process. (c) and (d) are the enlargements of the red squared zones in (a) and (b), respectively.

Figure 3.17 shows SEM images of typical ZnO clusters formed on the synthesized nanowires film surface by the wet chemical process. Cleaning the substrate in an ultrasonic cleaner can reduce the amount of ZnO clusters on the nanowires film, but results in the creation of holes on the ZnO film surface too, as shown in Figure 3.18. It seems that in the first growth steps (growth time shorter than 3 h) circular zones on the ZnO surfaces are formed, specially in lower zinc concentration, which might detach and appear as holes during the cleaning process in an ultrasonic cleaner. I call these zones ″potential holes″. Figure 3.19a shows potential holes on a ZnO film surface. Figure 3.19b depicts as an example a surface damage due to the cleaning process of the film grown in 0.1 M zinc solution at T=80 ℃ for t=2 h.

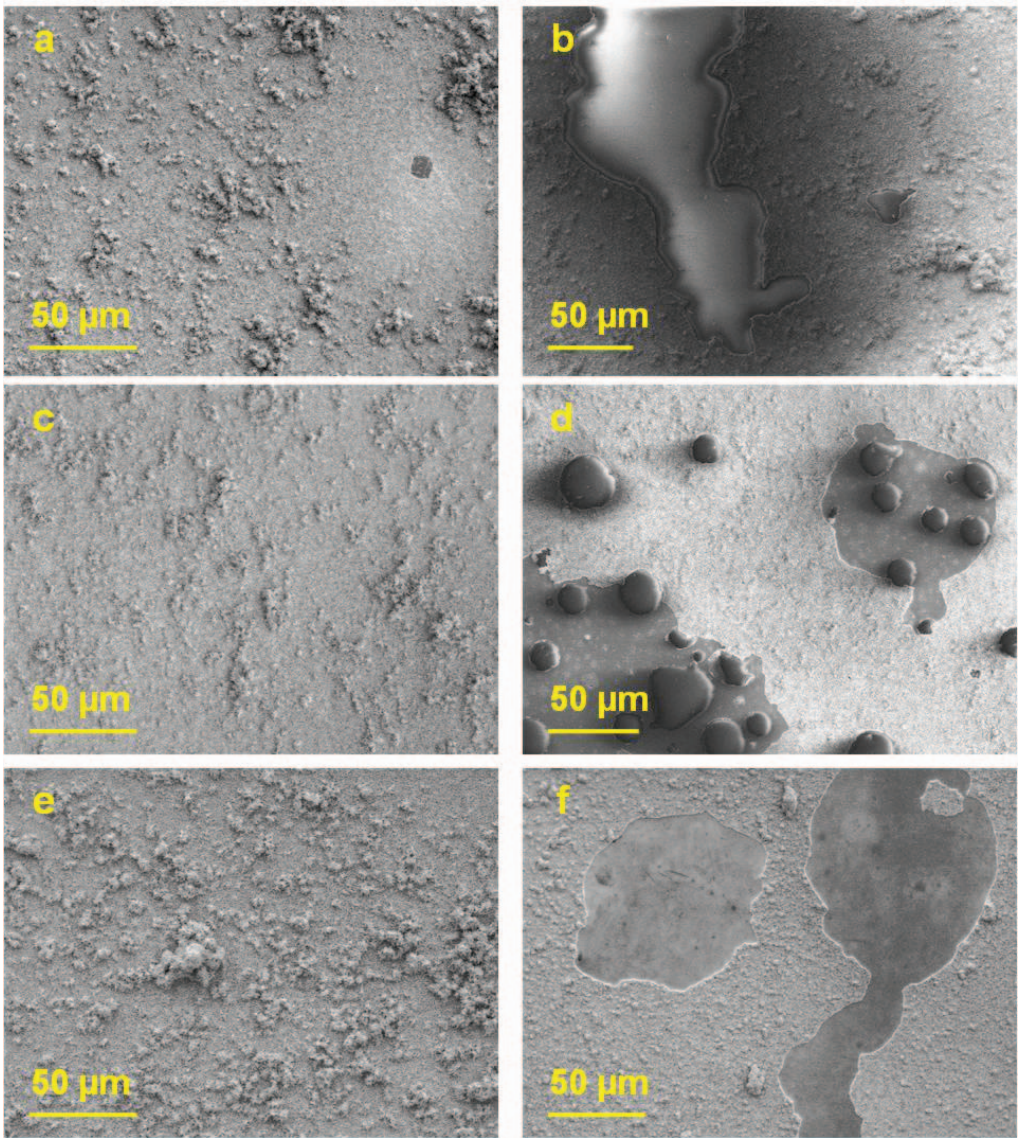

Figure 3.18: SEM images of the ZnO nanowire film before (left column) and after cleaning process (right column). (a) and (b) ZnO film of nanowires synthesized at T=98 ℃ in 0.07 M zinc solution (see Figure 3.14 a too) before and after cleaning in an ultrasonic cleaner for t=80 seconds, respectively. (c) and (d) ZnO film of nanowires synthesized at T=95 ℃ in 0.08 M zinc solution (see Figure 3.14 c too) before and after cleaning in an ultrasonic cleaner for t=80 seconds, respectively. (e) and (f) ZnO film of nanowires synthesized at T=95 ℃ in 0.1 M zinc solution (see Figure 3.14 e too) before and after cleaning in an ultrasonic cleaner for t=3 min, respectively.

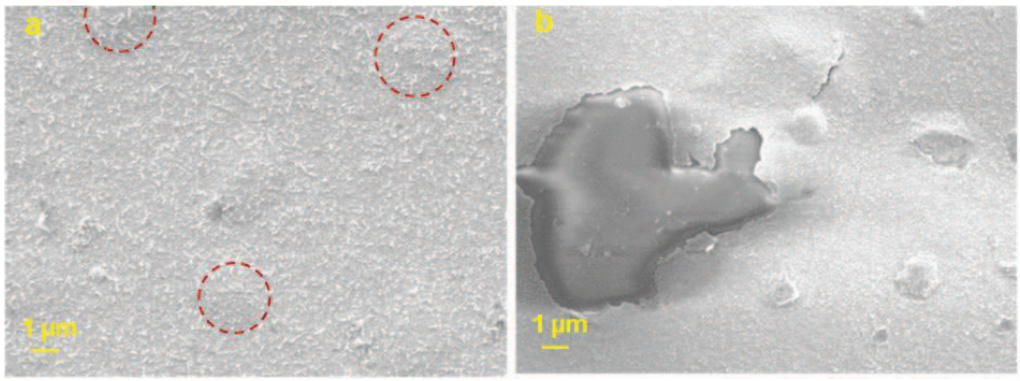

Figure 3.19: SEM images of ZnO nanowires film grown in 0.1 M zinc solution at T=80°C for t=2 h. (a) The ZnO film surface before the cleaning process. The red dashed circles represent the potential holes. (b) The ZnO surface after the cleaning process with a big hole and some damaged circular zones created during t=2 min cleaning in distilled water in an ultrasonic cleaner.

4 Comb-like ZnO nanostructures

Recently, ZnO comb-like nanostructures have attracted considerable attention for the application in nanoscale functional devices such as nanocantilevers [ZLW03], UV nanolaser arrays [HY03], optical nanogratings and nanopolarizers [ZWP05, KY08a]. In this chapter, a comb-like structure is described and the common synthesis methodes and growth mechanism are introduced. Then the synthesis of ZnO nanocombs by the VLS methode with a non-conventional molar ratio ZnO : C (2 : 3) is reported. At the end, a model for the growth of ZnO nanocombs is developed that explains the periodic growth of nanowire branches of a nanocomb on the polar +(0001) surface of a ZnO nanobelt, as a result of the piezoelectric character of ZnO. This model could further give an insight into the interaction between the growth parameters and allows more effective controlling of the growth of ZnO nanostructures.

4.1 Current state of research

A nanocomb structure is described as a self organized multi-dimensional nanostructure, such that one-dimensional nanowires are distributed in an ordered manner on one or both sides of a two-dimensional backbone nanosheet. Figure 4.1 shows a SEM image of double sided nanocombs formed by evaporating ZnO powder at T=1350 ℃. High-resolution TEM images of the reported nanocombs show that the backbone nanosheet with its top/bottom surface ±(0001) grows preferentially along $[01\bar{1}0]$ with the side dominated surfaces $(2\bar{1}\bar{1}0)$ [ZWP05, KY08a, YSL06, TX12] or along $[2\bar{1}\bar{1}0]$ with the side dominated surfaces $(01\bar{1}0)$ [XYK03, ZLW03]. The ZnO nanowire branches grow along [0001] perpendicular to the polar (0001) surfaces (see Figure 4.2a, 4.2d-e).

4.1.1 Synthesis of ZnO nanocombs

ZnO nanocombs can be synthesized by thermal evaporation using pure Zn or ZnO powders [ZLW03, ZWP05, RFZ08], or most commonly, by the carbothermal reduction process

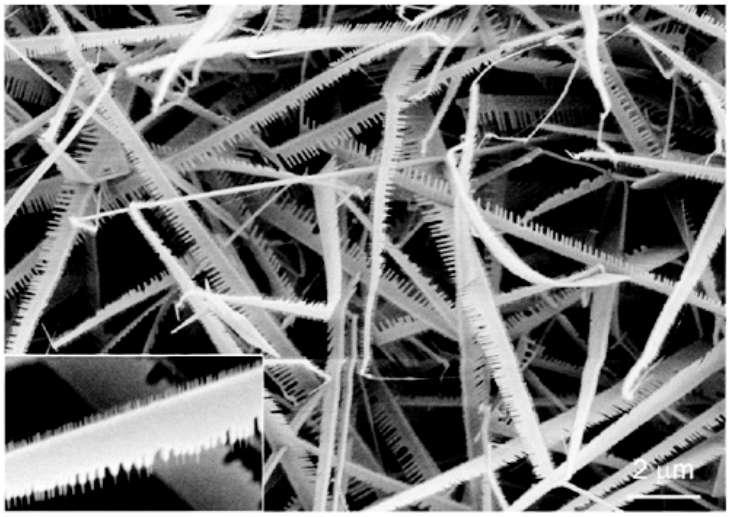

Figure 4.1: SEM image of double sided nanocombs formed by evaporating ZnO powder at T=1350 ℃ [ZLW03].

between graphite and ZnO powder [KY08a, YSL06, YHL04, RFZ08]. For the growth of ZnO nanocombs high Zn vapor pressure is essential. This can be achieved at high temperatures (T=1350 ℃–T=1500 ℃) and/or by proper control of the vapor pressure for the carbothermal reduction [YSL06]. The Zn vapor pressure can be controlled by using other source materials rather than a mixture of ZnO and graphite powder. Leung et al. [YHL04] have reported the synthesis of ZnO nanocombs at relatively low temperatures (T=1000 ℃–T=1100 ℃) by using single-walled carbon nanotubes (SWCNT) as the carbon source. Lim et al. [YSL06] have reported the synthesis of ZnO nanocombs by the carbothermal reduction process at T=1050 ℃ with carbon black powder as the carbon source. Yu et al. [KY08a] have synthesized ZnO nanocombs at T=900 ℃ by using CuO powder as a catalyst in the graphite carbon source.
In section 4.2, the possibility of synthesis of ZnO nanocombs by the vapor-liquid-solid (VLS) method under temperature variations of T=953 ℃–T= 1034 ℃ and T=961 ℃–T= 1040 ℃ using conventional graphite as the carbon source is reported.

4.1.2 Growth mechanisms of ZnO nanocombs

The mechanism that drives the growth of comb-like structures of ZnO was not elaborated until recently. The formation of ZnO nanocombs is known to be closely related with

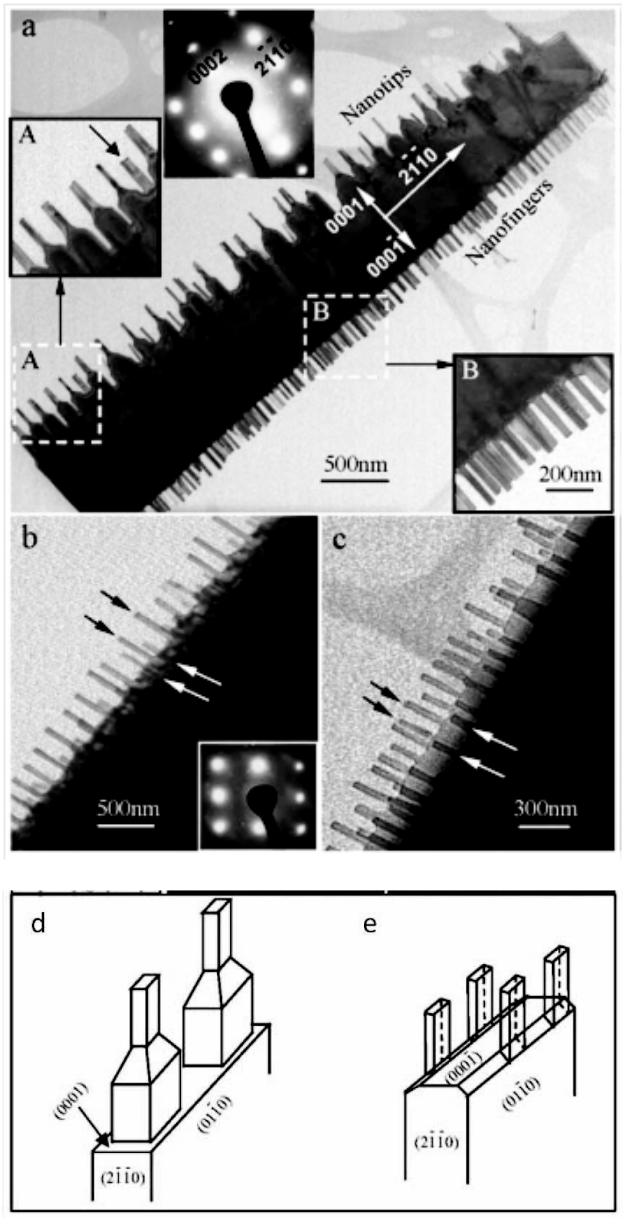

Figure 4.2: (a) TEM image of a double sided ZnO nanocomb synthesized at T=1350 ℃ by thermal evaporation. The insets are the corresponding electron diffraction pattern and the enlargements of two selected areas, as indicated. (b),(c) TEM images of the shorter ZnO branches grown on the bottom surface $(000\bar{1})$, showing their origin at the two edges of the backbone nanobelt. The white and black arrowheads indicate the branches rooted at the top and bottom edges, respectively. (d), (e) Schematic models of nanowire branches grown on the (0001) and $(000\bar{1})$ sides, respectively [ZLW03].

the polarity of the ZnO structure and to be an asymmetric growth along the [0001] direction [JHP04]. As mentioned in section 2.1, ZnO may be considered as alternating polar planes of Zn-terminated and O-terminated surfaces along the [0001] direction (see Figure 4.15). Wang et al. [ZLW03] have reported that the Zn-terminated +(0001) polar surface is chemically active and the oxygen-terminated −(0001) polar surface is inactive in the growth of nanocombs. They showed, using high-resolution transmission electron microscopy (HRTEM), that the Zn-terminated polar +(0001) surface has tiny Zn clusters. This suggests a self catalytic growth of ZnO branches analogous to the vapor-liquid-solid (VLS) growth process due to the enrichment of Zn on the Zn-terminated surface. The chemically inactive −(0001)-O surface typically does not initiate any growth, but controlling the growth temperature could lead to the growth of shorter and narrower ZnO branches from the intersections between −(0001)-O and $\pm(01\bar{1}0)$ surfaces [ZLW03], as shown in Figure 4.2. Schematic models of nanowire branches grown on the polar +(0001) surface and at the intersections between the polar −(0001) and $\pm(01\bar{1}0)$ surfaces, are shown in Figure 4.2d and 4.2e. The corresponding electron diffraction patterns (insets in Figure 4.2a and 4.2b) indicate the single crystalline structure of both backbone nanosheet and nanowire branches of the synthesized nanocomb. Lim et al. [YSL06] have mentioned that defective sites on the Zn-terminated surface, such as step edges and nano-sized holes, could provide proper sites for Zn clustering, so that the Zn cluster acts as a self catalyst for the growth of one-dimensional nanowire branches along the [0001] direction on two-dimensional nanosheet. The O-terminated surface is much smoother than Zn-terminated surface and it has no self catalytic effect for the growth of ZnO nanowire branches on the nanosheet [YSL06].

However, in previous studies, the reason why the ZnO nanowire branches grow parallel and evenly spaced on the polar +(0001) surface of the backbone nanosheet (or nanobelt) remained unclear. In section 4.3, a model for the growth of ZnO nanocombs is developed, which can explain the periodic growth of nanowire branches as a self catalytic process on the base of piezoelectric character of ZnO.

4.2 Vapor-liquid-solid method for synthesis of ZnO nanocombs

In this section, the synthesis of ZnO nanocombs under temperature variations of T=953 ℃–T=1034 ℃ and T=961 ℃–T=1040 ℃ by the vapor-liquid-solid (VLS) method is reported. For this synthesis process, conventional graphite was used as the carbon source

but with a non-conventional molar ratio ZnO: C (2: 3).

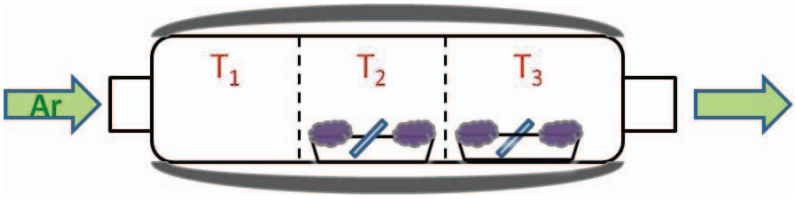

Figure 4.3: Schematic of the VLS process to synthesize ZnO nanowalls and nanocombs at the same time in a horizontal three-zone furnace.

The ZnO nanocombs and nanowalls were synthesized at the same time by the VLS method in a horizontal three-zone furnace (see Figure 4.3). The Si (111) substrates were coated with Au as catalyst. The layer thickness of Au was d=2.5 nm. A mixture of ZnO powder and graphite carbon powder with a molar ratio of 2: 3 was used as source material. Two substrates were handled simultaneously and placed in two quartz boats. In each boat, the substrate was placed in the center and the powder mixture at both end sides. The first boat was placed in the center of a quartz tube and the second one downstream 8 cm away from the center of the tube. Finally, the tube was inserted into the furnace. The furnace was at first heated up to T=650 ℃ and kept at this temperature for one minute. At this temperature the Au film brakes up into droplets, which are the preferential nucleation centers for the growth of ZnO nanostructures on the substrates. Then the furnace was heated up to T=1120 ℃–T=1130 ℃ in the middle and upstream zone and up to T=1034 ℃–T=1040 ℃ in the downstream zone and kept at these temperatures for t=30-45 minutes. Finally the furnace was cooled down to room temperature. For all the processes the same heating/cooling rate of 6 ℃/min in the middle and upstream zone and 1.8 ℃/min in the downstream zone was measured. During the synthesis process, argon served as carrier gas at a flow rate of 41 sccm (standard cubic centimeters per minute).

Figure 4.4 shows SEM images of the ZnO nanowalls and nanowires grown on a Au-catalyzed Si (111) substrate. The substrate was placed in the first boat in the center of the furnace at T=1130 ℃ for 45 minutes. It seems that under the applied experimental conditions, most of the Au nanodroplets form Au nanostrips (see Figure 4.4b and 4.4c) due to cohesive and adhesive forces. Since no synthesized ZnO structures in the form of nanostrips (or consequently nanowalls) could be observed by using the standard VLS molar ratio ZnO: C (1: 1), the higher Zn vapor in the present experimental conditions should be

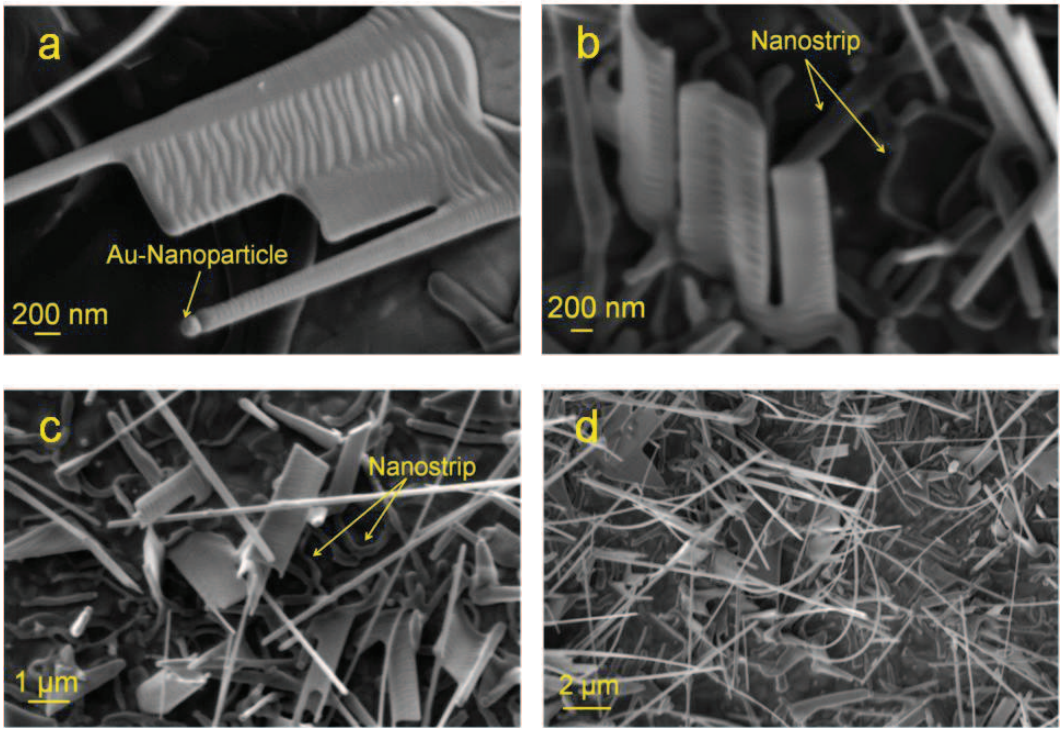

Figure 4.4: SEM images of ZnO nanowalls synthesized at T=1130 ℃ by the VLS method on Si (111) substrate. (a,b) Layer-by-layer growth of nanowalls. By the VLS method the Au catalyst particles usually stay at the tips of the ZnO nanostructures. (b,c) Au nanostrips formed on the substrate, which are the preferential nucleation centers for the growth of ZnO nanowalls. (d) Synthesized long nanowires and short nanowalls on the substrate.

of importance for the formation of Au nanostrips from Au nanodroplets. This suggests the formation of Au nanostrips as a result of action of the Zn vapor on the Au nanodroplets. As mentioned above, more graphite was used in comparison to the standard VLS molar ratio ZnO: C (1: 1). Hence more Zn atoms from the ZnO powder can be vaporized. Thus Zn saturates relative homogeneously in the nanostrips and consequently ZnO nucleates relative homogeneously under the nanostrips on the substrate too. This is followed by the crystallization of ZnO in the form of nanostrip structures on the substrate. The saturation process of Zn in an alloy nanostrip takes a particular time due to its relative high volume. Consequently, the building of a ZnO nanostrip under the primary Au nanostrip takes place in a particular period of time. This results in the layer-by-layer growth of a nanowall from the ZnO nanostrips as shown in Figures 4.4a and 4.4b. Figure 4.4a shows also a

crystallized ZnO nanowire under an Au nanodroplet joined at the bottom to the neighbor ZnO nanowall. By the VLS mechanism the Au catalyst particles usually stay at the tips of the ZnO nanowires [SYL03]. Because the saturation process of Zn is faster in an alloy nanodroplet than in an alloy nanostrip, the grown ZnO nanowires on the substrate are longer than the ZnO nanowalls (see Figure 4.4c and 4.4d).

The ZnO nanowalls can also be synthesized at lower temperature T=1120 ℃ in the center of the furnace (see Figure 4.5).

In order to study the influence of the growth time on the morphology of ZnO nanostructures, Au-catalyzed Si (111) substrates were used under the same growth conditions but with different growth times between t=30 min–t=45 min. A comparison of the SEM images of the grown nanowalls and nanowires shows that generally, the dimension of the nanostructures increases significantly with the growth time. This can be seen for example in Figure 4.5 for nanowalls synthesized at T=1120 ℃ in the center of the furnace on Si (111) substrates for t=30 min and t=40 min. The nanowalls grown for t=30 min (representative dashed forms in Figure 4.5a) are mostly about w=550 nm wide and h=3µm–h=4.5µm high, but those grown for t=40 min (representative dashed forms in Figure 4.5b) are about h=4 µm–h=7 µm high and show a width distribution in a range of w=0.8 µm–w=4 µm.

Figure 4.6 shows the SEM images of the grown nanocombs on an Au-catalyzed Si (111) substrate. The substrate was placed in the second quartz boat 8 cm away from the center of the furnace in the downstream zone (see Figure 4.3 too). During the growth time of t=45 min, the temperature was constant at T=1130 ℃ in the center of the furnace

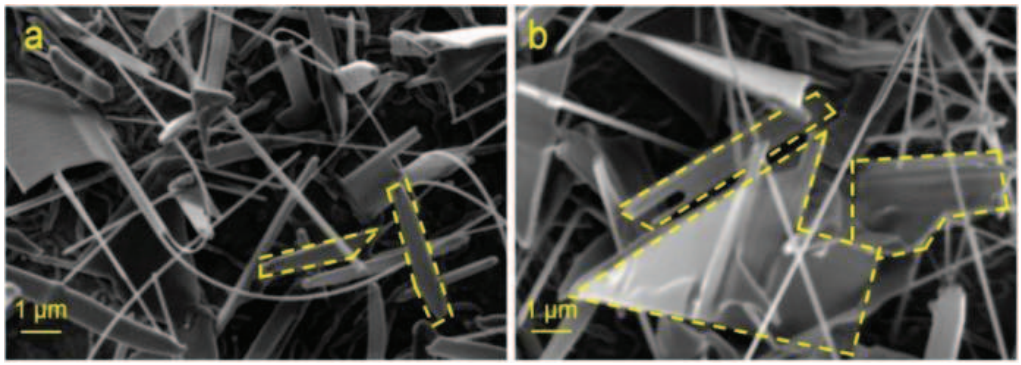

Figure 4.5: SEM images of ZnO nanostructures synthesized at T=1120 ℃ by the VLS method on Si (111) substrates. The growth time was (a) t=30 min and (b) t=40 min. The dashed lines show representative nanowalls.

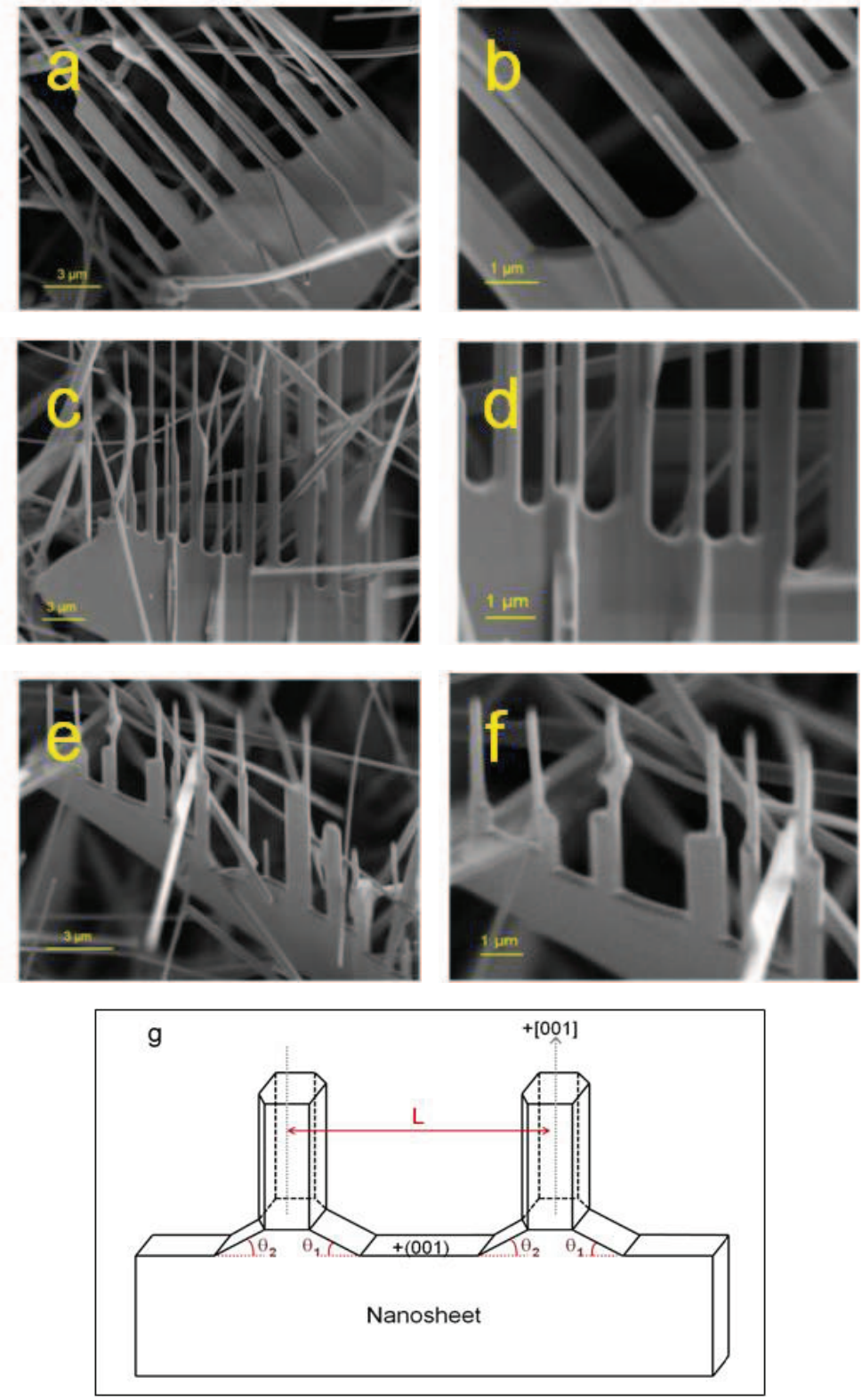

Figure 4.6: SEM images of ZnO nanocombs synthesized under temperature variation T=961 ℃–T=1040 ℃ by the VLS method on a Si (111) substrate. The facets between nanowire side and the nanosheet side are placed at $\theta_1 \cong 90$, $\theta_2 \cong 37$ degrees (a,b), $\theta_1 = \theta_2 \cong 37$ degrees (c,d) and $\theta_1 = \theta_2 \cong 90$ degrees (e,f). (g) Schematic geometry of a nanocomb. L is the periodicity of the grown nanowires on the sheet of a nanocomb.

but increased from T=961 ℃ up to T=1040 ℃ with a heating rate of 1.8 ℃/min in the downstream zone. ZnO nanocombs could not be synthesized at constant temperature in the range T=900 ℃–T=1100 ℃ on Si substrates placed in the center of the furnace. The Zn vapor from the exit side of the first boat in the center of the furnace can alter the Zn vapor flux in the downstream zone. Thus, it seems that the temperature variation, changing the Zn vapor flux in the downstream zone, or both play a significant role during the formation of ZnO nanocomb structures. Figure 4.6g schematically shows the geometry of as grown nanocombs, in which nanowire branches with a periodicity of L are grown on the polar +(0001) surface of the backbone nanosheet. The angles θ_1 and θ_2 indicate the position of facets between the nanowire side and the nanosheet side. Three types of nanocombs with different facets (different angles θ_1 and θ_2) were synthesized on the substrate. For the nanocombs shown in Figure 4.6a and 4.6b, these facets are placed at $\theta_1 \cong 90$ degrees and $\theta_2 \cong 37$ degrees. For the nanocombs shown in Figure 4.6c and 4.6d, as well for those shown in Figure 4.6e and 4.6f there are the same facets for both sides of the nanowires which are placed at $\theta_1 = \theta_2 \cong 37$ degrees and $\theta_1 = \theta_2 \cong 90$ degrees, respectively. The grown nanowires on the same backbone nanosheet have different periodicities. This may be caused by the Ar flow fluctuation during the growth process. For the nanocombs shown in Figure 4.6a and 4.6b the grown nanowires have the periodicity in a range of L=2.06 µm–L=2.14 µm. For the nanocombs shown in Figure 4.6c and 4.6d the periodicity lies in a range of L=1.50 µm–L=1.75 µm. The periodicity for the nanocombs shown in Figure 4.6e and 4.6f lies in a range of L=2.00 µm–L=2.30 µm. ZnO nanocombs were also synthesized under the same experimental conditions but at lower temperature T=1120℃ in the center of the furnace and temperature variation of T=953 ℃–T=1034 ℃ in the downstream zone (Figure 4.7b). The nanocombs synthesized at lower temperatures have more surface contaminations and defect sites on their nanowires (see Figure 4.7a and 4.7b).

The grown nanocombs and nanowalls on the Si substrates are well crystallized and can be indexed to the hexagonal structure of ZnO with the lattice constants $a = 0.325$ nm and $c = 0.521$ nm as can be deduced from the XRD spectra shown in Figure 4.8.

The chemical composition of the surface layer of the grown nanowalls and nanocombs was studied using Auger electron spectroscopy (AES). Figure 4.9 and 4.10 show the AES-spectra of the nanowalls and nanocombs, which are synthesized simultaneously but at T=1130 ℃ in the center of the furnace and under temperature variation of T=961℃–T=1040℃ in the downstream zone, respectively. The spectra show that the atomic rate of zinc and oxygen varies within the structures. As can be seen in Figure 4.9, zinc and oxygen have

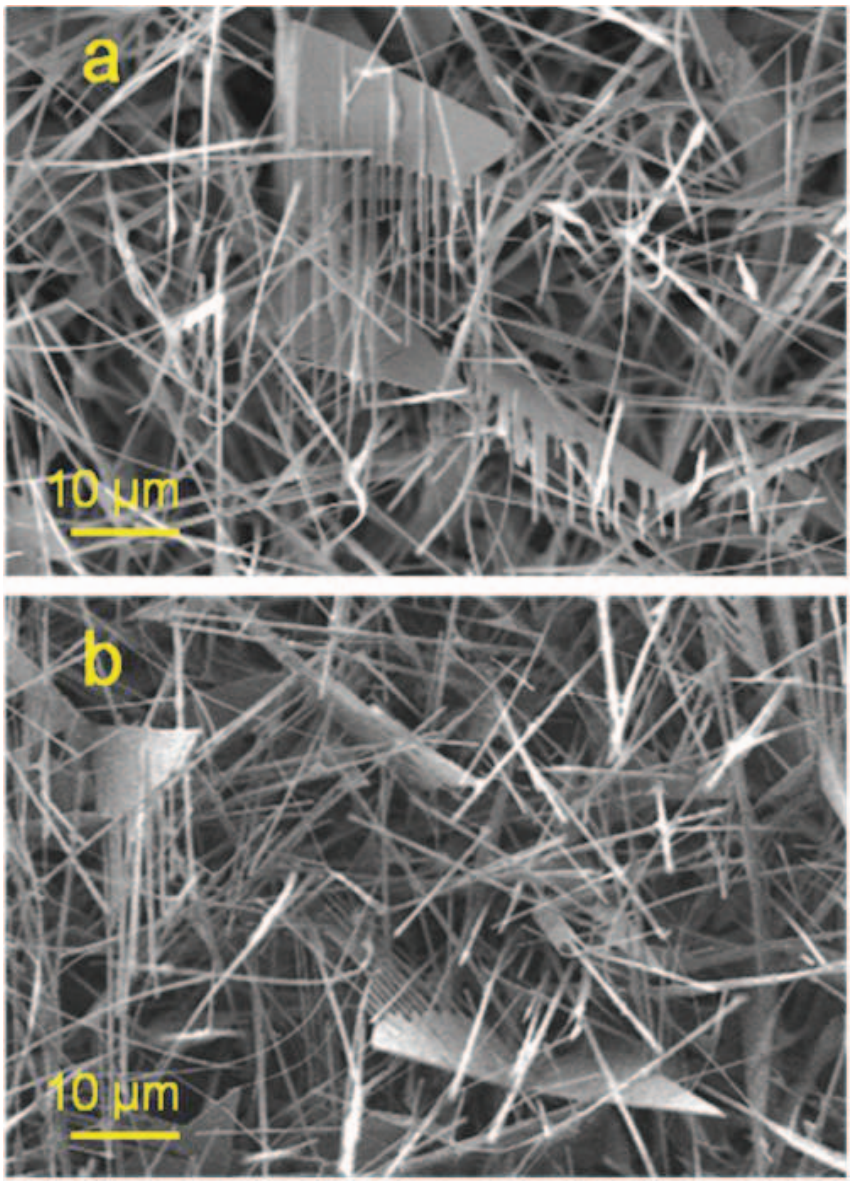

Figure 4.7: SEM images of ZnO nanocombs synthesized under temperature variation of (a) T=961 ℃–T=1040 ℃ and (b) T=953 ℃–T=1034 ℃ by the VLS method on Si (111) substrates.

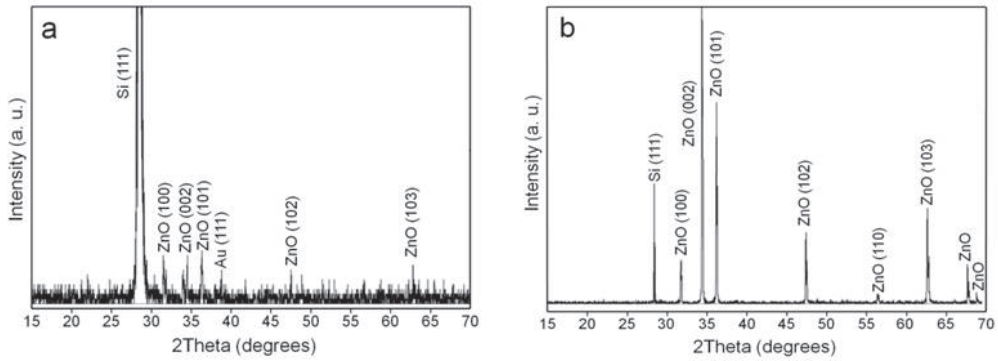

Figure 4.8: XRD-Patterns of ZnO nanostructures synthesized on Si (111) substrates. (a) Nanowalls grown at T=1130 ℃ in the center of the furnace. (b) Nanocombs grown under temperature variation of T=961 ℃–T=1040 ℃ in the downstream zone.

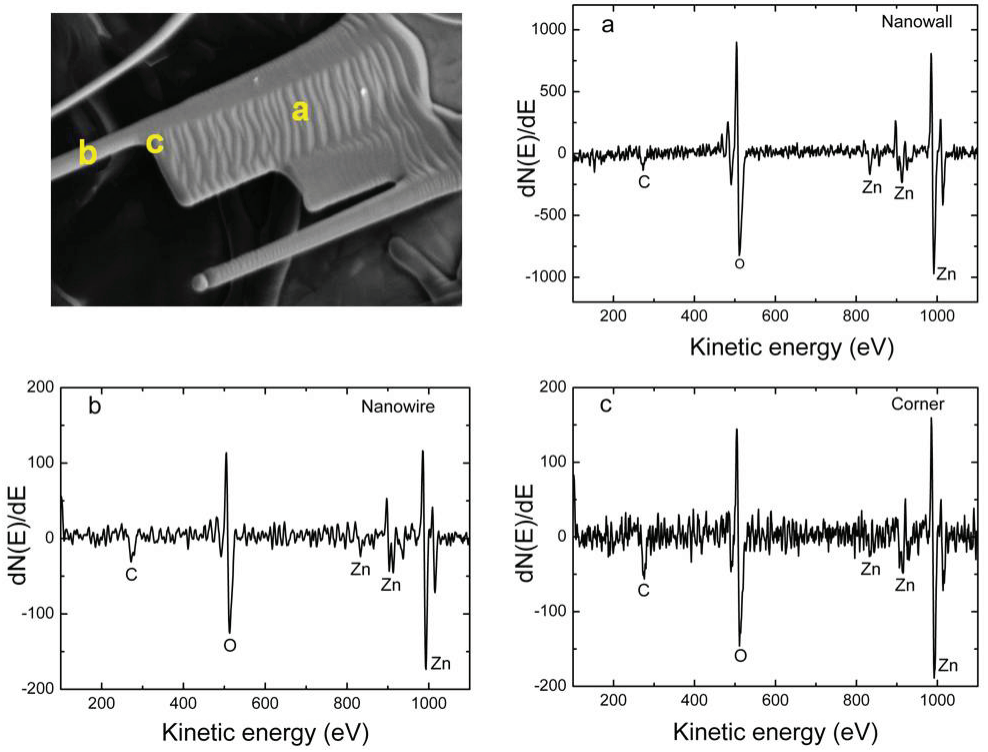

Figure 4.9: AES-Spectra of the ZnO nanowall grown at T=1130 ℃ in the center of the furnace on Si (111) substrate on (a) the wall position, (b) the nanowire position and (c) the facet (corner) between the nanowire and the nanowall. The measured positions a, b and c are shown in the SEM image of the nanowall.

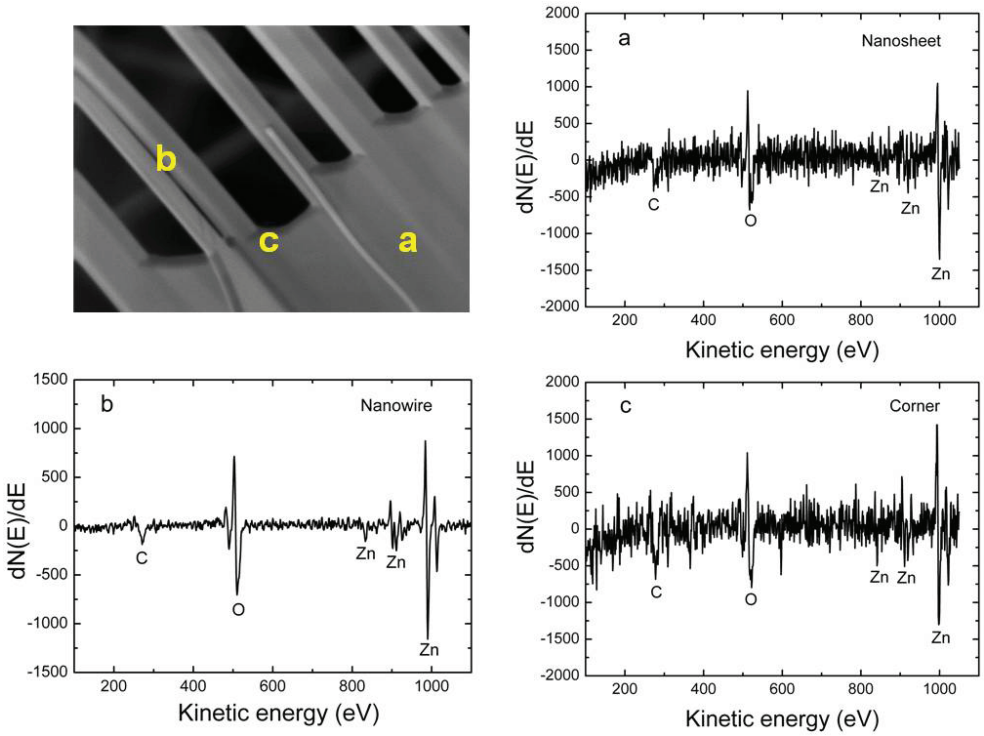

Figure 4.10: AES-Spectra of ZnO nanocombs grown under temperature variation of T=961 ℃–T=1040 ℃ in the downstream zone of the furnace on Si (111) substrate on (a) the sheet position, (b) the nanowire position and (c) the facet (corner) between the nanowire and the nanosheet. The measured positions a, b and c are shown in the SEM image of the nanocomb.

the same atomic rate within the nanowall body, but zinc has a slightly larger atomic rate than oxygen within both nanowire and facet (corner) between the nanowire side and the nanowall side. For the case of nanocombs, as can be seen in Figure 4.10, zinc has a larger atomic rate within the whole structure, especially, within the nanowire and the corner between the nanowire side and the backbone nanosheet. Moreover, the carbon peaks demonstrate the contaminations on the ZnO nanostructure surfaces. As already mentioned, the ZnO structures are synthesized by the reduction process of CO into C (Zn + CO $\rightarrow$ ZnO + C). Therefore, there should be no carbon contaminations within the ZnO structures. The carbon peaks may arise from CO molecules adsorbed on the polar ZnO surfaces, due to their van der Waals attractions [VS03].

In summary, ZnO nanocombs and nanowalls can be synthesized by the VLS method too. Using the molar ratio ZnO: C (2: 3) instead of the standard molar ratio (1: 1) by the VLS method, a high zinc vapor pressure can be achieved, which is essential for the growth of ZnO nanocombs. It seems that the temperature variation has an important role for the formation of nanocomb structures by the VLS method. A systematic study should be done to deeper understanding of the influence of growth parameters on the morphology of nanowalls and nanocombs. This enables the further development of the VLS method specially for the growth of ZnO nanocomb structures. The controlling of the growth process is important to advance the functional devices based on the ZnO multi-dimensional nanostructures.

4.3 Modeling the growth of ZnO nanocombs

In this section, a model for the growth of ZnO nanocombs based on the piezoelectric character of ZnO is developed that explains the periodic growth of nanowire branches of a nanocomb on the polar +(0001) surface of a ZnO nanobelt as a self catalytic growth process. In this model the perturbation and elasticity theory are applied to approximate the induced strain distribution in the ZnO nanobelt under the growth kinetics. The coupling of the mechanical strain to the piezoelectric field across the nanobelt thickness leads to periodic vertical displacements along the nanobelt length, which are the preferred places for the self catalytic growth of the nanowire branches for building a nanocomb structure.

A static piezoelectric system can be completely described with the following equations along with appropriate boundary conditions [SPT70]: Gauss equation for the electric field (4.1), the mechanical equilibrium equation (4.2), the constitutive equation (4.3) and the compatibility equation (4.7). By assuming no free charge ρ_{ext} in the volume of the nanobelt, the electric displacement $\vec{D}$ must satisfy the Gauss equation

$$\vec{\nabla}.\vec{D} = \rho_{ext} = 0. \tag{4.1}$$

The mechanical equilibrium condition when there is no external body force $\vec{f}_{ext} = \vec{0}$ acting on the nanobelt (neglecting the weight of the nanobelt) is

$$\vec{\nabla}.\vec{\sigma} = \vec{f}_{ext} = \vec{0}. \tag{4.2}$$

where $\vec{\sigma}$ is the stress tensor, which is related to strain $\vec{\varepsilon}$, electric field $\vec{E}$, and electric displacement $\vec{D}$ by constitutive equations (refer to section 2.3)

$$\begin{cases} \sigma_p = c_{pq}\varepsilon_q - e_{kp}^T E_k \\ D_i = e_{iq}\varepsilon_q + k_{ik}E_k. \end{cases} \tag{4.3}$$

Here, c_{pq} is the linear elastic constant, e_{kp} is the linear piezoelectric coefficient, e_{kp}^T is the transpose of the element e_{kp} and k_{ik} is the dielectric constant of the material. For a ZnO crystal with the $C_{6\nu}$ symmetry, c_{pq}, e_{kp}, and k_{ik} can be written as

$$c_{pq} = \begin{pmatrix} c_{11} & c_{12} & c_{13} & 0 & 0 & 0 \\ c_{12} & c_{11} & c_{13} & 0 & 0 & 0 \\ c_{13} & c_{13} & c_{33} & 0 & 0 & 0 \\ 0 & 0 & 0 & c_{44} & 0 & 0 \\ 0 & 0 & 0 & 0 & c_{44} & 0 \\ 0 & 0 & 0 & 0 & 0 & (c_{11}-c_{12})/2 \end{pmatrix} \tag{4.4}$$

$$e_{kp} = \begin{pmatrix} 0 & 0 & 0 & 0 & e_{15} & 0 \\ 0 & 0 & 0 & e_{15} & 0 & 0 \\ e_{31} & e_{31} & e_{33} & 0 & 0 & 0 \end{pmatrix} \tag{4.5}$$

$$k_{ik} = \begin{pmatrix} k_{11} & 0 & 0 \\ 0 & k_{11} & 0 \\ 0 & 0 & k_{33} \end{pmatrix} \tag{4.6}$$

The compatibility equation is a geometrical constraint that must be satisfied by the strain ε_{ij} [SPT70],

$$\begin{cases} \dfrac{\partial^2 \varepsilon_i}{\partial x_j^2} + \dfrac{\partial^2 \varepsilon_j}{\partial x_i^2} = \dfrac{\partial^2 \varepsilon_{ij}}{\partial x_i \partial x_j} \\ 2\dfrac{\partial^2 \varepsilon_i}{\partial x_j \partial x_k} = \dfrac{\partial}{\partial x_i}(-\dfrac{\partial \varepsilon_{jk}}{\partial x_i} + \dfrac{\partial \varepsilon_{ik}}{\partial x_j} + \dfrac{\partial \varepsilon_{ij}}{\partial x_k}) \end{cases} \tag{4.7}$$

4.3.1 Perturbation Theory

In order to simplify the analytical solution of above equations, one can apply the perturbation expansion of the linear equations introduced by Wang and Gao [YG07]: The different orders of coupling between mechanical field and electric field are achieved by introducing a perturbation parameter λ in the constitutive equations (4.3). When $\lambda = 1$, it corresponds to the real material. When $\lambda = 0$, there is a situation of no coupling between mechanical field and electric field. For virtual materials with $0 < \lambda < 1$ and piezoelectric coefficient $\tilde{e}_{kp} = \lambda e_{kp}$, both mechanical and electric field are functions of the parameter λ, which can be written in an expansion form

$$\begin{aligned} \sigma_p^{(\lambda)} &= \sum_{n=0}^{\infty} \lambda^n \sigma_p^{(n)}, \quad \varepsilon_q^{(\lambda)} = \sum_{n=0}^{\infty} \lambda^n \varepsilon_q^{(n)} \\ E_k^{(\lambda)} &= \sum_{n=0}^{\infty} \lambda^n E_k^{(n)}, \quad D_i^{(\lambda)} = \sum_{n=0}^{\infty} \lambda^n D_i^{(n)} \end{aligned} \tag{4.8}$$

By substituting equations (4.8) into equations (4.3) and comparing the terms in the equations that have the same order of λ, the first two orders of these perturbation equations are given as follows [YG07]:

$$\sigma_p^{(0)} = c_{pq} \varepsilon_q^{(0)} \tag{4.9}$$

$$D_i^{(0)} = k_{ik} E_k^{(0)} \tag{4.10}$$

$$\sigma_p^{(1)} = c_{pq} \varepsilon_q^{(1)} - e_{kp}^T E_k^{(0)} \tag{4.11}$$

$$D_i^{(1)} = e_{iq} \varepsilon_q^{(0)} + k_{ik} E_k^{(1)} \tag{4.12}$$

In this work the solutions of the first two orders are considered for the case of a

ZnO nanobelt. As mentioned already in section 4.1, the ZnO backbone nanobelt grows preferentially along either $[2\bar{1}\bar{1}0]$ or $[01\bar{1}0]$, with its top/bottom surface $\pm(0001)$. The polar surfaces $\pm(0001)$ at the top and bottom end of the nanobelt, are terminated by Zn^{2+} and O^{2-} ions. These polar surfaces (spontaneous polarization) introduce an intrinsic electric field $E_k^{(0)}$ inside of the nanobelt. For the case of a thick nanobelt, i.e. with a large distance between its polar surfaces as depicted in Figure 4.11, $E_k^{(0)}$ and its contribution to the coupling between mechanical field and electric field is ignored. Consequently one can take $\sigma_p^{(1)} = 0$, $\varepsilon_q^{(1)} = 0$ in equation (4.11). Thus in the free standing ZnO nanobelt, the first two orders of the perturbation equations become

$$\sigma_p^0 = c_{pq}\varepsilon_q^0 \tag{4.13}$$

$$D_i^{(1)} = e_{iq}\varepsilon_q^{(0)} + k_{ik}E_k^{(1)} \tag{4.14}$$

The zeroth order solution is a purely mechanical deformation depending on the growth kinetics and the first order solution is the result of the direct piezoelectric effect meaning that the mechanical deformation in the material induces an electric field in the nanobelt.

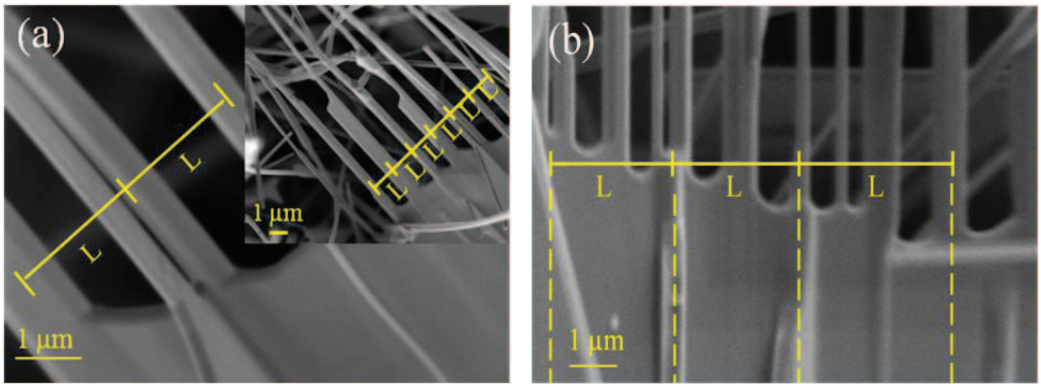

Figure 4.11: SEM images of two ZnO nanocombs synthesized on Si (111) substrate by VLS method. L is the periodicity of the nanowires branches. The ZnO nanocombs in (a) and (b) have a different geometry: (a) L=2.10 µm and (b) L=2.76 µm.

4.3.2 Theory of elasticity

Because of the small displacement ($\varepsilon_z = \frac{\triangle \mathrm{h}}{2\mathrm{H}} \simeq 3\%$) (see Figure 4.12 for the definition of $\triangle$h and H) in the backbone nanobelt shown in Figure 4.11b, the infinitesimal strain theory is used. Mao et al. [SXM03] have reported that for the ZnO nanobelt, which is grown along the [0001] direction and enclosed by the $(01\bar{1}0)$, the hardness along [0001] may be higher than that along $[2\bar{1}\bar{1}0]$. But to simplify the analytical solution the ZnO nanobelt is approximated as an isotropic elastic material with Young's modulus Ę and Poisson ratio ν. The strain and stress relation (Hooke's law) is written [YG07]

$$\begin{pmatrix} \varepsilon_x^{(1)} \\ \varepsilon_y^{(1)} \\ \varepsilon_z^{(1)} \\ \gamma_{yz}^{(1)} \\ \gamma_{zx}^{(1)} \\ \gamma_{xy}^{(1)} \end{pmatrix} = \frac{1}{\text{Ę}} \begin{pmatrix} 1 & -\nu & -\nu & 0 & 0 & 0 \\ -\nu & 1 & -\nu & 0 & 0 & 0 \\ -\nu & -\nu & 1 & 0 & 0 & 0 \\ 0 & 0 & 0 & 2(1+\nu) & 0 & 0 \\ 0 & 0 & 0 & 0 & 2(1+\nu) & 0 \\ 0 & 0 & 0 & 0 & 0 & 2(1+\nu) \end{pmatrix} \begin{pmatrix} \sigma_x^{(1)} \\ \sigma_y^{(1)} \\ \sigma_z^{(1)} \\ \tau_{yz}^{(1)} \\ \tau_{zx}^{(1)} \\ \tau_{xy}^{(1)} \end{pmatrix} \tag{4.15}$$

Where σ is the notation for the stress components acting perpendicular to the sides of the nanobelt parallel to cartesian coordinate axes x, y, z (normal stress). τ is the notation for the stress components acting tangential to the sides of the nanobelt (shear stress). The first subscript letter for the shearing stress indicates the direction of the normal to the side under consideration and the second one indicates the direction of the stress component. Here ε is the notation for the components of the normal strain and γ is the notation for the components of the shear strain in the same manner.

To further simplify, it is assumed that the nanobelt has its edges parallel to two perpendicular axes y and z of elastic symmetry with a uniform rectangular cross section. The coordinate axes are chosen as shown in Figure 4.12. The black line in this figure shows the primary nanobelt with a thickness of 2H and the dashed line shows the final geometry of the nanocomb. The position of facets at the nanowire-side is indicated with distances a and e, and the position of facets at the nanobelt-side with distances b and d. The distance between two neighboring nanowires is shown with ℓ and the periodicity of the repeating unit of nanowires with L (L=2ℓ). Because of the small width of the nanobelt along x-axis in comparison to its thickness of 2H along z-axis (see Figure 4.11 too) the problem can be treated as a case of the plane stress ($\sigma_x^{(0)} = 0, \tau_{zx}^{(0)} = \tau_{xy}^{(0)} = 0$).

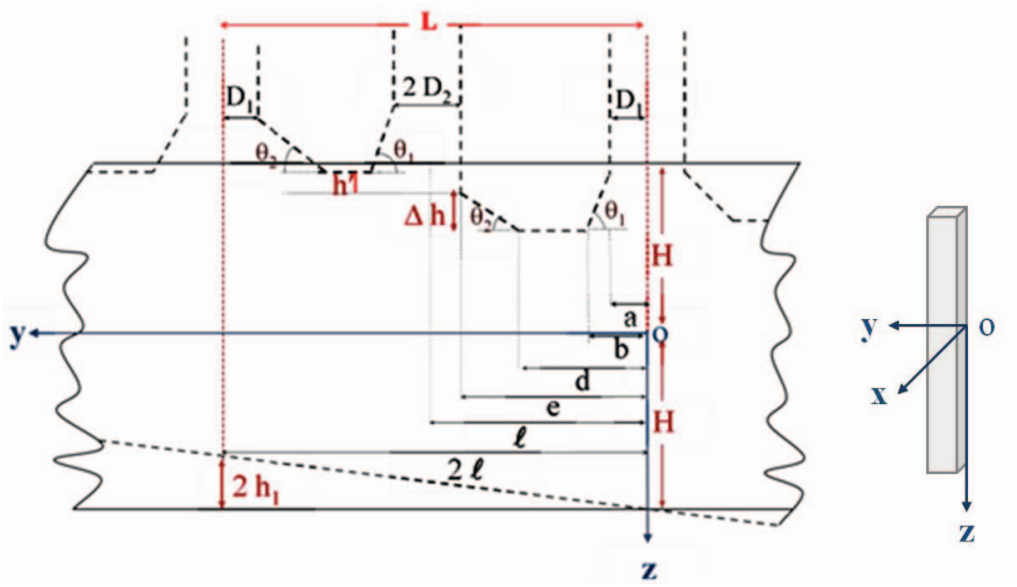

Figure 4.12: Coordinate system and schematic geometry of the ZnO nanocomb in two dimensions. The black line shows the primary nanobelt with a thickness of 2H and the dashed line shows the final geometry of the nanocomb. L is the periodicity of the repeating unit of nanowires grown on the top polar +(0001) surface of the nanobelt.

For the state of the plane stress, the solution of two-dimensional problems reduces to the integration of the differential equations of equilibrium (4.2) together with the compatibility equations (4.7) and the stress function, ϕ, must satisfy the differential equation [SPT70]:

$$\frac{\partial^4\phi}{\partial y^4} + 2\frac{\partial^4\phi}{\partial y^2\partial z^2} + \frac{\partial^4\phi}{\partial z^4} = -(1-\nu)\left(\frac{\partial^2\vartheta}{\partial y^2} + \frac{\partial^2\vartheta}{\partial z^2}\right) \tag{4.16}$$

In which ϑ is the potential function of the external body force. The stress components are given by the equations

$$\sigma_y - \vartheta = \frac{\partial^2\phi}{\partial z^2}, \quad \sigma_z - \vartheta = \frac{\partial^2\phi}{\partial y^2}, \quad \tau_{yz} = -\frac{\partial^2\phi}{\partial y\partial z} \tag{4.17}$$

When there is no body force, the right-hand side of equation (4.16) reduces to zero

$$\frac{\partial^4\phi}{\partial y^4} + 2\frac{\partial^4\phi}{\partial y^2\partial z^2} + \frac{\partial^4\phi}{\partial z^4} = 0 \tag{4.18}$$

Equation (4.18) may be satisfied by functions ϕ_n in the form

$$\phi_n = f_n(z)\cos\frac{n\pi y}{\mathrm{L}}, \quad n = 1, 2, 3, ... \tag{4.19}$$

In which $f_n(z)$ is a function of z only. Substituting equation (4.19) into equation (4.18) and using the notation $\frac{n\pi}{\mathrm{L}} = \alpha$, one finds the following equation for determining $f_n(z)$:

$$\alpha^4 f_n(z) - 2\alpha^2\frac{d^2 f_n(z)}{dz^2} + \frac{d^4 f_n(z)}{dz^4} = 0 \tag{4.20}$$

The general integral of this linear differential equation with constant coefficients is

$$f_n(z) = A_n\cosh\alpha z + B_n\sinh\alpha z + C_n z\cosh\alpha z + D_n z\sinh\alpha z \tag{4.21}$$

The stress function is then obtained by substituting equation (4.21) into equation (4.19) and consequently, from equation (4.17) one takes

$$\begin{aligned}\sigma_y = \sum_{n=1}^{\infty}\sigma_y^{(n)} = \sum_{n=1}^{\infty}\frac{\partial^2\phi_n}{\partial z^2} = \sum_{n=1}^{\infty}\cos\alpha y[A_n\alpha^2\cosh\alpha z + B_n\alpha^2\sinh\alpha z \\ + C_n\alpha(2\sinh\alpha z + \alpha z\cosh\alpha z) + D_n\alpha(2\cosh\alpha z + \alpha z\sinh\alpha z)]\end{aligned} \tag{4.22}$$

$$\begin{aligned}\sigma_z = \sum_{n=1}^{\infty}\sigma_z^{(n)} = \sum_{n=1}^{\infty}\frac{\partial^2\phi_n}{\partial y^2} = -\sum_{n=1}^{\infty}\cos\alpha y[A_n\alpha^2\cosh\alpha z + B_n\alpha^2\sinh\alpha z \\ + C_n\alpha^2 z\cosh\alpha z + D_n\alpha^2 z\sinh\alpha z]\end{aligned} \tag{4.23}$$

$$\tau_{yz} = \sum_{n=1}^{\infty} \tau_{yz}^{(n)} = -\sum_{n=1}^{\infty} \frac{\partial^2 \phi_n}{\partial y \partial z} = \sum_{n=1}^{\infty} \sin \alpha y [A_n \alpha^2 \sinh \alpha z + B_n \alpha^2 \cosh \alpha z + C_n \alpha (\cosh \alpha z + \alpha z \sinh \alpha z) + D_n \alpha (\sinh \alpha z + \alpha z \cosh \alpha z)] \quad (4.24)$$

where the constants A_n, B_n, C_n, and D_n are determined from the conditions on the upper and lower edges of the nanobelt, $z = \pm \mathrm{H}$.

4.3.3 Fourier series

In the most general case the distribution of vertical loading along the upper and lower edges of a beam can be expressed as Fourier series

$$q_{upper}(y) = a_0 + \sum_{n=1}^{\infty} a_n \cos \alpha y + \sum_{n=1}^{\infty} a'_n \sin \alpha y \quad (4.25)$$

$$q_{lower}(y) = b_0 + \sum_{n=1}^{\infty} b_n \cos \alpha y + \sum_{n=1}^{\infty} b'_n \sin \alpha y \quad (4.26)$$

Here

$$a_0 = \frac{1}{\mathrm{L}} \int_0^{\mathrm{L}} q_{upper}(y) dy, \quad b_0 = \frac{1}{\mathrm{L}} \int_0^{\mathrm{L}} q_{lower}(y) dy,$$

$$a_n = \frac{2}{\mathrm{L}} \int_0^{\mathrm{L}} q_{upper}(y) \cos \alpha y dy, \quad a'_n = \frac{2}{\mathrm{L}} \int_0^{\mathrm{L}} q_{upper}(y) \sin \alpha y dy,$$

$$b_n = \frac{2}{\mathrm{L}} \int_0^{\mathrm{L}} q_{lower}(y) \cos \alpha y dy, \quad b'_n = \frac{2}{\mathrm{L}} \int_0^{\mathrm{L}} q_{lower}(y) \sin \alpha y dy.$$

The constant terms a_0, b_0 represent uniform loadings in the z direction and produce constant stresses $\sigma_y^{(0)} = c_0, \sigma_z^{(0)} = f_0, \tau_{yz}^{(0)} = d_0$. The stresses produced by terms containing $\cos \alpha y$ are obtained from equations (4.22), (4.23), and (4.24). By exchanging $\cos \alpha y$ for $\sin \alpha y$ and changing the sign of τ_{yz} in these equations one obtains the stresses produced

by terms containing $\sin \alpha y$ too. Thus for the case of the nanocomb one has

$$\sigma_y = c_0 + \sum_{n=1}^{\infty} \cos \alpha y [A_n \alpha^2 \cosh \alpha z + B_n \alpha^2 \sinh \alpha z + C_n \alpha (2 \sinh \alpha z + \alpha z \cosh \alpha z) + D_n \alpha (2 \cosh \alpha z + \alpha z \sinh \alpha z)] + \sum_{n=1}^{\infty} \sin \alpha y [A'_n \alpha^2 \cosh \alpha z + B'_n \alpha^2 \sinh \alpha z + C'_n \alpha (2 \sinh \alpha z + \alpha z \cosh \alpha z) + D'_n \alpha (2 \cosh \alpha z + \alpha z \sinh \alpha z)] \tag{4.27}$$

$$\sigma_z = f_0 - \sum_{n=1}^{\infty} \cos \alpha y [A_n \alpha^2 \cosh \alpha z + B_n \alpha^2 \sinh \alpha z + C_n \alpha^2 z \cosh \alpha z + D_n \alpha^2 z \sinh \alpha z] - \sum_{n=1}^{\infty} \sin \alpha y [A'_n \alpha^2 \cosh \alpha z + B'_n \alpha^2 \sinh \alpha z + C'_n \alpha^2 z \cosh \alpha z + D'_n \alpha^2 z \sinh \alpha z] \tag{4.28}$$

$$\tau_{yz} = d_0 + \sum_{n=1}^{\infty} \sin \alpha y [A_n \alpha^2 \sinh \alpha z + B_n \alpha^2 \cosh \alpha z + C_n \alpha (\cosh \alpha z + \alpha z \sinh \alpha z) + D_n \alpha (\sinh \alpha z + \alpha z \cosh \alpha z)] - \sum_{n=1}^{\infty} \cos \alpha y [A'_n \alpha^2 \sinh \alpha z + B'_n \alpha^2 \cosh \alpha z + C'_n \alpha (\cosh \alpha z + \alpha z \sinh \alpha z) + D'_n \alpha (\sinh \alpha z + \alpha z \cosh \alpha z)] \tag{4.29}$$

From the strain-displacement relationships and the Hooke's law, the following equations can be obtained [SPT70]:

$$\text{Ę} V = \int (\sigma_y - \nu \sigma_z) dy + \text{Ę} k_0 z + k_1 \tag{4.30}$$

$$\text{Ę} W = \int (\sigma_z - \nu \sigma_y) dz - \text{Ę} k_0 y + k_2 \tag{4.31}$$

$$\gamma_{yz} = \frac{\tau_{yz}}{G} = \frac{\partial V}{\partial z} + \frac{\partial W}{\partial y} \tag{4.32}$$

$$G = \frac{\text{Ę}}{2(1+\nu)} \tag{4.33}$$

where V and W are the displacement components parallel to the coordinate axes y and

z, respectively. k_0, k_1 and k_2 are the constants, which are determined from the known displacements at the ends of the nanobelt. The constant G is called shear modulus or the modulus of rigidity. γ_{yz} is the distortion of the angle between the intersecting sides xz and xy.

4.3.4 Electromechanical coupling in ZnO nanocombs

By controlling the growth kinetics, ZnO comb-like nanostructures with a variety of periodicity and geometrical shapes, can be synthesized [YSL06, KY08b, ZWP05]. For each ZnO nanocomb the periodicity of its nanowire branches (length L in Figure 4.12), the position of facets at the nanowire-side (lengths a and e in Figure 4.12) and the position of facets at the nanobelt-side (lengths b and d in Figure 4.12) determine the appropriate boundary conditions uniquely. As an example of a real structure, the ZnO nanocomb shown in Figure 4.11b is considered, which represents a more general deformation in the crystal structure of the primary nanobelt. In this case the boundary conditions are taken as follows:

$$
\begin{aligned}
&V(0,z) = 0, \quad V(2\ell,z) = constant, \quad W(y,+\mathrm{H}) = -\frac{\mathrm{h}_1}{\ell} y,\\
&W(2\ell,z) = -2\mathrm{h}_1, \quad W(0,-\mathrm{H}) = 0,\\
&W(\ell+\mathrm{d},-\mathrm{H}) - W(\mathrm{e},-\mathrm{H}) = -\mathrm{h}',\\
&W(\mathrm{e},-\mathrm{H}) - W(\mathrm{d},-\mathrm{H}) = W(\ell+\mathrm{e},-\mathrm{H}) - W(\ell+\mathrm{d},-\mathrm{H}),\\
&W(\mathrm{a},-\mathrm{H}) - W(\mathrm{b},-\mathrm{H}) = W(\ell+\mathrm{a},-\mathrm{H}) - W(\ell+\mathrm{b},-\mathrm{H}),\\
&W(\mathrm{b},-\mathrm{H}) - W(\mathrm{d},-\mathrm{H}) = W(\ell+\mathrm{b},-\mathrm{H}) - W(\ell+\mathrm{d},-\mathrm{H}).
\end{aligned}
\tag{4.34}
$$

From these boundary conditions and equilibrium equations $\sum \mathrm{F}_y = 0$, $\sum \mathrm{F}_z = 0$ for the force components in y- and z-direction the constants $A_n, B_n, C_n, D_n, A'_n, B'_n, C'_n, D'_n, c_0, f_0, d_0$ in equations (4.27), (4.28), (4.29) and the constants k_0, k_1, k_2 in equations (4.30), (4.31), (4.32) are derived. Consequently, by substituting equations (4.27), (4.28), (4.29) into equations (4.15), the strain distribution in the nanobelt is determined. From the first two boundary conditions one finds that n in the Fourier expansions (4.27), (4.28), (4.29) must be an even number.

With taking $n = 2$ the solution for the first three orders can be approximated. Using the Wolfram Mathematica 8.0 the strain distribution in the ZnO nanobelt is simulated

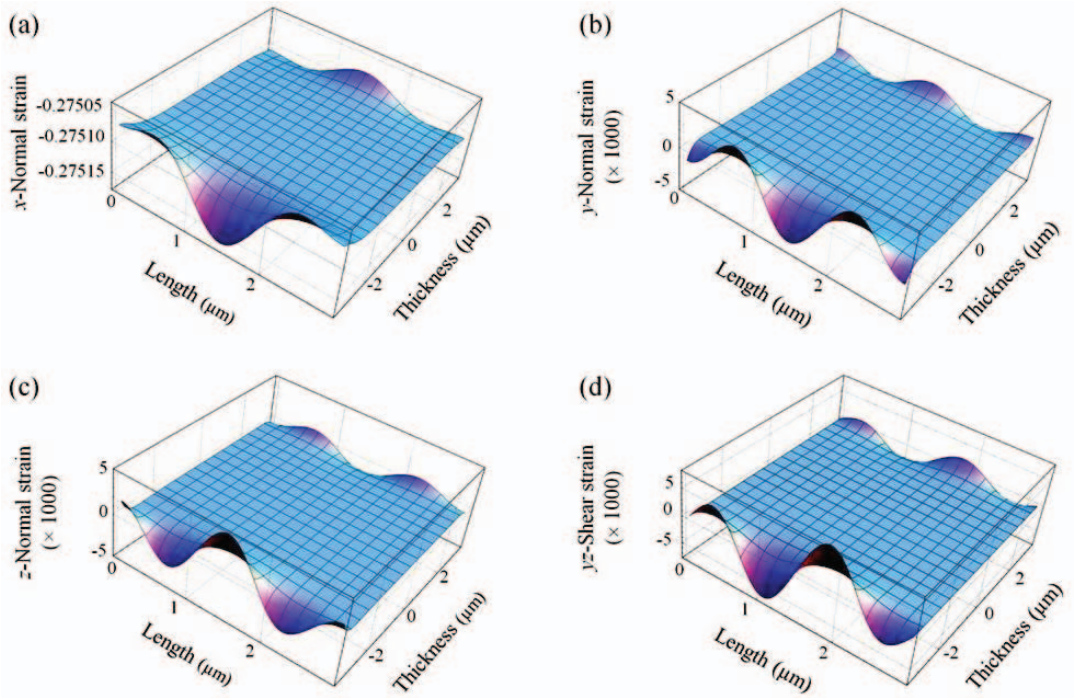

Figure 4.13: Induced strain in the primary nanobelt for the ZnO nanocomb shown in Figure 4.11b. The components of the normal strain in (a) x-, (b) y-, (c) z-direction and (d) the shear strain in the nanobelt.

as shown in Figure 4.13. The values given in Table 4.1 for E and ν are used in present calculations. In the problem of plane stress ($\sigma_x^{(0)} \sim 0$) for the ZnO nanocomb a non zero strain $\varepsilon_x^{(0)}$ across the width of the nanobelt is to be calculated (Figure 4.13a). This is caused by the normal stress components $\sigma_y^{(0)}$ and $\sigma_z^{(0)}$. The positive strain is corresponding to the induced tension and the negative strain to the induced compression in the nanobelt. Now by using the perturbation approximation in equation (4.14) one obtains the induced piezoelectric field $E_k^{(1)}$ in the ZnO nanobelt. By noting that there is no free body charge in the nanobelt one takes

$$0 = \nabla . e_{iq} \varepsilon_q^{(0)} + \nabla . k_{ik} E_k^{(1)} \tag{4.35}$$

in which

$$\nabla . e_{iq} \varepsilon_q^{(0)} = \frac{\partial}{\partial y} e_{15} \gamma_{yz}^{(0)} + \frac{\partial}{\partial z} (e_{31} \varepsilon_x^{(0)} + e_{31} \varepsilon_y^{(0)} + e_{33} \varepsilon_z^{(0)}) \tag{4.36}$$

$$\nabla.k_{ik}E_k^{(1)} = \frac{\partial}{\partial x}k_{11}E_x^{(1)} + \frac{\partial}{\partial y}k_{11}E_y^{(1)} + \frac{\partial}{\partial z}k_{33}E_z^{(1)} \tag{4.37}$$

By using $\vec{E} = -\vec{\nabla}\varphi^{(1)}$ in equation (4.37) one obtains

$$\nabla.k_{ik}E_k^{(1)} = -k_{11}\frac{\partial^2\varphi^{(1)}}{\partial x^2} - k_{11}\frac{\partial^2\varphi^{(1)}}{\partial y^2} - k_{33}\frac{\partial^2\varphi^{(1)}}{\partial z^2} \tag{4.38}$$

Since the $\nabla.e_{iq}\varepsilon_q^{(0)}$ is independent of x, the induced piezoelectric potential $\varphi^{(1)}$ is uniform in x direction. In addition, because of the Fourier series expansion of $\nabla.e_{iq}\varepsilon_q^{(0)}$, one can take $\varphi^{(1)}$ as a Fourier series expansion, which satisfies the Maxwell's law $\vec{\nabla} \times \vec{E}^{(1)} = \vec{0}$ too:

$$\varphi^{(1)} = \sum_{n=1}^{\infty} S_n(z)\sin\alpha y + \sum_{n=1}^{\infty} T_n(z)\cos\alpha y \tag{4.39}$$

Here $S_n(z)$ and $T_n(z)$ are functions of z. By substituting equation (4.39) into equation (4.38) and solving equation (4.35) for the electric potential inside the nanobelt and the Laplace equation for the electric potential outside the nanobelt one obtains the induced piezoelectric potential and consequently the piezoelectric field in the nanobelt (Figure 4.14a and 4.14b). The values given in the Table 4.1 for the constants e_{kp} and k_{ik} are used in this calculation. From Figure 4.13 and Figure 4.14a one sees the induced strain and electric potential within the nanobelt are noticeable only in the first layers under the top and bottom surfaces. A comparison between the induced electric potential distribution (Figure 4.14a) and the normal strain distribution in z-direction in the nanobelt (Figure 4.13c) indicates that positive and negative electric potentials are generated in the regions stretched and compressed along the polar axis of the nanobelt, respectively. The induced piezoelectric field distribution in the ZnO nanobelt is consistent with the mechanical deflection distribution in the material. This is shown for example in Figure 4.14b and Figure 4.14c only for the first layers under the top polar +(0001) surface of the nanobelt.

The red dashed line in Figure 4.14c shows schematically the expected geometry of the final nanostructure, which does not match exactly the geometry of the nanocomb shown in Figure 4.12. This is because of the fact that in present calculations only the first three orders in the Fourier expansions (4.27), (4.28), (4.29) are taken into account. To obtain a more precise solution one needs to consider higher orders in the Fourier expansions. Thus more boundary conditions are required. This may be achieved by using

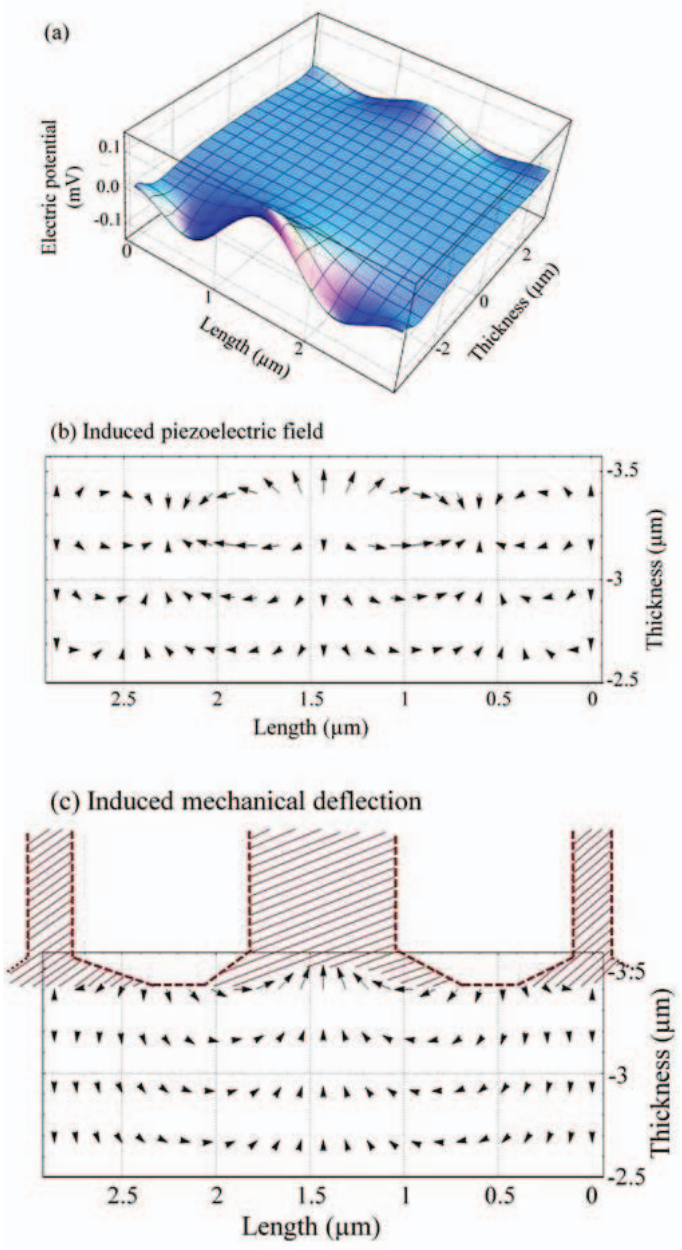

Figure 4.14: (a) Induced piezoelectric potential distribution in the primary nanobelt. (b) corresponding piezoelectric field distribution and (c) mechanical deflection in the first layers under the top polar +(0001) surface of the nanobelt at z=-H (see Figure 4.12). The red dashed line shows the schematic geometry of the final ZnO nanocomb.

Table 4.1: The elastic and electric constants for bulk ZnO [YG07]. k_{11}, k_{22} and k_{33} are the dielectric constants of the material. e_{31}, e_{33} and e_{15} are the piezoelectric coefficients. E is Young's modulus and ν is Poisson ratio.

Constant	Value	Constant	Value
k_{11}	7.77	e_{31}	-0.51
k_{22}	7.77	e_{33}	1.22
k_{33}	8.91	e_{15}	-0.45
ν	0.349	E(GPa)	129

the transmission electron microscopy (TEM) images of a nanocomb, illustrating more details about the facets at the nanowire-side and at the nanobelt-side. For the case of the nanocomb considered in this work (see Figure 4.11b), no TEM images could be taken because the structure is too thick.

4.3.5 Development of a new growth model

ZnO crystallizes in the wurtzite structure without a center of inversion (Figure 4.15a). That means by cleaving the crystal perpendicular to the c axis, two polar surfaces on opposite sides of the crystal are formed. The polar +(0001) surface has only Zn^{2+} ions and the polar −(0001) surface has only O^{2-} ions. Such a system may be considered as a "slab" of Zn-O double layers [BM03] as shown in Figure 4.15b.

The $-\nabla.e_{iq}\varepsilon_q^{(0)}$ in equation (4.35) can be considered as a body charge density and it means that actually the divergence of the strain $\varepsilon_q^{(0)}$ in the material induces a piezoelectric field $E_k^{(1)}$in the nanostructure. We call this body charge density, induced piezoelectric charge density. As shown in Figure 4.16a the induced piezoelectric charge is localized in the surface regions and decayes to zero in the middle of the nanobelt. A comparison between the induced piezoelectric charge and deflection distribution suggests a rearrangement of charges between the first Zn-O double layers under the top and bottom polar surfaces of the nanobelt. In the stretched regions of the nanobelt, the Zn-terminated side gets farther away from the O-terminated side and becomes more positively charged. On the other hand, in the compressed regions the Zn-terminated side gets closer to the O-terminated side and becomes less positively charged. It follows that the top polar +(0001) surface (at z= -H) of the nanobelt has no homogenous Zn^{2+} ion density (see Figure 4.16b). This suggests a self catalytic growth of ZnO nanowires on the polar +(0001) surface at the regions with higher positive charge density and hence more metal content compared to its

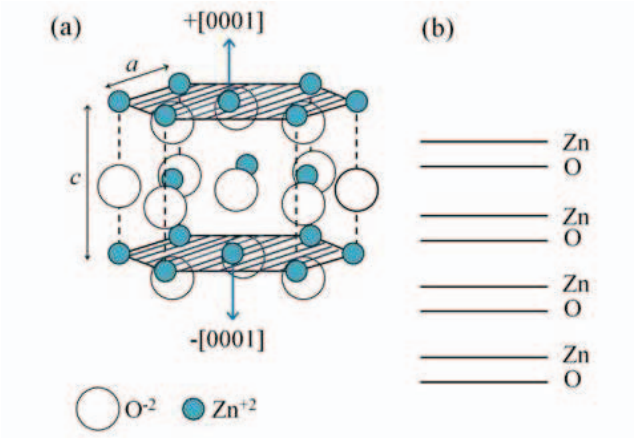

Figure 4.15: Crystal structure of ZnO. (a) Wurtzite structure of ZnO with the top polar Zn-terminated +(0001) surface and the bottom polar O-terminated −(0001) surface. a and c are the crystal parameters of ZnO. (b) Schematic illustration of Zn-O double layers in a slab of the material.

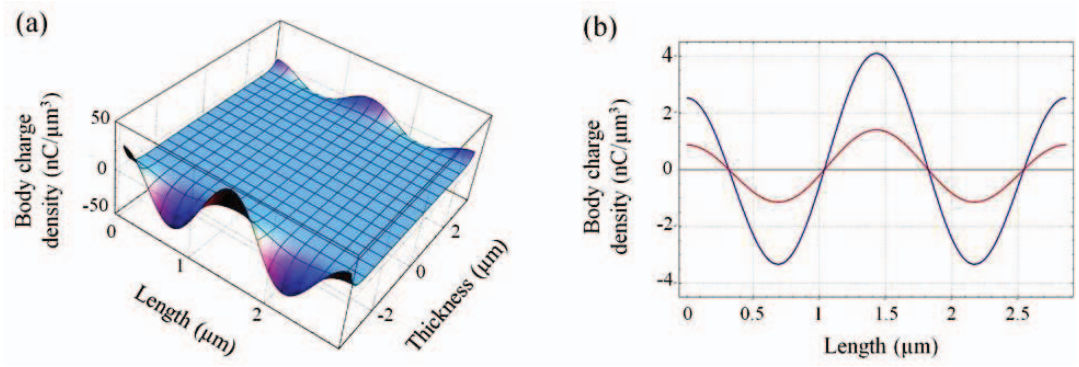

Figure 4.16: Induced piezoelectric body charge density (a) in the nanobelt (b) in the top surface layer at z=-H (blue line) and in the bottom surface layer at z=+H (red line).

vicinity. Therefore the nanowires grow periodically on the top polar surface and thus the nanobelt changes into a nanocomb. Similarly, on the bottom polar −(0001) surface (at z=+H), the O^{2-} ion density is not homogenous either (see Figure 4.16b) but this causes no metallic catalyst for the growth of ZnO nanowires. Hence the nanowire branches grow only on the top polar +(0001) surface of the nanobelt.

As mentioned already, the periodicity of the nanowire branches on the nanobelt depends on the growth kinetic control. In present experiment the Ar flow fluctuation and relatively

low carbon vapor pressure in the growth process may cause different periodicities of the nanowire branches of the same nanocomb as shown in Figure 4.11.

5 Manufacture of ZnO nanogenerators

Energy harvesting from the environment is today an important subject of research. In particular, for wireless nanodevices and nanosensors, especially biosensors, an embedded energy harvesting system is desired, so that self-powered nanodevices can oparate independently from a battery. The latter has the advantage of an extended life time and of not requiring recharging procedures [MA08]. Beside radiation (light) and thermal energy, mechanical kinetic energy is an important source in our environment. In addition to acoustic waves, noise, wind, and water, the human body provides numerous potential mechanical energy too, such as body movement, muscle stretching, blood vessel contraction, body fluid and blood flow. Mechanical energy can be harvested exploiting different transduction mechanisms based on electrostatic, electromagnetic, and piezoelectric effects. Generators based on the piezoelectric effect offer the most robust and simple solutions for mechanical energy harvesting. The main advantage of piezoelectric generators is their scalability, in that the generated power is scalable up by combining individual piezoelectric elements and the characteristic dimension is scalable down to the nanoscale [MA08]. Recently, energy harvesting from the environment using piezoelectric ZnO nanowire arrays has attracted considerable attention, due to their nanosize scale and an expected efficiency of 17% to 30%. Moreover, ZnO is relatively biosafe and biocompatible and can be used for biomedical application with little toxicity [ZLW06].

In this chapter the reported concepts of ZnO nanogenerators, their fabrication methods and proposed working mechanisms are introduced. Then the fabrication of ZnO nanogenerators by an advanced wet chemical method is reported. The advantages of this fabrication method are also pointed out.

5.1 Current state of research

5.1.1 Topical concepts of ZnO nanogenerators

By today several approaches to use piezoelectric ZnO nanowires as nanogenerators have been demonstrated. In the following these are categorized into three main groups based on their working mechanisms.

The deflected ZnO nanowires: The first concept originally was reported by Wang and Song [ZLW06] in 2006, in which vertically aligned ZnO nanowires were deflected with a conductive atomic force microscope (AFM) tip in contact mode. Figure 5.1 shows the experimental design for converting nanoscale mechanical energy into electrical energy by a vertical ZnO nanowire, as repored by Wang and Song. A Pt-coated AFM tip was used as both the actuator and the electrical measurement device. Voltage signals of U=6 mV to U=9 mV amplitude were detected only at the moments when the scanning tip snapped off the ZnO nanowires.

The proposed working mechanism is represented in Figure 5.2. The nanowire is schematically shown in Figure 5.2a. By deflecting the ZnO nanowire with an AFM tip in the direction y, a mechanical strain in the nanowire is induced. Figure 5.2b presents the induced strain distribution along its polar axis (ϵ_z) simulated for a 1 µm long nanowire with an aspect ratio of 10. Consequently, due to the piezoelectric effect negative and positive ionic charges are induced on the compressed and stretched sides, respectively. The corresponding induced piezoelectric field E_z and potential V_s distribution are simulated in

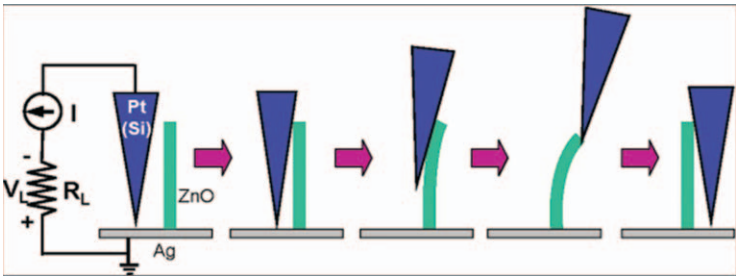

Figure 5.1: Experimental setup for generating electricity by deflecting a piezoelectric nanowire with a conductive AFM tip. The base of the nanowire is grounded and an external load of R_L is applied, which is much larger than the inner resistance of the nanowire. The AFM scans across the nanowire arrays in contact mode [ZLW06].

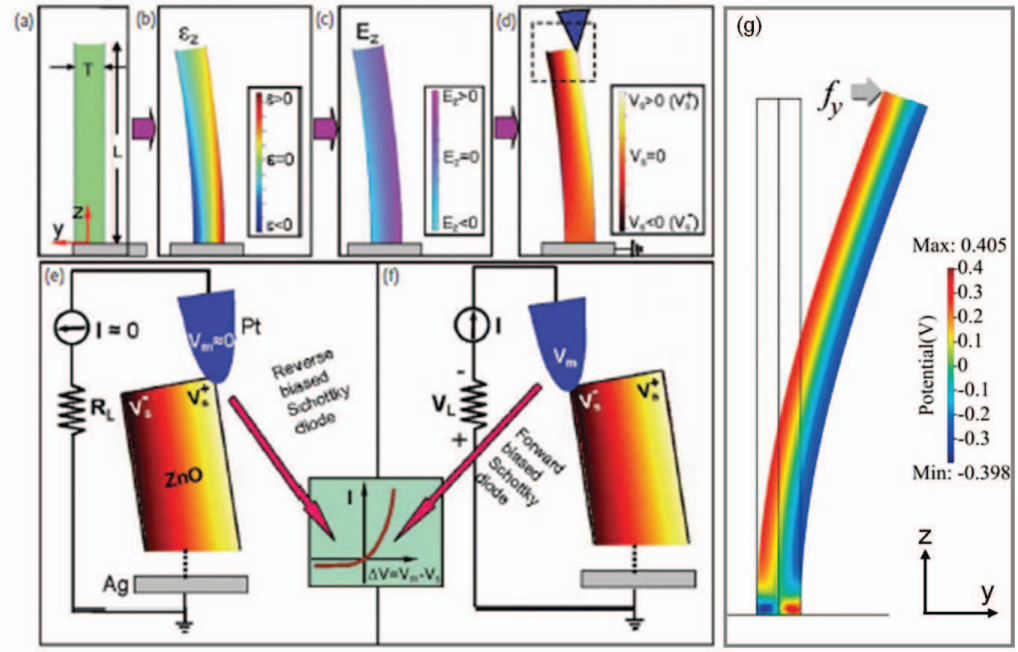

Figure 5.2: Mechanism of power generation in a ZnO nanowire. (a) Schematic of a nanowire and the coordinate system. (b) Simulation of the Longitudinal strain ϵ_z distribution in the deflected nanowire. (c) and (d) Corresponding longitudinal electric field E_z and potential V_s distribution in the nanowire induced by the piezoelectric effect, respectively. The dashed box in (d) indicates the area shown in parts (e) and (f). (e),(f) Interface between the metal AFM tip and semiconducting ZnO nanowire under local positive and negative contact potentials, showing reverse- and forward-biased Schottky rectifying behavior, respectively. Inset: typical I-V characteristic of a metal-semiconductor (n-type) Schottky barrier [ZLW06]. (g) Simulation of the induced electric potential distribution in the nanowire as an ideal insulator without free carriers. The ZnO nanowire with diameter of D=50 nm and length of L=600 nm was deflected under a lateral force of F=80 nN [YG09].

Figure 5.2c and 5.2d, respectively. Therefore, an electric potential drop develops between the top surface of ZnO nanowire and the bottom electrode. The Schottky barrier at the interface between the Pt-coated AFM tip and the ZnO nanowire (n-type semiconductor) gates and directs the flow of electrons under the driving electric potential in an external circuit. In fact, a signal can be measured only when the tip touches the compressed side of the nanowire (see Figure 5.2e and 5.2f). In other words, a current in the external circuit flows only in one direction and thus the deflected ZnO nanowire is a DC nanogenerator. The piezoelectric potential distribution induced in the deflected ZnO nanowire was also

calculated by Gao et al. [YG07, YG09] for the case of an ideal insulator (without free carriers) using the continuum mechanics, a perturbation technique [YG07] (refer to subsection 4.3.1 too) and solving the derived analytical solution with a finite element method. This is shown in Figure 5.2g.

Figure 5.3 shows three developed designs of a ZnO nanowire nanogenerator on the basis of the harvesting mechanism proposed above. In Figure 5.3a a zigzag shaped silicon electrode, which is coated with Pt acts as an array of parallel integrated metal tips. When an ultrasonic wave drives the electrode up and down the metal tips deflect the nanowires and simultaneously and continuously collect and output electricity from all of the nanowires. Because the voltages created by all of the nanowires are in parallel, the output voltage is effectively the voltage created by one nanowire. In this design, the large majority of the nanowires did not produce electricity because of their nonuniformity in height and distribution on the substrate surface, as shown in Figure 5.3b. Thus, the total output current was rather small. The total output power of the nanogenerator fabricated with a substrate of area A=2 mm^2 was reported to be $W = I_{NW}V \approx 1$ pW. In this case, the output power of one nanowire, as driven by the ultrasonic wave at $\nu \sim$41 kHz, would be $\Delta W_{wave} = 1$–4 fW. This is much smaller than the power of $\Delta W_{AFM} = 0.1$ pW generated by one nanowire, as directly deflected by an AFM tip scanning with a speed of 12.081 µm/s (see Figure 5.1 too) [XW07a]. But it must be noted that the vibrational amplitude of the nanowire was much larger for the latter case. Hsu et al. [CLH12] reported a nanogenerator driven by vibrations at low frequencies, in which Pt-coated ZnO nanowires grown on a flexible PET (polyethylene terephthalate) substrate were used as an array of parallel integrated conductive tips (Figure 5.3c). The nanogenerator with 2% compressive bending produced a piezoelectric current of approximately $I=5 \times 10^{-10}$ A without a source of vibration. The maximum piezoelectric current of the sample with 2% compressive bending under vibration at a low frequency of ν=120 Hz was measured to be about $I=2.5 \times 10^{-7}$ A, which was 4 times the current of a nonbending sample. Figure 5.3e shows another design of a ZnO nanogenerator with the same concept for the array of integrated conductive tips but with a diffent geometry of substrates. In this case, ZnO nanowires were grown radially around two textile fibres, one of which was coated with 300 nm of Au. By entangling two fibres and brushing the nanowires grown on them with respect to each other, mechanical energy was converted into electricity. The pulling and releasing of the gold-coated fibre was accomplished by a motor at a controlled frequency ($<$ 10 Hz), as shown schematically in Figure 5.3e. Qin et al. [YQ08] measured maximum short-circuit current signals of about

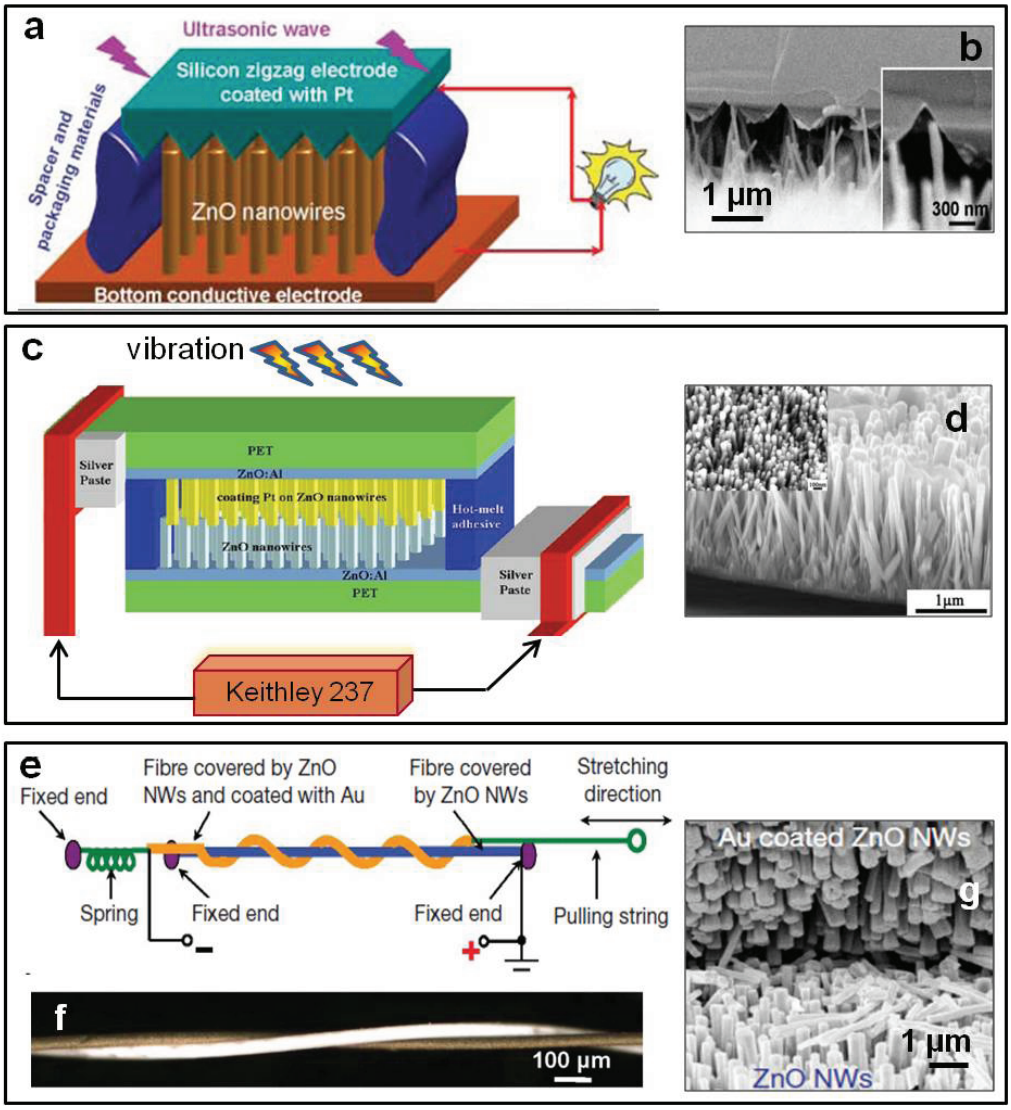

Figure 5.3: Schematic diagrams showing the design and structure of nanogenerators of vertically aligned ZnO nanowires. (a) Nanogenerator driven by an ultrasonic wave. The zigzag shaped Si top electrode, was coated with 200 nm of Pt. (b) Cross-sectional SEM image of the nanogenerator, which is composed of the zigzag electrode and aligned nanowires grown on a GaN substrate. Inset: A typical nanowire that is forced by the electrode to deflect [XW07a]. (c) Nanogenerator driven by vibration at low frequency. Aligned nanowires were grown on both the top and bottom electrodes. The nanowires on the top electrode were coated with 20 nm of Pt. (d) Cross-sectional SEM image of aligned nanowires grown on ZnO: Al-coated PET substrates. Inset: Top view SEM image of grown nanowires [CLH12]. (e) Schematic experimental set-up of the fibre-based nanogenerator driven by a low frequency, external pulling force. (f) An optical micrograph of a pair of entangled fibres, one of which is coated with Au (in darker contrast). (g) SEM image at the teeth-to-teeth interface of two fibres covered by nanowires (NWs), with the top one coated with Au. The Au-coated nanowires at the top fiber serve as an array of conductive tips that deflect the nanowires at the bottom fiber [YQ08].

I=4 nA and corresponding open voltage signals of U=1 mv –U=3 mV for double-fiber nanogenerators with an effective length of L=4 mm –L=5 mm, by applying an external pulling force at a motor speed of 80 rpm (revolutions per minute; 60 rpm = 1 Hz).

Beside ZnO nanowires, ZnO nanotubes could also be used for harvesting mechanical energy. Xi et al. [YX09] reported a piezoelectric nanogenerator, in which vertically aligned ZnO nanotubes were deflected by a Pt-coated AFM tip with the presence of a Schottky contact between the tip and the ZnO nanotubes. Output voltages from U=10 mV to U=35 mV were measured when nanotubes were deformed under a lateral force of F∼80 nN. The working mechanism agreed with that proposed for nanogenerators based on deflected nanowires (refer to Figure 5.2).

The bent ZnO nanowires: The second concept for ZnO nanowire generators was reported by Yang et al. [RY09c] in 2008, in which a piezoelectric ZnO wire lay flat on a flexible substrate and was fixed to electrodes at both ends (Figure 5.4). Bending the substrate, and therefore, stretching the wire, a tensile strain was induced in the wire, which led to a piezoelectric potential drop along the wire. The piezoelectric potential drove electrons through an external circuit to charge the wire. Releasing the substrate, electrons were forced to flow back in the opposite direction. Yang et al. could measure alternating output voltage of up to U=50 mV and a current of up to I=800 pA by repeated stretching and releasing of a single wire (AC nanogenerator) with a strain of S=0.05-0.1%.

The mechanism for the generation of piezoelectric current proposed by Yang et al. is shown in Figure 5.5. Tensile strain induces ionic charges in the ZnO nanowire due to the piezoelectric effect. The induced ionic charges are non-mobile and remain in the nanowire for an extended period of time without depletion by free carriers as long as the strain is preserved. The ZnO nanowire makes a Schottky contact with a metal electrode on the left and an ohmic contact with an electrode on the right. For the case of positive piezoelectric potential V^+ at the Schottky barrier side and negative one V^- at the ohmic side, the conduction band C_B and Fermi level E_F on the right side is raised by $\Delta E_p = e(V^+ - V^-)$ (Figure 5.5b). Thus electrons flow from the right to the left electrode through an external load resistor. Because of the high resistance of the Schottky barrier (for voltages below a threshold value) electrons can not flow through the nanowire. The electrons accumulate at the interfacial region between the left electrode and the nanowire. This process continues until the potential created by the accumulated electrons balances the induced piezoelectric potential and the Fermi levels of the electrodes reach a new equilibrium value (Figure 5.5c).

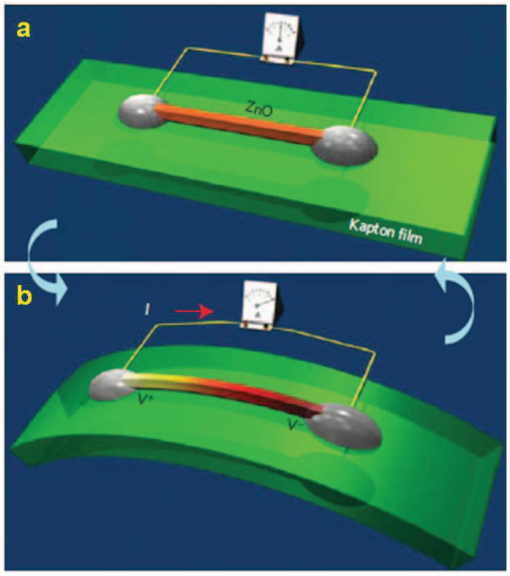

Figure 5.4: Design of a single ZnO wire nanogenerator on a flexible substrate. (a) The ZnO nanowire lies on a polymer (Kapton) substrate, with both ends tightly bonded to the substrate and outlet interconnects. (b) Mechanical bending of the substrate creates tensile strain in the ZnO wire. The corresponding induced piezoelectric potential drives electrons through the external load [RY09c].

Releasing the tensile strain in the nanowire results in the disappearance of the piezoelectric potential and then the Fermi level on the right side lowers by $\Delta E_p = e(V^+ - V^-)$ (Figure 5.5d). The electrons accumulated near the left electrode flow back through the external circuit to the right electrode and the system returns to its original state. Figure 5.5e shows the corresponding peaks in the electrical output by stretching and releasing the nanowire. For the case of negative piezoelectric potential V^- at the Schottky barrier side and positive one V^+ at the ohmic side (as a result of switching the c-axis orientation of the ZnO nanowire), the conduction band C_B and Fermi level E_F on the left side is raised by $\Delta E_p = e(V^+ - V^-)$ (Figure 5.5f). Thus electrons flow from the left to the right electrode through the external load resistor. In this case the free electrons can enter the nanowire and screen the induced piezoelectric charges. Because the piezoelectric charges are ionic charges and can not move, the free electrons can not completely neutralize them and thus the local effective potentials reduce from V^- and V^+ to V_1^- and V_1^+ on the left and right side, respectively (see Figure 5.5g). This process continues until the electric potential created by free moving electrons balances the induced piezoelectric potential and

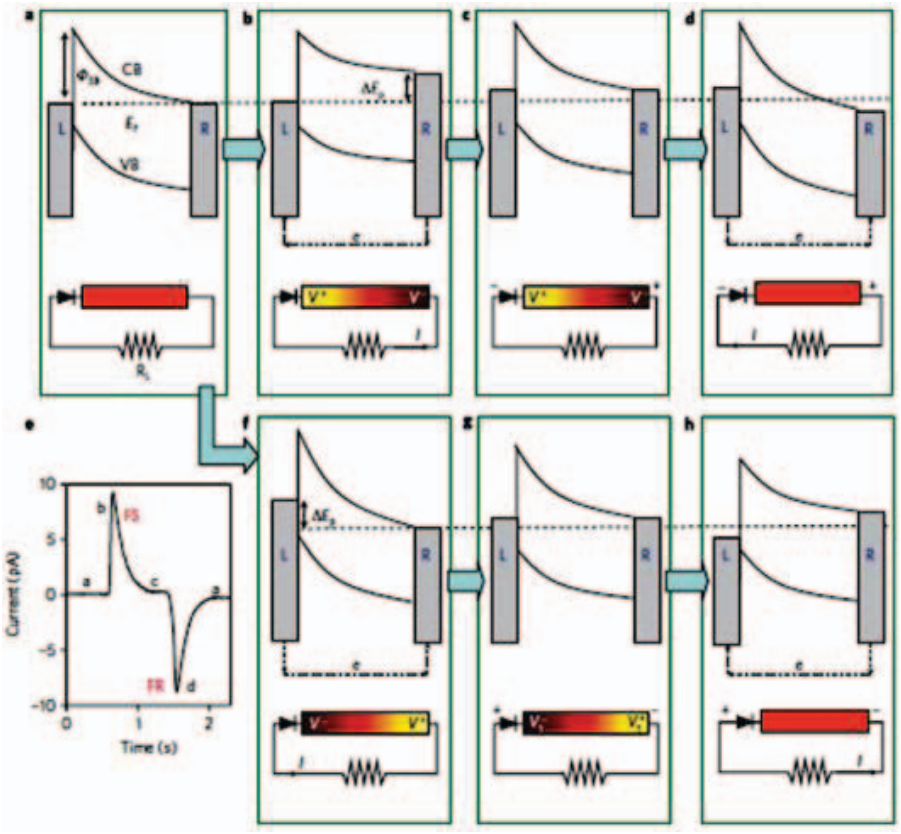

Figure 5.5: Proposed mechanism for the generation of piezoelectric current in a bent ZnO wire generator.(a) Energy band diagram of a piezoelectric ZnO wire making a Schottky contact with a metal electrode on the left and an ohmic contact with an electrode on the right. The dotted line is the Fermi level E_F of the electrodes and ϕ_{SB} is the height of the Schottky barrier. C_B and V_B are the conduction and valence bands of ZnO, respectively. A realistic measurement circuit containing a load resistor R_L, which is much smaller than the resistance of the Schottky barrier and the ZnO wire, is also shown. (b)-(d), Induced piezoelectric potential is positive at the Schottky barrier side V^+, and negative at the ohmic contact side V^-. (b) when the ZnO wire is tensile stretched, the Fermi levels shift relative to each other generating a positive voltage/current peak as a result of electrons flowing from the right electrode to the left electrode, and they re-reach equilibrium in (c), and they shift reversely again when the ZnO wire is released in (d), generating a negative voltage/current peak as the electrons flow back (from the left electrode to the right electrode). (e) Experimentally measured output current showing the four different stages described above. (f)-(h) When the induced piezoelectric potential is negative at the Schottky barrier side V^-, and positive at the ohmic contact side V^+, the Fermi levels shift in a different way during the stretch-release cycle [RY09c].

the Fermi levels at the two electrodes reach a new equilibrium value. Releasing the tensil strain in the nanowire results in the disappearance of the piezoelectric potential and the free charges that used to screen the piezoelectric charges are now free to move. Because the Fermi level of the right side is higher, the free electrons flow back from the right to the left electrode through the external circuit (Figure 5.5h). This process continues until the Fermi levels of the two sides reach their original equilibrium again. In this mechanism the nanowire acts like a capacitor and charge pump, storing electrons and then driving them back and forth through the external circuit when the ZnO nanowire is stretched and released. The Schottky barrier acts as a gate that prevents the flow of the electrons through the ZnO nanowire. In addition, this leads to the accumulation of electrons, which results in a higher discharge rate. The Schottky barrier can either be at just one side of the nanowire or at both sides [RY09c].

Recently Zhu et al. [GZ10] have developed a ZnO nanowire generator on the basis of the harvesting mechanism proposed above. The used technique consisted of two main steps. In the first step, the vertically aligned ZnO nanowires grown on a Si substrate were transferred to a receiving flexible substrate (kapton-film) to form horizontally aligned arrays of ZnO nanowires. Then, using the photolithography technique rows of stripe-shaped Au electrodes were deposited on top of the horizontal nanowire arrays to connect all of the nanowires together. An as-fabricated nanogenerator structure could generate a short-circuit current of up to I_{sc}=107 nA and an open-circuit voltage of up to U_{oc}=2.03 V at a strain of S=0.1%

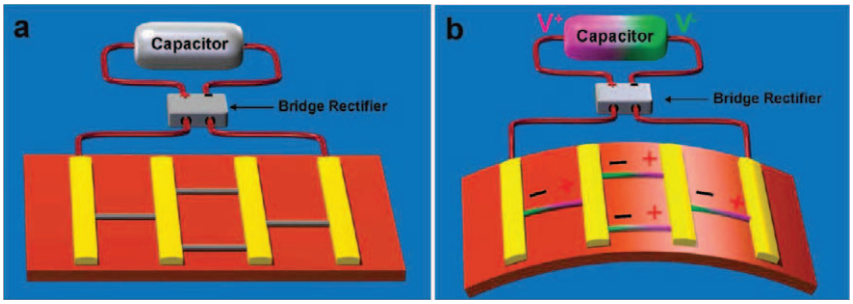

Figure 5.6: (a) Schematic diagram of horizontally aligned ZnO nanowire generator without mechanical deformation. Using photolithography technique 300 nm thick rows of stripe-shaped Au electrodes with 10 µm spacing were deposited on top of the horizontal nanowire arrays. (b) Demonstration of the output scaling-up under mechanical deformation. The "±"signs indicate the polarity of the local piezoelectric potential induced in the nanowires. For a successful and effective energy storage in the capacitor, the alternating output of the nanogenerator was rectified using a full wave rectifying bridge [GZ10].

with a deformation frequency of ν=0.33 Hz. By rectifying and storing the generated electric energy in capacitors, a commercial light-emitting diode (LED) was successfully lighted up. The schematic diagrams in Figure 5.6 show the working principle of this nanogenerator. The nanowires connected in parallel contribute collectively to the current output and those connected in different rows in serial improve constructively the voltage output. Another similar disign of the nanogenerator composed of horizontally aligned ZnO nanowires but with more complexe stripe-shaped electrodes has been reported by Xu et al. [SX10]. The nanogenerator could achieve a maximum open-circuit output voltage of U_{oc}=1.26 V and a short-circuit current of I_{sc}=28.8 nA in response to a low-frequency mechanical strain of S=0.19% at a straining rate of $2.13\%s^{-1}$.

Lately a nanocomposite generator composed of conical shaped ZnO nanowires dispersed onto a flat polymer film of polymethyl-methacrylate (PMMA) has been reported by Hu et al. [YH10] (Figure 5.7b). The used technique for fabrication consisted of three main steps: In the first step, the vertically aligned ZnO nanowires grown on a GaN film were transferred to a receiving kapton-film. The kapton substrate was coated first with a Cr/Au (50 nm/50 nm) metal film and then with a PMMA layer (2 µm), before distribution of the nanowires on it. In the second step, the distributed conical nanowires with their random lateral orientation on the substrate were spin coated with a 100 nm PMMA layer. These distribution and coating processes were carried out alternately for five cycles to form a composite structure as shown in Figure 5.7c. In the last step, first another PMMA layer (2 µm) and then a Cr/Au (50 nm/50 nm) metal film as an electrode were deposited on the nanocomposite. The size of the whole device was about 1.5×2 cm^2. This nanogenerator could produce an output voltage up to U=2 V (equivalent open circuit voltage of U_{oc}=3.3 V) and a current of I=50 nA under a compressive strain of S=0.11% at a straining rate of $3.67\%s^{-1}$. The output power of the nanogenerator was sufficient to drive a LCD (liquidt-crystal diode) screen with the same size of the lighting area.

The working principle of the nanogenerator was suggested to be a result of the unipolar assembly of the conical nanowires. Because of the conical shape of the nanowires (Figure 5.7a) the projected components of all of them added along the vertical direction constructively up, as shown in Figure 5.7c. This could be the source of pizoelectric polarization across the thickness of the composite structure for creating the piezopotential. Figure 5.8 shows the calculated piezopotential induced across the top and bottom electrodes when the nanogenerator was deformed under a compressive stress. For a pair of compressed conical nanowires (Figure 5.8a) the local potential distribution along the nanowires indicated an

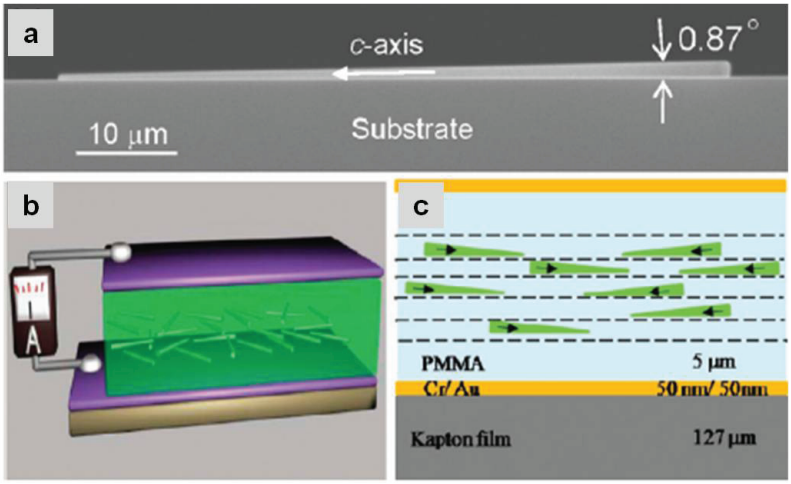

Figure 5.7: (a) Cross-section view SEM image of a conical nanowire (with the conical angle of φ=0.87°) laying on a flat substrate. The c axis of the nanowire was pointing downward into the substrate. (b) Schematic image of the nanocomposite generator consisting of conical nanowires in a PMMA layer. (c) Schematic diagram showing the design and the working principle of the nanocomposite generator. Each dashed line indicates one cycle of deposition-coating of the nanowires. The conical shape nanowires and their corresponding c axes are represented by arrowheads [YH10].

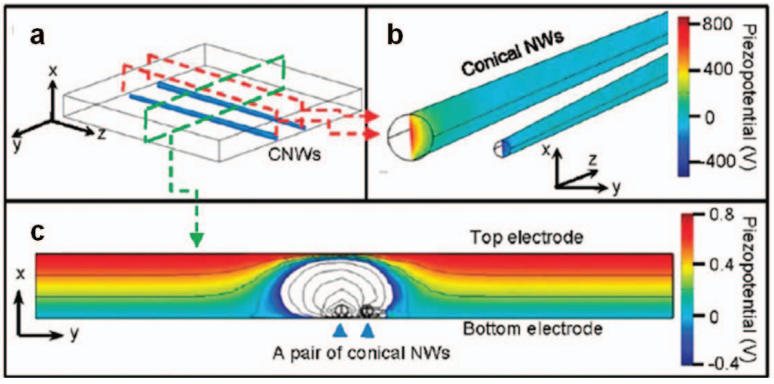

Figure 5.8: (a) The unit cell and model used for calculating the potential distribution across the top and bottom electrodes of the nanogenerator with the presence of a pair of conical nanowires. The conical nanowires (CNWs) were under compressive strain during the deformation of the nanogenerator under a compresive stress. The corresponding cross sections at which the potential distributions were exhibited are indicated by dashed lines, and the results are shown in (b,c), respectively. (b) The local potential distribution in compressed conical nanowires. In (c) the blank region close to the conical nanowires was the region where the calculated piezopotential was smaller than U=-0.4 V, beyond the range selected for the color plotting. Equal potential lines were used to present the detail in this region [YH10].

induced negative potential at the head of the conical nanowires and a positive one at their bottoms (Figure 5.8b). As well, the potential distribution across the nanowires indicated an induced negative potential close to the conical nanowires and a positive one at the top electrode, as shown in Figure 5.8c. The induced electric potential difference across the two electrodes was the driving force for the flow of electrons in the external load. By releasing the applied stress, and therefore, releasing the strain in the conical nanowires the inductive charges in the electrodes had to flow back. This process produced an AC output current [YH10].

The uniaxial stressed ZnO nanowires: The latest concept of a ZnO nanowire generator has been reported by Xu et al. [SX10] in 2010, in which uniaxial stress was applied to vertically aligned ZnO nanowires to induce a piezoelectric potential along the nanowires. Figure 5.9c-d show schematically the design and working principle of the nanogenerator reported by Xu et al. The nanogenerator consisted of vertically aligned ZnO nanowires grown on a 50 nm Au-coated silicon substrate (Figure 5.9a). A 20 nm thick film of titanium was used between the substrate and the gold film as an adhesion layer to buffer the large lattice mismatch between the Si (100) surface with native oxide and Au (111) surface to improve interfacial bonding. A layer of polymethyl-methacrylate (PMMA) was spin-coated onto the nanowires to improve the stability and mechanical robustness of the entire structure. This also prevented possible short-circuiting between the bottom and top electrodes. After oxygen plasma etching the clean tips of the nanowires were availabe to contact with the top electrode (Figure 5.9b). A 300 nm platinum-coated silicon wafer was used as the top electrode, creating a Schottky contact at the interface. Using a linear motor stimulator to generate the mechanical strain at an impact speed of 0.1 ms^{-1} a maximum open-circuit voltage of U_{oc}=96 mV and short-circuit current density of I_{sc}/A=8.9 nA cm^{-2} could be achieved. Connecting three as-fabricated nanogenerators in series, showed a linear increase of output voltage and in parallel, a linear superposition of output current density.

The working principle of the nanogenerator proposed by Xu et al. [SX10] is as follows: Uniaxial strain in a ZnO nanowire separates the static ionic charge centers in the tetrahedrally coordinated ZnO units (see Figure 2.5a in section 2.2 too). Thus a piezoelectric potential gradient appears along the c-axis of the nanowire. Because the c-axes of the nanowires are aligned parallel to each other, the piezoelectric potentials in nanowires have the same tendency of distribution, which results in an enhanced macroscopic behaviour.

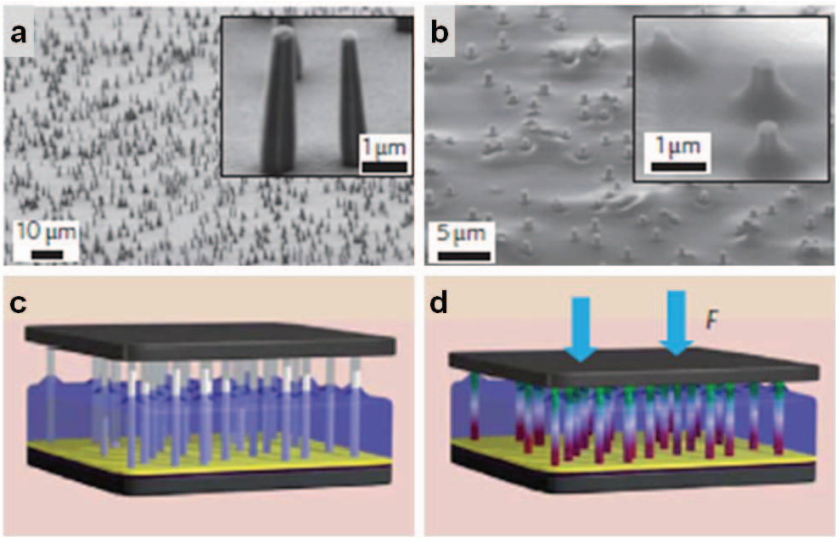

Figure 5.9: (a) SEM image of grown ZnO nanowires on an Au-coated silicon substrate. (b) SEM image of the nanowires after spin-coating with polymethyl-methacrylate (PMMA) and then oxygen plasma etching. (c) Design of a nanogenerator of as-prepared ZnO nanowires. The Pt-coated silicon electrode placed on top of the nanowires forms a Schottky contact at the interface. (d) Mechanical normal stress applied on the top electrode creates uniaxial strain in crystallographically aligned ZnO nanowires and results in a macroscopic piezoelectric potential along the growth direction (c-axis) of the nanowires [SX10].

The working mechanism for the present nanogenerator is similar to the proposed mechanism for the bent horizontally aligned ZnO nanowire arrays as shown in Figures 5.5a and 5.5f-h, in which L represents the Schottky top contact and R shows the ohmic bottom contact. A compressive stress applied on the top electrode (see Figure 5.9d) results in uniaxial compression in the nanowires. Thus a negative piezoelectric potential at the top Schottky contact side and a positive piezoelectric potential at the bottom ohmic contact side are created. The negative piezoelectric potential rises up the conduction band and the Fermi level at the top relative to the bottom electrode. Therefore, electrons flow from the top to the bottom through the external circuit. These electrons accumulate around the bottom of the nanowires. This process continues until the piezoelectric potential is fully screened and the Fermi levels of both sides reach a new equilibrium. When the compressive strain is released, the piezoelectric potential inside the nanowires diminishes and the electrons accumulated at the bottom flow back via the external circuit (if leakage is negligible). The Schottky barrier prevents the flow of mobile charges through the nanowire-metal contact

interface. For the operation of the nanogenerator presence of a Schottky contact at least at one end of the nanowires was essential. A nanogenerator with ohmic contacts at both ends gave no output signal.

Recently Momeni et al. [KM10] have developed an analytical model that predicts the electric potential generated by a nanocomposite electrical generator composed of vertically aligned ZnO nanowires embedded in a finite epoxy matrix (Figure 5.10). Using continuum mechanics and the perturbation technique introduced by Wang and Gao [YG07] (refer to subsection 4.3.1 too) the piezoelectric response of a single ZnO nanowire embedded in an epoxy matrix (Figure 5.11a) was predicted. Solving the governing differential equations using a finite difference method resulted in an electric potential gradient aligned along the c-axis of the nanowire. As shown in Figure 5.11c positive and negative potentials were located at the ends of the nanowire and separated by a zero-valued electric potential at the middle. It was also shown that the electric potential is a strong function of shear stress at the interface of matrix and nanowire. The calculated distribution of axial and shear stresses along the ZnO nanowire indicated that axial stress is maximal in the middle of the nanowire and shear stress is highest at the ends of the nanowire. Thus the distribution of electric potential was attributed to shear stress transfer at the interface of nanowire and the surrounding polymer matrix.

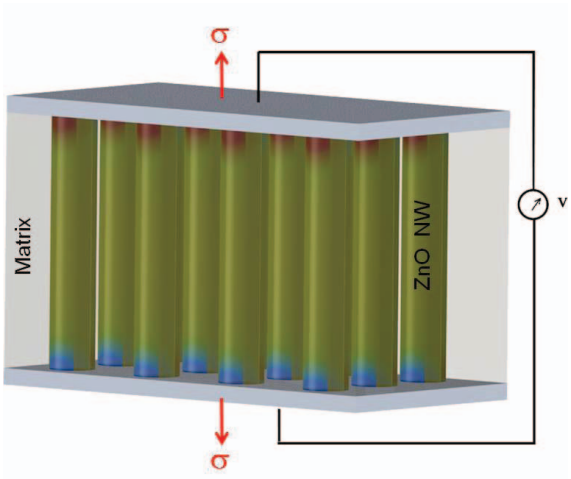

Figure 5.10: Schematic picture of the proposed nanocomposite generator system composed of vertically aligned ZnO nanowires, which are embedded in an epoxy matrix. Under an uniaxial stress on the electrodes positive and negative electric potentials are induced at the ends of the nanowires [KM10].

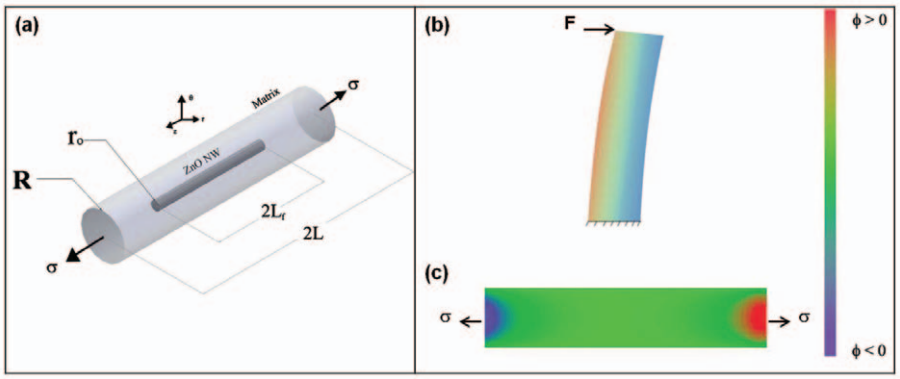

Figure 5.11: (a) representative volume element of a ZnO nanowire with length of $2L_r$ embedded in an epoxy matrix with length of 2L. The composite is subjected to the overall stress of σ along the cylindrical axis. R and r_0 are the outer radius of the element and the radius of the ZnO nanowire, respectively. (b) Schematic of induced electric potential distribution for a deflected ZnO nanowire along its diameter and (c) for a nanowire embedded in an epoxy matrix as shown in (a) along its growth axis (c-axis) [KM10].

Figures 5.11b and c shows schematically the electric potential distribiutions calculated in a deflected ZnO nanowire and in a nanowire embedded in an epoxy matrix. Because of the electric potential gradient the electric field inside the nanowire embedded in the matrix is lower than that inside the deflected nanowire. Therefore, the nanocomposite electrical generator is a more sustainable energy source relative to typical nanogenerators using deflected ZnO nanowires. For a nanowire with diameter of D=50 nm and length of L=600 nm under maximum applied stress σ_{max} = 200 MPa, the maximum generated electric potential was calculted to be more than U=0.8 V [KM10]. This is 260% of the value (U=0.3 V) reported for the deflected ZnO nanowires [YG09].

As shown in Figures 5.9c-d, the uniaxial nanogenerator reported by Xu et al. can be considered also as a nanocomposite electrical generator composed of ZnO nanowires embedded in a matrix of PMMA. The experimental results of this nanogenerator are in agreement with the analytical model proposed by Momeni et al. This suggests that the PMMA layer used in the nanogenerator structure exerted shear stresses on the embedded nanowires as an uniaxial stress was applied on the top electrode. This explains why no response signal could be measured by the uniaxial nanogenerator without the PMMA matrix. Thus it seems that the working mechanism proposed by Momeni et al. is more appropriate than that one proposed by Xu et al.

In sections 5.2 and 5.3 a new approach for the uniaxial nanogenerator without any

epoxy matrix will be reported, but in which shear stress at the interface of nanowires may nevertheless contribute to the induced piezoelectric potential.

5.1.2 Fabrication and characterization methods

Fabrication: Most of the reported ZnO nanowires generators (∼75%) were composed of nanowires, which were synthesized by the vapor-liquid-solid (VLS) method [YG09, YH10, JL08a, JL08b, ZLW06, GZ10, XW07a, XW07b, RY09b]. As explained in section 3.1, due to its high synthesis temperature (above T=1000 ℃), the growth process by the VLS method is limited to certain substrates, which have a high melt temperature above the synthesis temperature. Moreover, the synthesis of vertically aligned ZnO nanowires required the use of GaN or sapphire (Al_2O_3) substrates because of the small lattice mismatch between the substrates and ZnO. Therefore, the fabrication of these nanogenerators is associated with high energy consumption and expensive substrates. For the nanogenerators, in which the synthesized nanowires should be transferred onto another receiving flexible substrate to form horizontally aligned arrays, the fabrication process had more steps. For these cases, the nanowires were deposited directly onto the receiving substrate by dry physical contact using the sweeping-printing-method [GZ10] (refer to the fabricated structure shown in Figure 5.6) or in a nanowire solution which was dispersed onto the receiving substrate. In the latter case the nanowires together with the substrate were soaked with ethanol. Then the nanowires were effectively chopped off the substrate by applying an ultrasonic wave, forming a freely suspended nanowire solution. The nanowire could be transferred by dispersing a droplet of the nanowire solution onto the receiving substrate [YH10] (refer to the fabricated structure shown in Figure 5.7b-c). In contrast to the VLS method, the wet chemical method (refer to section 3.3) allows a simple and cost-efficient fabrication process of the nanogenerators, in which vertically aligned ZnO nanowires are synthesized at temperatures below T=100 ℃ on a silicon wafer [SX10] (see Figure 5.9) or even on flexible polymer substrates [CLH12] (see Figure 5.3c) and textile fibers [YQ08] (see Figure 5.3e).

In general, the ZnO nanowires synthesized by the VLS method at high temperatutes show a better crystal quality with less defects compared to the ones synthesized by the wet chemical method at low temperatures. This can result in the generation of higher piezoelectric potential in deformed nanowires synthesized by the VLS method [Mr10]. However, the advantages of the wet chemical method make this as a competitive method

to the other ones.

Not only the crystal quality, but also the density, effective length, and diameter (aspect ratio) of the nanowires affect the piezoelectric behavior. Riaz et al. [Mr10] observed that the performance of the nanogenerators was not dependent on the substrates. In addition, finite element simulations for deflected nanowires with a Pt-coated AFM tip indicated that the output voltage of the nanogenerator increased as the aspect ratio was increased and started to decrease above an aspect ratio of 80 for ZnO nanowires. Moreover, the output voltage from a single ZnO nanowire could be maximized by increasing the contact area along the length of the nanowire. Riaz et al. concluded that to achieve a larger magnitude of the output voltage signals from a ZnO nanogenerator, the density of the nanowires on the substrate, length, and diameter of the nanowires should all be in the range of $10^6 - 10^7$ cm^{-2}, L=1-4 µm, and D=50-200 nm, respectively.

Characterization: A piezoelectric material is modeled as a charge generator in parallel with an intrinsic capacitance and an intrinsic resistance as shown in Figure 5.12. To transform the piezoelectrically generated charge into a voltage signal, a load resistor R_L can be connected between the top and bottom electrodes, allowing free charges existing within the metal electrodes to flow and redistribute to balance the induced piezoelectric potential. C_L represents the equivalent capacitance of the external circuit, which is the sum of the capacitances of the cables and other external connecting devices that carry the signal to the load resistance [MA08, YH11].

The output signal of a nanogenerator may be affected by the measurement system and change in capacitance of the nanogenerator during mechanical deformation. In general, an

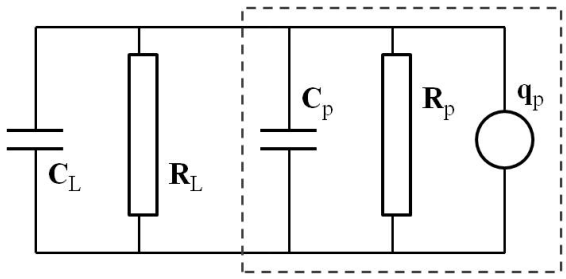

Figure 5.12: The equivalent circuit of a piezoelectric generator including a charge generator q_p, parallel to a resistor R_p and a capacitor C_p. The piezoelectric generator is connected to a load resistor R_L. Here C_L is the equivalent capacitance of the external circuit.

electrical measurement system has a feed in bias current in an order of picoamperes that may charge up the capacitor made of the two electrodes on the top and bottom surfaces. Thus a variation in capacitance due to deformation of the entire structure may induce an output signal [YH10]. The switching-polarity test can differentiate a true output signal generated by the nanogenerator, due to the piezoelectric effect, from a false signal from the measurement system [SX10, YH10, RY09c, RY09b]: For example, when a current meter in the forward connection to a ZnO nanogenerator, measures a positive output pulse (current/voltage) during stretching and a corresponding negative pulse during releasing the ZnO nanowires, the current meter in the reverse connection must measure also the reversed output pulses.

In the literature, usually, the short-circuit current (I_{sc}) and open-circuit voltage (U_{oc}) were measured to characterize the performance of a nanogenerator. In all reported ZnO nanogenerators, current-voltage curves were also measured to determine the Schottky nature of metal-ZnO interfaces.

It is worth remembering that for all so far realized ZnO nanowire generators (except one case [RY09b, RY09a]), using Au/Pt electrodes at least at one metal-ZnO contact creating an asymmetric Schottky barrier is an essential requirement for the function of these devices. It has been assumed that the Schottky contact at the interface between the electrode and the nanowires gates and directs the flow of electrons under the driving of the piezoelectric potential and prevents the flow of electrons through the nanowire itself. Even in the exceptional case of the single-wire generator reported by Yang et al. [RY09b, RY09a], in which silver paste was used for the metal-ZnO contact, the nonlinear Schottky-like transport behavior was a necessity for a working nanogenerator.

In the next two sections, the generation of piezoelectric potential in uniaxial stressed ZnO nanowires using Ag electrodes is reported. It will be shown that by manipulating the growth process of ZnO nanowires and controlling the electrical properties of the ZnO seed layers, one can control the behavior of the metal-semiconductor contacts (Ag-ZnO) and even change an ohmic-like contact to a Schottky-like one. In addition, it will be indicated that the Schottky contact is not a necessity for the operation of a ZnO nanogenerator, as believed by now.

5.2 Advancement of the wet chemical method for ZnO nanogenerators

The wet chemical method and the influence of the growth parameters on size, density, diameter distribution, and orientation of growing ZnO nanowires was discussed in section 3.3. For using the synthesized ZnO nanowires as nanogenerators, the quality of the electric contact between the upper electrode and the synthesized ZnO surface is an important factor. For the wet chemical method, there are two possible processes that lead to worse contacts: the formation of ZnO clusters on top of the grown nanowire film, and a broad length distribution of grown nanowires. In this section, the synthesis of well-flat films of ZnO nanowires by an advanced wet chemical method is reported. Flat seed layers, which are synthesized wet chemically themselves, lead to the growth of flatter films of ZnO nanowires in the next step and consequently, to better electric contacts with the metal electrodes.

At first the glass substrates were cleaned with acetone, isopropyl and distilled water in an ultrasonic cleaner for t=10 min, and then dried under a flow of nitrogen. Before sputtering, the substrates were baked at T=95 ℃ in a conventional furnace for t=30 min and then coated with d=70 nm Ag as the bottom electrode for the later nanogenerators. Three types of ZnO seed layers denoted A, B, and C in the following were synthesized by putting the substrates top up in the ZnO nanoparticle solution of 0.01 M zinc acetate dihydrate [$Zn(CH_3COO)_2.2H_2O$] and lithium hydroxide monohydrate [$LiOH.H_2O$] in ethanol. Their growth parameters are given in Table 5.1. The thickness of the as synthesized seed layers was approximately 80 nm. Figure 5.13 shows SEM images of the synthesized ZnO seed layers. After cleaning the seed layered substrates with distilled water and drying under a flow of gaseous nitrogen, the ZnO nanowires were grown by the wet chemical method putting the substrates top up in an aqueous solution of 0.1 M zinc nitrate hexahydrate [$Zn(NO_3)_2.6H_2O$] and hexamethylenetetramine ($C_6H_{12}N_4$) in the furnace. Four types of ZnO nanowires denoted A1, B1, C1 and C2 in the following were grown with the parameters given in Table 5.2. Figure 5.14, 5.15, 5.16, and 5.17 show the SEM images of grown nanowires type A1, B1, C1, and C2, respectively. After the growth processes, the substrates were cleaned and dried again.

Figure 5.19 shows the influence of the cleaning process on the synthesized ZnO film surface. For most of the samples, it was observed that a cleaning in the ultrasonic cleaner longer than t=45 min resulted in an appearence of holes on the ZnO films, which can

Table 5.1: Growth parameters of the synthesized ZnO seed layers.

ZnO seedlayer	Dilution of nanoparticle solution	T (°C)	t (h)
A	1 : 1	80	2
B	1 : 6	80	2
C	1 : 1	90	2

Table 5.2: Growth parameters of the synthesized ZnO nanowires.

ZnO nanowire	ZnO seed layer	T (°C)	t (h)
A1	A	80	6
B1	B	90	6
C1	C	90	6
C2	C	90	2

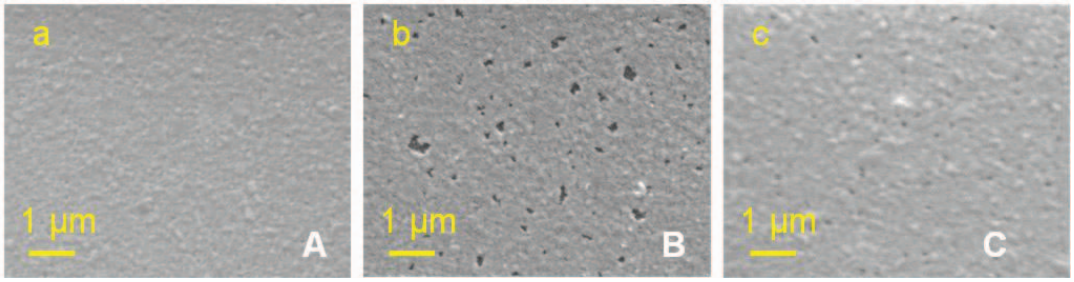

Figure 5.13: SEM images of synthesized ZnO seed layers by the wet chemical method in 0.01 M ZnO nanoparticle solution. (a,b) Seed layer of type A synthesized at T=80 °C for t=2 h. (c,d) Seed layer of type B synthesized in 1 : 6 dilution of the nanoparticle solution at T=80 °C for t=2 h. (e,f) Seed layer of type C synthesized at T=90 °C for t=2 h.

negatively affect the electric contact between the ZnO surface and the top electrode for nanogenerator applications. A comparison between the cleaned ZnO films synthesized by the above described advanced wet chemical method and those synthesized by the standard wet chemical method (see Figure 3.18 in section 3.3) indicates the advantage of the advanced method for production of a flat film of ZnO nanowires.

The cross-sectional SEM images of nanowires grown for t=6 h (see Figures 5.14b, 5.15b, and 5.16b) show that the synthesized ZnO films consist of three layers of nanowires, at least. The thickness of the ZnO films for the sample A1, B1 and C1 were measured to be about d=1.12 µm, d=1.85 µm and d=2.46 µm using a profilometer. As shown in the SEM images (Figures 5.14 b and 5.15 b), the nanowires in the upper layer of the ZnO film grown

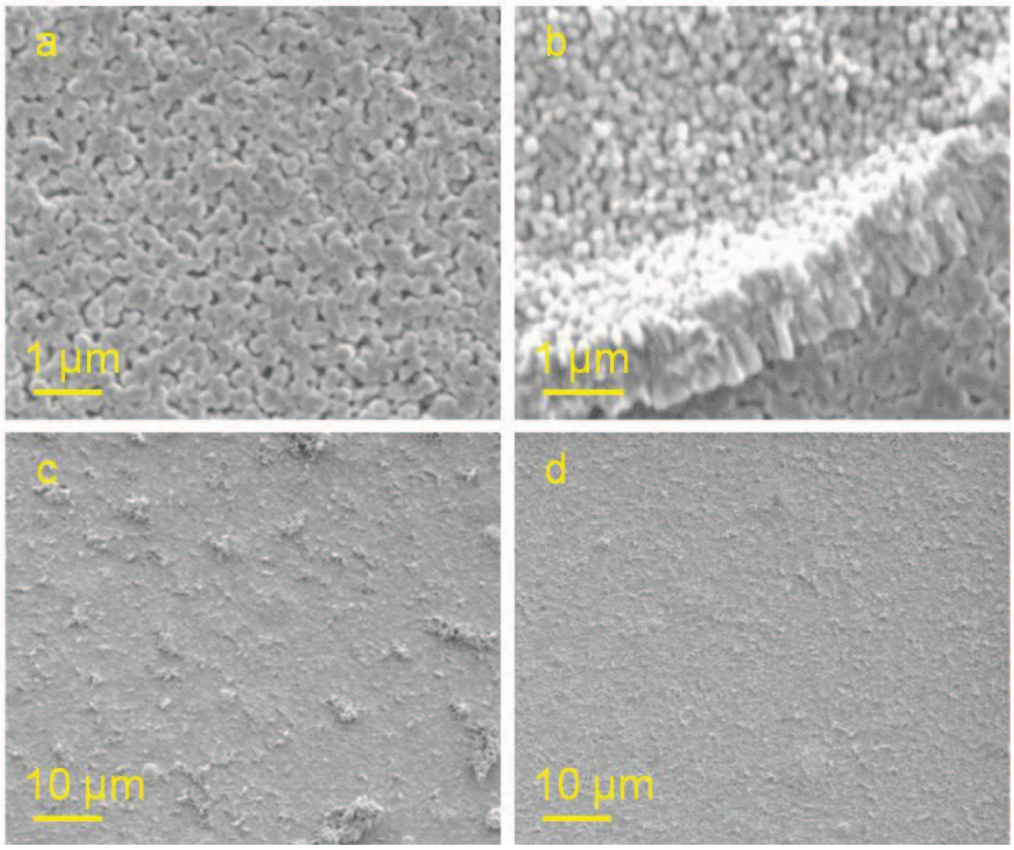

Figure 5.14: SEM images of ZnO nanowires type A1 grown wet chemically on a seed layer of type A in 0.1 M zinc solution at T=80 ℃ for t=6 h. (a) and (b) show top and cross-sectional views of grown nanowires, respectively. (c) and (d) show the ZnO film surface before and after the cleaning process, respectively.

at T=90℃ (sample B1) are nearly 2 times longer than those grown at T=80℃ (sample A1). Although the synthesized nanowires in the middle layer of the ZnO film are about 130 nm thick for both samples, those in the upper layer of the ZnO film have different sizes. These are about 260 nm thick in sample A1 and 100-330 nm thick in sample B1. Actually, using the wet chemical method a higher synthesis temperature results in longer nanowires and a wider diameter distribution. The influence of the seed layer on the growth morphology of nanowires can be seen from the SEM images of sample B1 and C1 (Figures 5.15 b and 5.16 b). The nanowires were grown at the same temperature (T=90℃) on the seed layers of type B and C with the (approximately) same thickness of d=80 nm.

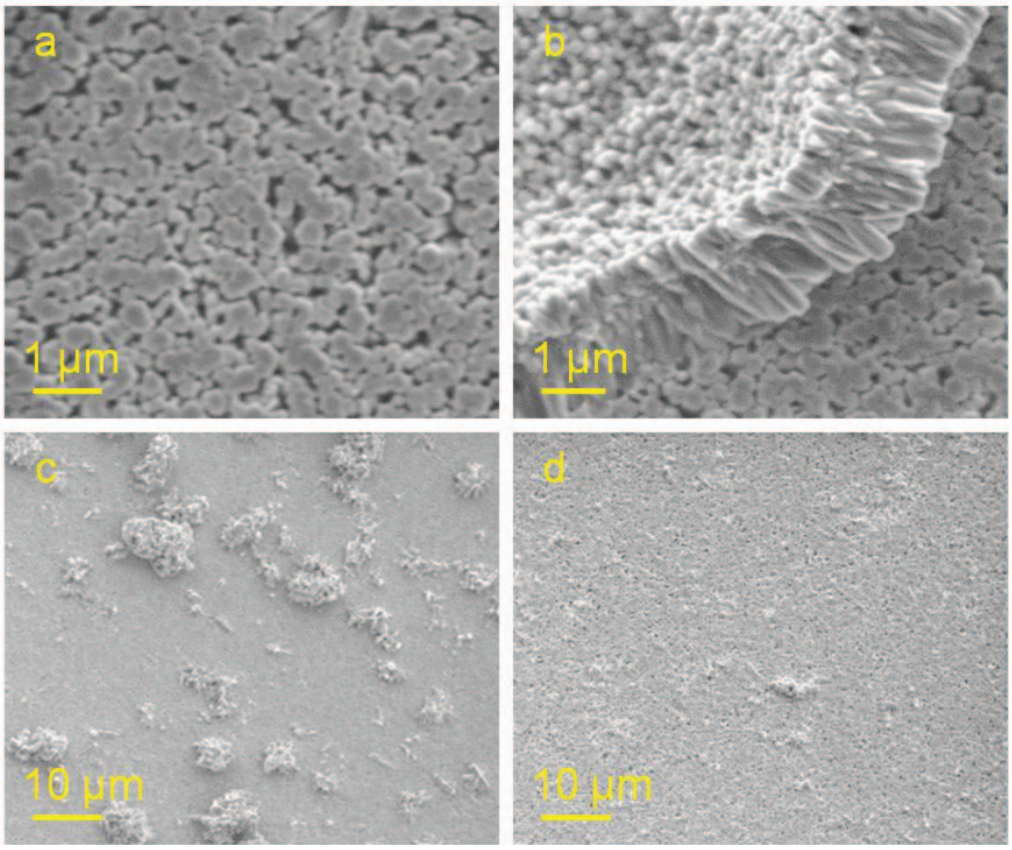

Figure 5.15: SEM images of ZnO nanowires type B1 grown wet chemically on a seed layer of type B in 0.1 M zinc solution at T=90 ℃ for t=6 h. (a) and (b) show top and cross-sectional views of grown nanowires, respectively. (c) and (d) show the ZnO film surface before and after the cleaning process, respectively.

However, the final ZnO film in the sample C1 is thicker than that in the sample B1. As shown in Figures 5.15 b and 5.16 b, the nanowires in the upper layer of the ZnO film grown on the seed layer of type A are a little longer (1.8 µm) than those grown on the seed layer of type B (1.36 µm). Moreover, those in sample C1 are averagely thicker (with a diameter distribution of 220-540 nm) than those in sample B1.

From Figure 5.17a (inset), for the ZnO structure grown for t=2 h and the previous systematic studies for the wet chemical method (refer to section 3.3), it seems that in the first 2 hours of the growth process, effectively no oriented nanowires can be synthesized under these growth conditions. Thus the grown nanostructures of type C2 should be

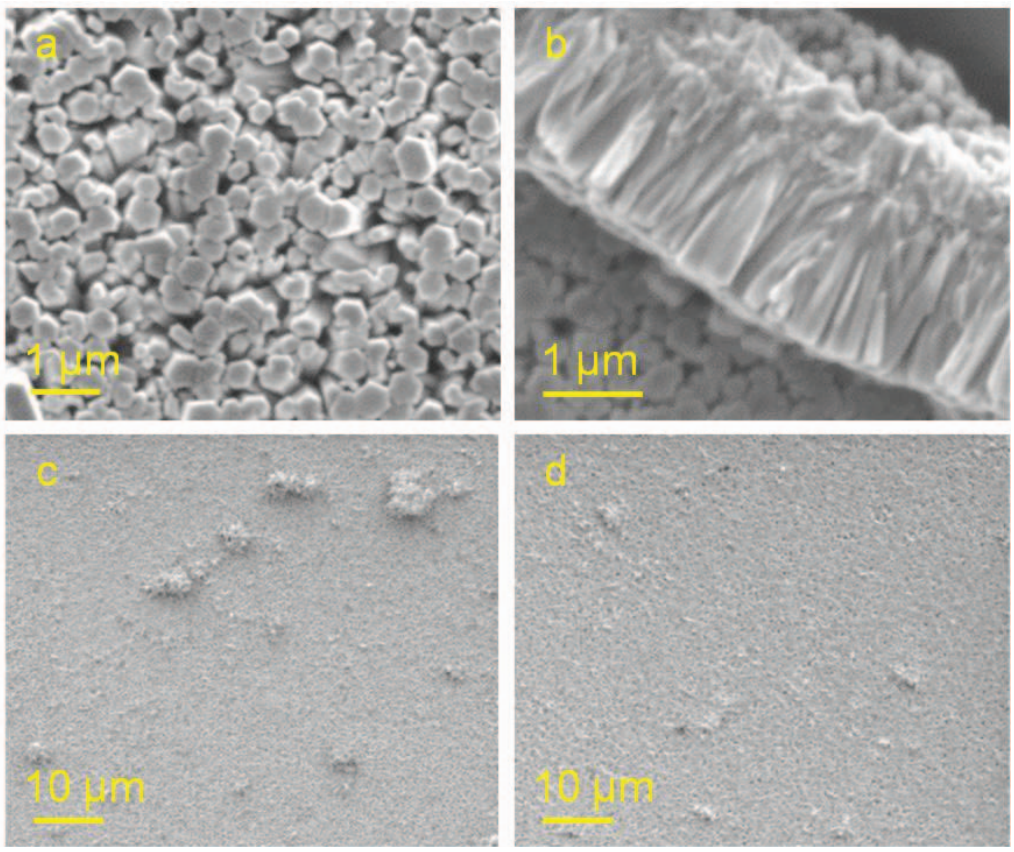

Figure 5.16: SEM images of ZnO nanowires type C1 grown wet chemically on a seed layer of type C in 0.1 M zinc solution at T=90 ℃ for t=6 h. (a) and (b) show top and cross-sectional views of grown nanowires, respectively. (c) and (d) show the ZnO film surface before and after the cleaning process, respectively.

effectively an amorphous ZnO-film. This can be well confirmed by the X-ray diffraction pattern of the sample, as shown in Figure 5.18a. The XRD patterns of the synthesized ZnO seed layers of all three types A, B, and C do not show any ZnO crystal peaks, and therefore, are amorphous thin films (Figure 5.18a). The peak at about 38.3° originates from the Ag-film sputtered on the substrates. As shown in Figure 5.18b, the XRD patterns of the grown nanowires of type A1, B1 and C1 present a strong peak at 34.41° for the ZnO (002) surface. This reveals that the synthesized nanowires are crystallized in the hexagonal structure of ZnO and, especially for the sample C1, are well vertically aligned along the preferential growth direction (c-axis) of ZnO.

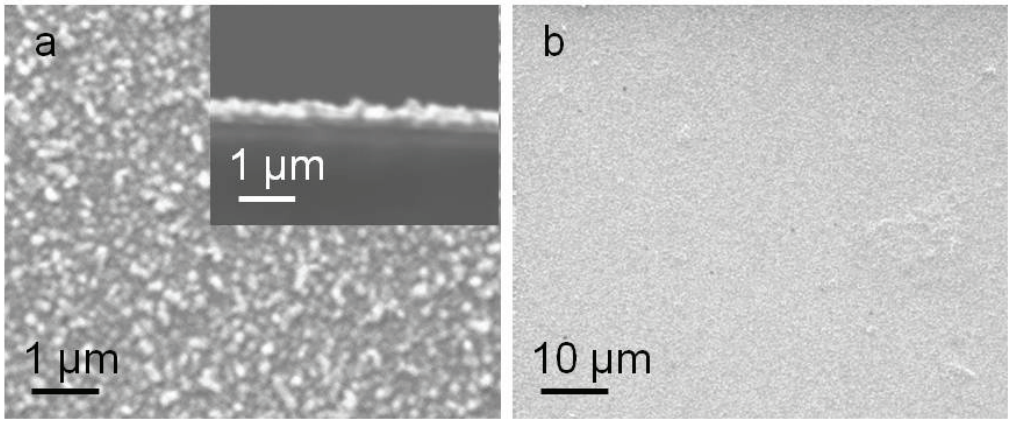

Figure 5.17: Top view SEM images of ZnO nanowires type C2 grown wet chemically on a seed layer of type C in 0.1 M zinc solution at T=90 ℃ for t=2 h. The inset in (a) shows the cross-sectional view of the grown ZnO film.

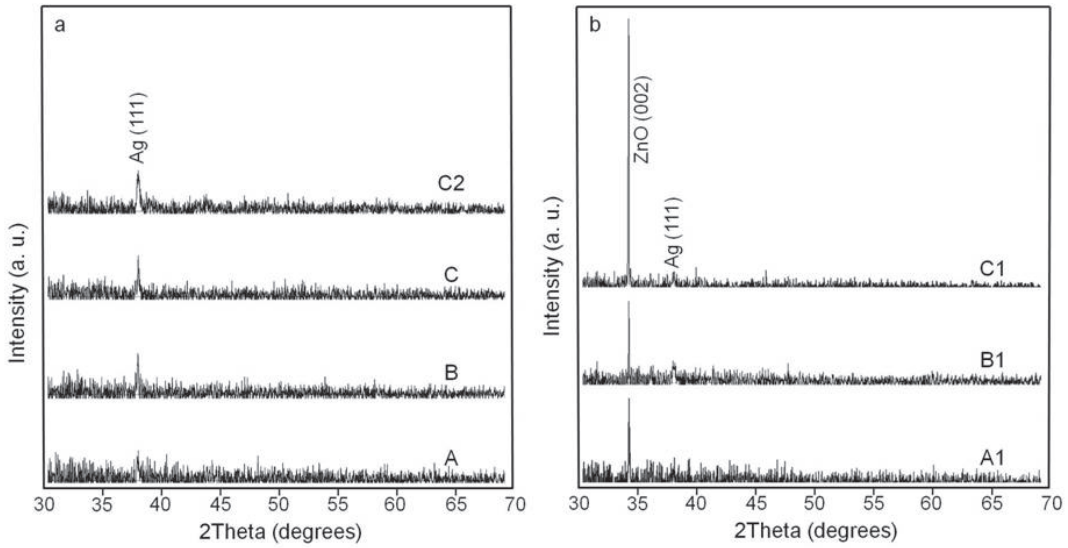

Figure 5.18: XRD Pattern of synthesized ZnO structures. (a) ZnO seed layers of A, B, and C types. C2 shows the pattern of the ZnO film grown on a C type seed layer, as explained in the text. (b) ZnO nanowires of A1, B1, and C1 types grown on seed layer of A, B, and C types, respectively, as explained in the text.

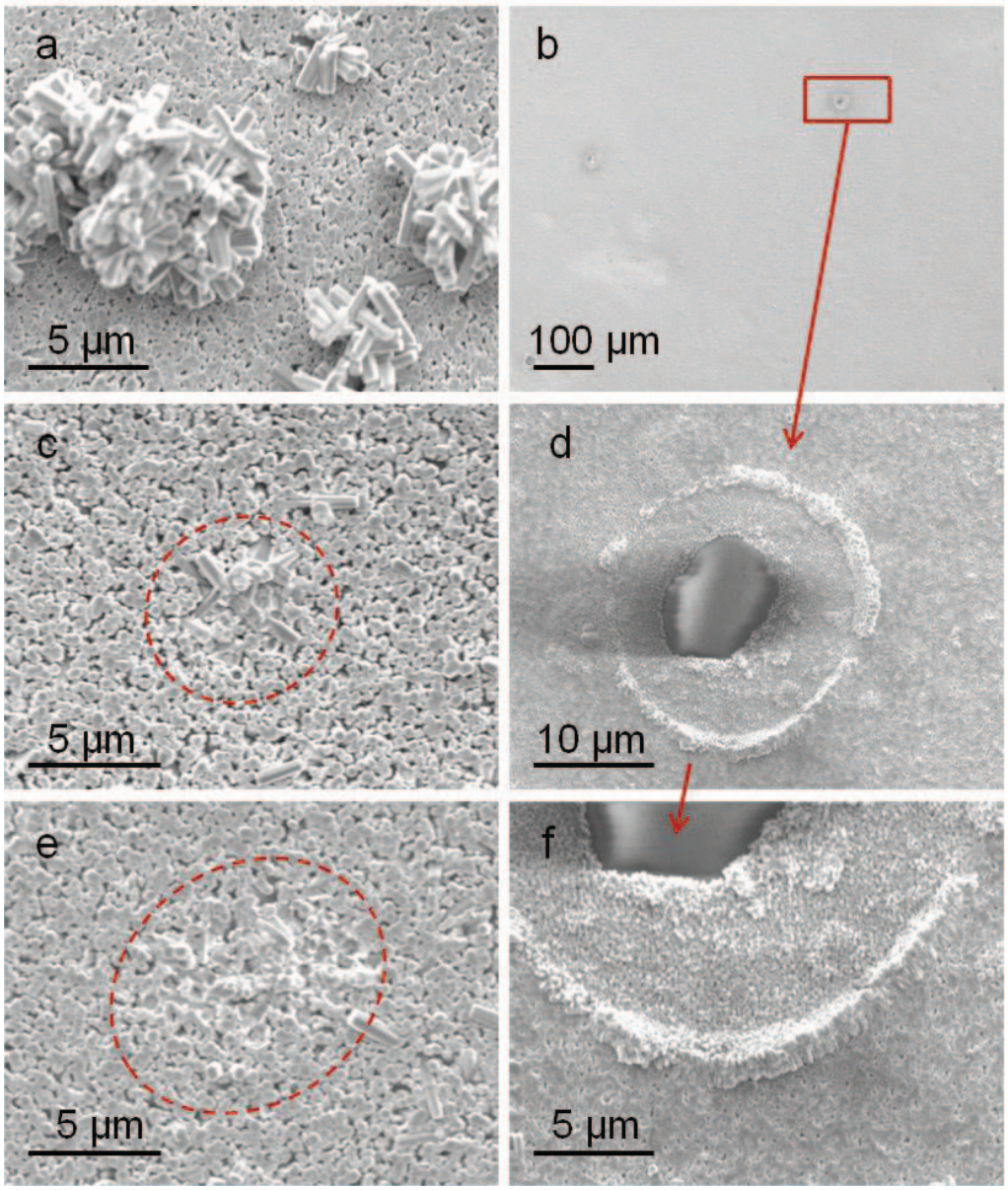

Figure 5.19: Influence of cleaning process on the synthesized ZnO film surface. (a) SEM images of typical ZnO clusters grown on the nanowire film surface. (b) and (c) The ZnO film after cleaning in distilled water in an ultrasonic cleaner for t=45 min. The red dashed circles show the trace of ZnO clusters cut off by the cleaning process. (d), (e) and (f) show some holes created on the ZnO film after t=55 min cleaning.

5.3 Characterization of fabricated nanogenerators

Because of the nature of the piezoelectric effect and the appearance of the piezoelectric potential under mechanical deformation in the single crystal form of ZnO, one expects no piezoelectric response from the amorphous seed layers and C2-type film. This can be deduced from their current-voltage transport properties. Clean glass substrates were coated with d=70 nm silver using the same sputtering method and served as top electrodes for the following measurements (see Figure 5.21 a). Under compressive uniaxial strain applied on the top electrode no measurable changes in the I-V response of the samples could be observed (Figures 5.20 a-d). However, for the vertically aligned nanowires of types A1, B1 and C1, the current, and therefore, the resistance of the samples changes with increasing compression as a result of the induced piezoelectric potential along the nanowires (Figures 5.21 b-d).

A comparison between the I-V curves of the ZnO seed layers shows the influence of the synthesis temperature on metal-semiconductor contacts. For the seed layers of A- and B-type, which were synthesized at lower temperature of T=80 ℃ the Ag-ZnO interface (see Figures 5.20 a and b) shows a symmetric and relative linear behavior (ohmic contact). The seed layer of C-type synthesized at T=90 ℃ has a very high resistance at the Ag-ZnO interfaces (see Figure 5.20 c). This can be related to high Schottky barriers at both top and bottom ends of the seed layer created naturally by built-in strain in the ZnO film during its fabrication [ZG09, YZ10]. The growth temperature can largely affect the growth morphology and deposition speed of ZnO nanoparticles in the solution on the Ag-coated glass substrates. Thus one can control the behavior of the metal-ZnO contact by controlling the growth temperature and change an ohmic contact into a Schottky one, or vice versa, by the same metal material for both electrodes. The synthesis temperature affects the transport property of the Ag-ZnO contact not only by the synthesis of ZnO seed layers but also by the growth of ZnO nanowires on the seed layers in the next step. A comparison between I-V curves of samples A1 and B1 (see Figures 5.21 b and c) shows that although in both samples the seed layers (see Figures 5.20 a and b) have an ohmic character, the metal-ZnO interfaces of the finally synthesized structures behave differently even when using the same Ag electrodes as before. The I-V curve of sample A1 shows still a symmetric and relatively ohmic-like behavior, even when it is uniaxially compressed. However, the I-V curve of sample B1 presents a symmetric diode character with no mechanical deformation (black curve in Figure 5.21 c) and an asymmetric and further

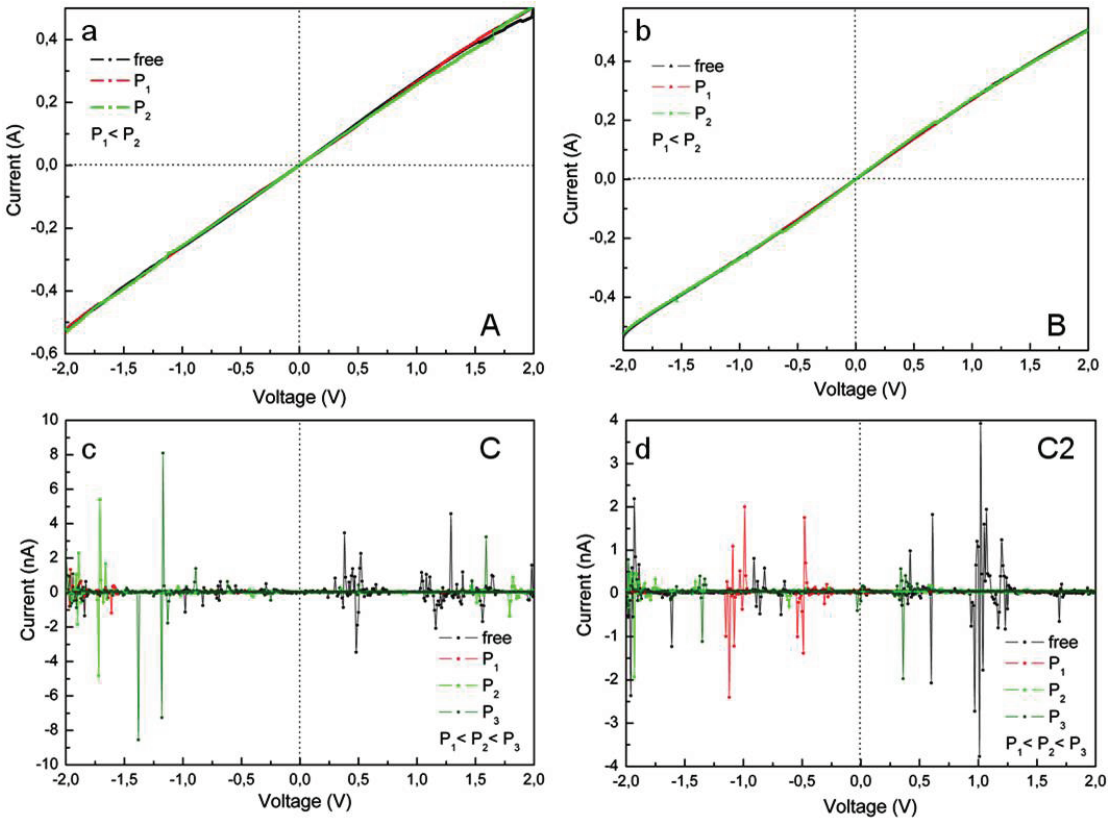

Figure 5.20: I-V curves of ZnO seed layers of (a) A, (b) B, and (c) C type synthesized by the wet chemical method. (d) shows the I-V curve of ZnO film of type C2 grown on a seed layer of type C, as explained in the text. Here P presents the normal pressure applied on the top surface of a seed layer.

rectifying behavior under uniaxial compression. The influence of the seed layer on the transport property of the final synthesized nanostructure can be seen from the I-V curves of sample B1 and C1 (Figures 5.21c and 5.21d), in which the nanowires were grown at the same temperature (T= 90 ℃) on the seed layers of type B and C with the (approximately) same thickness of 80 nm. The I-V curves of sample C1 (Figure 5.21 d) show an asymmetric and well rectifying behavior (Schottky contact), even without any mechanical deformation. A comparison between the black curves in Figures 5.21 c and d shows a symmetric diode contact in c and an asymmetric Schottky contact at the Ag-ZnO interfaces in d. This may be mainly caused by the transfer of the ohmic behavior to the Schottky-like behavior in the seed layers (see Figures 5.20 b and c) and might be influenced by the thickness of the

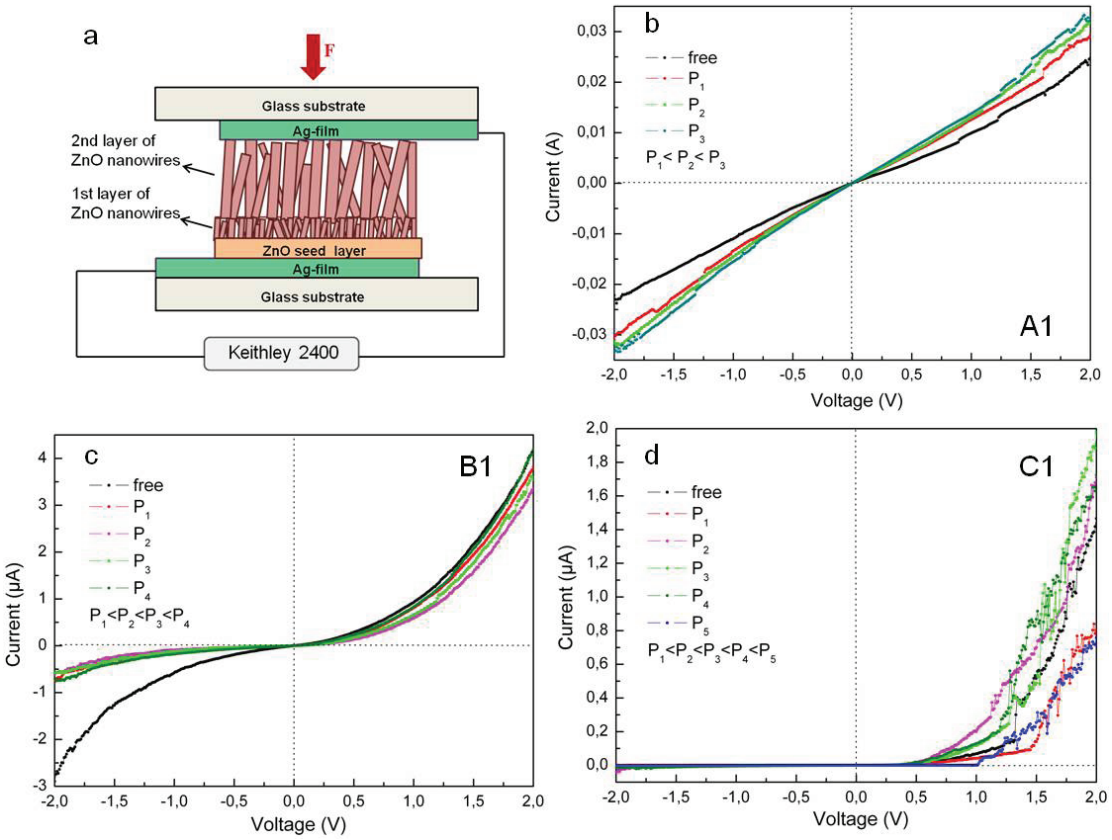

Figure 5.21: (a) Schematic diagram of fabricated ZnO nanogenerators and measurement setup. F presents a compressive uniaxial force applied on the top end of a nanogenerators (b), (c) and (d) show I-V curves of ZnO nanogenerator of A1, B1 and C1 type, respectively. Here P presents the uniaxial pressure applied on the top surface of a nanogenerator. P_1=14.7 Pa, P_2=29.4 Pa, P_3=44.1 Pa, P_4=58.8 Pa and P_5=73.5 Pa.

ZnO film in sample C1. The current-voltage measurements explained above indicate the possibility of controlling the transport property at the metal-ZnO interfaces for vertically aligned nanowires by controlling the electrical behavior of seed layers and controlling the synthesis process of ZnO nanowires. Moreover, one can use Ag or other metal materials, e.g. Cr, which possess work functions similar to that of ZnO, instead of expensive Au or Pt electrodes with their higher work function, to realize Schottky contacts at the metal-ZnO interfaces.

The as-fabricated samples A1, B1, and C1 can generate periodic piezoelectric current under applied periodic mechanical deformation. The measurement setup is schematically

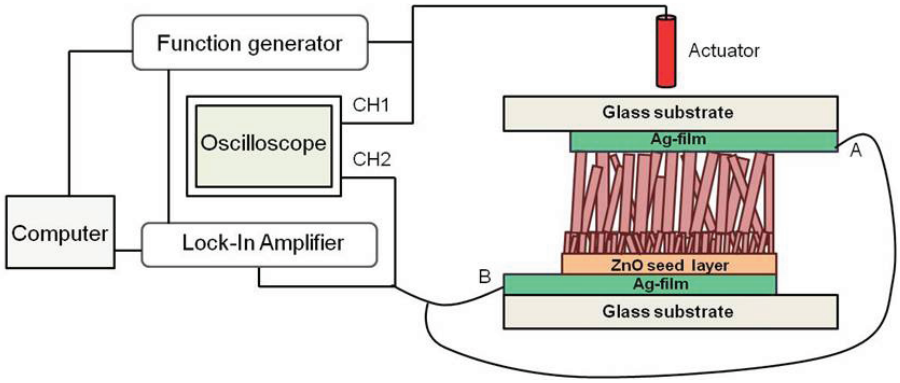

Figure 5.22: Schematic setup for measuring the piezoelectric current of fabricated ZnO nanogenerators.

shown in Figure 5.22. A Tektronix AFG3021 function generator was used to drive a piezoelectric actuator (Thorlabs, AE0203D08F) applying periodic uniaxial compressive strain on the top end of the nanogenerators. The piezoelectric current from the ZnO nanogenerators were measured at room temperature using a SR830 DSP lock-in amplifier (Stanford research systems). The compressive uniaxial strain creates a piezoelectric potential drop along the c-axis of ZnO nanowires, with the -c-axis side at a higher and the +c-axis side at a lower potential. In the nanogenerators the grown nanowires were highly dense (see Figures 5.14 a-b, 5.15 a-b, and 5.16 a-b). This suggests that shear stress at the interface between neighbor nanowires may contribute to the induced piezoelectric potential too. The maximal piezoelectric responses of the generators A1, B1 and C1 were observed at different frequencies as periodically compressed in a range of $\nu = 1$ Hz –100 kHz. These frequencies and the corresponding piezoelectric short-circuit current density of A1, B1 and C1 were measured as given in Table 5.3. The nanogenerator C1, in which the Ag-ZnO contacts showed a rectifying Schottky behavior (see Figure 5.20 d), generated the highest piezoelectric current. However, also the nanogenerator A1 with the symmetric ohmic-like Ag-ZnO contacts could generate a measurable piezoelectric current. This indicates that the Schottky contact is not a necessity for the operation of a ZnO nanogenerator, as believed until now. The Schottky contact leads only to a stronger piezoelectric response and a more effectively energy harvesting. Basically the generation of a piezoelectric signal in the external circuit does not require any conductive properties of the metal-piezoelectric material. Two main conditions must be fulfilled in order to transform the induced piezoelectric charge into a current/voltage signal [MA08]:

- The load resistance of the external circuit R_L (refer to Figure 5.12 in subsection 5.1.2) should necessarily be lower than the internal resistance of the piezoelectric generator R_P to avoid the charge transport through the generator itself.
- The capacitance of the readout circuit C_L should be equal to or smaller than the generator's capacitance C_P.

That means the time constant of the generator must be larger than the time constant of the external circuit to allow the external circuit to transform the induced piezoelectric charge into a signal before it is canceled by internal leakage. The internal resistance of the nanogenerator A1, B1 and C1 were about R_P=115 Ω, R_P=3.4 MΩ and R_P=3.6 GΩ measured using a Keithely 2400 source meter at very low applied voltage (U$\sim$ 10 mV). The external circuit resistor R_L was too small in our case ($R_L < 1\Omega$). Thus, even in the case of nanogenerator A1, the induced piezoelectric potential drove free electrons to flow effectively through the external circuit and not through the nanogenerator itself. However, in this case the generator had a small capacitance (as compared to the other ones) and therefore, could be charged rapidly, which resulted in a small current signal in the external circuit.

As mentioned already in subsection 5.1.2, the output signal of a nanogenerator may be affected by the measurement system. The change in the capacitance of the sample and or contact resistances might produce a signal when the sample is deformed. Thus the switching-polarity test should be done to differentiate a true output signal caused by the piezoelectric effect, from a false signal caused by the measurement system. All three nanogenerators A1, B1 and C1 passed this test. Figure 5.23 shows the result for nanogenerator B1 as an example by using an oscilloscope. The output signal (red signal) in Figure 5.23 measured by reversed connection is the reversal of that (blue signal) measured for forward connection. The difference in magnitudes observed under forward and reverse configurations is likely caused by a bias current in the measurement system, which is

Table 5.3: Maximal piezoelectric response of fabricated ZnO nanogenerators in the range of ν=1 Hz–100 kHz.

ZnO nanogenerator	ν (kHz)	I_{max}/A (µAcm^{-2})
A1	14.10	0.167
B1	17.17	0.458
C1	23.70	1.117

added to the generated piezoelectric current in the forward configuration, and subtracted from the generated piezoelectric current in the reverse configuration. Thus the true signal generated by the nanogenerator is the average of the magnitudes observed under forward and reverse configurations [RY09c].

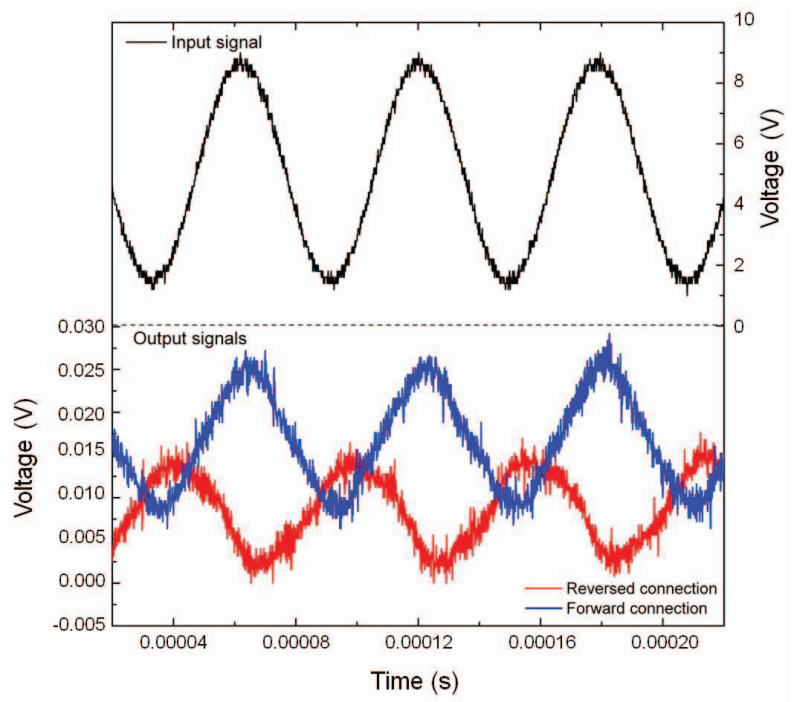

Figure 5.23: Switching-polarity test of the piezoelectric signal. The black signal shows the periodic uniaxial compressive strain (ν= 17170 Hz) applied on the ZnO nanogenerator of type B1. The blue and red signals show the corresponding piezoelectric output signals for (a) forward connection and (b) reversed connection, respectively.

With respect to above measurements one sees that as grown highly dense vertically aligned ZnO nanowires can be used to produce piezoelectric power under uniaxial deformations, in which Ag electrodes were used for both electrodes. As already discussed, the Schottky contact is not a necessity for the operation of a ZnO nanogenerator, but results only in a stronger piezoelectric response and a more effective energy harvesting. The maximal piezoelctric open-circuit voltage of U_{oc}=103 mV and short-circuit current density of I_{sc}/A=1.117 µAcm^{-2} were achieved by the nanogenerator C1 (P = 0.115 µWcm^{-2}). In this case the actuator, which was driven by a function generator at U=7 V, compressed

the nanowires periodically with a frequency of ν=23.7 kHz. Since piezoelectricity is a linear effect, the output signal of a single nanowire is linearly proportional to the magnitude of its deformation [YG07]. The ZnO nanowires in the nanogenerator C1 were all connected in parallel between the two electrodes (see Figure 5.16). Thus one expects that by increasing the pressing force acting on the nanowires, their deformation becomes larger, and the output signal is linearly scaled up. This can be seen in Figure 5.24. By increasing the driving voltage of the actuator, and therefore, increasing the magnitude of the uniaxial deformation, the output current density of the nanogenerator increased linearly.

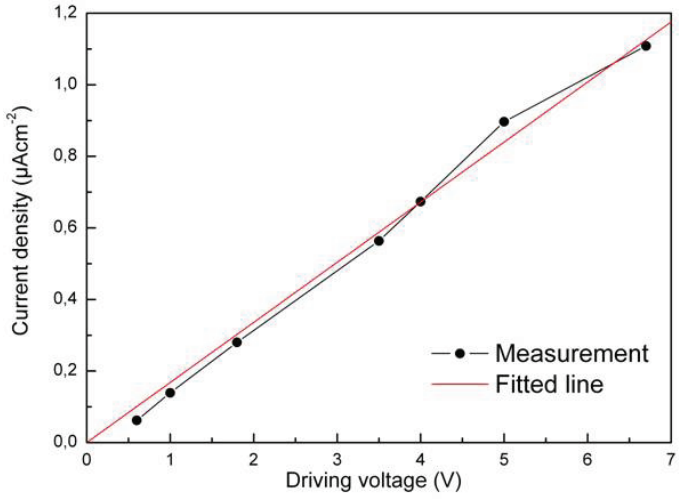

Figure 5.24: Linear dependency of the piezoelectric current on the uniaxial deformation applied on the nanogenerator C1. The horizontal axis shows the driving voltage of the actuator, which is linearly proportional to the applied uniaxial deformation, too.

By connecting more nanogenerators in parallel one can increase the output current. In addition, by connecting more nanogenerators in series, the output voltage can be increased too [XW07b, SX10, RY09b]. The voltage produced by the nanogenerator C1 is equal to the voltage produced by the individual ZnO nanowires between two electrodes. But, the output current from the nanogenerator is proportional to the number of its constituent nanowires. Thus, by synthesis of nanowires (of type C1) on wide metal-coated plates by the advanced wet chemical method and their integration to form a tandem generator one will achieve a significant output power, which may be enough to drive not only nanoscale wireless devices, but also devices in bulk dimensions. Moreover, since the ZnO nanowires

were grown using chemical synthesis at low temperaturs (T=90 ℃), this method should be applicable to growth on a large group of substrate materials. Therefore, the fields in which nanowires (of type C1) can be applied for energy harvesting purposes may be greatly expanded.

6 Conclusion and outlook

Zinc oxide (ZnO) is a II-VI compound semiconductor with abundant configuration in nanoscale structures. Because of its unique optical, electrical, mechanical, thermal and chemical properties ZnO, especially, in the form of nanostructures, offers tremendous potential in future applications in optoelectronic, piezotronic, piezophotonic, and magnetoelectronic devices. This work focused on the piezoelectric characteristic of ZnO nanostructures and its exploitation in two main fields: (I) modelling the growth of ZnO comblike-nanostructures, which are recently applied as nanocantilevers, UV nanolaser arrays, optical nanogratings and nanopolarizers, and (II) harvesting energy from the environment using aligned ZnO nanowire arrays, which is a promising means for self-powered and wireless nanodevices.

The studied ZnO nanostructures in this work were synthesized by three methods, which were available within the facilities at Clausthal University of Technology, including the vapor-liquid-solid (VLS), the electrochemicaldeposition (ECD), and the wet chemical methods. The VLS method was successfully manipulated for the synthesis of ZnO nanocombs. Using the molar ratio ZnO: C (2: 3) instead of the standard molar ratio (1: 1) by the VLS method, a high zinc vapor pressure can be achieved, which is essential for the growth of ZnO nanocombs. The ZnO nanocombs were then syntesized under temperature variations of T=953 ℃–T=1034 ℃ and T=961 ℃–T=1040 ℃. It seems that, beside high Zn vapor, the temperature variation has also an important role for the formation of nanocomb structures by the VLS method. However, a systematic study should be done to deeper understanding of the influence of the growth parameters on the morphology of nanocombs and, consequently to advance the functional devices based on the ZnO nanocomb structures mentioned above. In addition to the synthesis of ZnO nanocombs, a theoretical model for the formation of these structures based on the piezoelectric character of ZnO was developed. This model explains the periodic growth of nanowire branches of a nanocomb on the polar +(0001) surface of its backbone nanobelt as a self catalytic growth process. In this model, applying the perturbation and elasticity theory and using the

Fourier expansion of mechanical stress exerted in the material under the growth kinetics, the induced piezoelectric charge in the nanostructure is approximated. In fact, the periodic distribution of the induced piezoelectric charge is responsible for the periodic growth of nanowire branches of ZnO nanocombs on the polar +(0001) surface as a consequence of a self catalytic growth process. Some assumptions are taken in this model to simplify the analytical solution: (I) ZnO is in fact an anisotropic crystal with different elastic coefficients along its three crystal directions. But the ZnO nanobelt is approximated as an isotropic elastic material. (II) the polar ±(0001) surfaces introduce an intrinsic electric field (spontaneous polarization) inside of the ZnO nanobelt. This intrinsic electric field and its contribution to the coupling between mechanical field and electric field in the nanobelt is ignored. (III) Only the first two orders of the perturbation equations for the electromechanical coupling are solved. However, even with these assumptions the simulations for the ZnO nanocombs synthesized in this work showed a good agreement between experimental and theoretical results. Since the background theoretical knowledge can be important to control the growth process of nanocombs and, consequently to develop nanoscale functional devices based on them, it will be beneficial to extend this model for anisotropic ZnO by taking more orders of the electromechanical coupling in the nanostructure into account.

Due to its promising advantages over the other methods the wet chemical method for the advancement of ZnO nanogenerators was studied in more detail. The influence of the growth parameters on size, density, diameter distribution, and orientation of growing ZnO nanowires was studied. For using the synthesized ZnO nanowires as nanogenerators, the quality of the electric contact between the upper electrode and the synthesized ZnO surface is an important factor. For the wet chemical method, there are two possible processes that lead to worse contacts: the formation of ZnO clusters on top of the grown nanowire film, and a broad length distribution of grown nanowires. In this work, the wet chemical method was successfully developed for the synthesis of well-flat films of highly dense vertically aligned ZnO nanowires. Energy harvesting using these structures under uniaxial compressive strain was done, in which Ag electrodes were used for both electrodes. The possibility of controlling the transport property of the Ag-ZnO contacts by controlling the synthesis process of ZnO seed layers and nanowires was shown. One can effectively make Ohmic, diode, or schottky contacts at Ag-ZnO interfaces. Here the influence of the synthesis temperature and the synthesis time on the transport property of the ZnO seed layer and the final nanogenerator consisting of ZnO nanowires and Ag electrodes

was discussed. However, a systematic study should be done to investigate the influence of the other synthesis parameters like nanoparticle solution concentration, growth time of seed layer, and chemical solution concentration. In addition, it was indicated that the Schottky contact is not a necessity for the operation of a ZnO nanogenerator, as believed by now. However, the Schottky contact leads to a stronger piezoelectric response and a more effective energy harvesting.

Bibliography

[AK13] A. Kushwaha, M. Aslam, H. Tyagi: *AIP ADVANCES* (2013), Bd. 3: S. 042110

[AM95] A. Mang, S. Ruebenacke, K. Reimann: *Solid State Communications* (1995), Bd. 94(4): S. 251–254

[AR07] A. Rahm, T. Nobis G. Zimmermann M. Grundmann B. Fuhrmann F. Syrowatka, M. Lorenz: *Appl. Phys. A* (2007), Bd. 88: S. 31–34

[AZ02] A. Zaoui, W. Sekkal: *Phys. Rev. B*: *Condensed Matter* (2002), Bd. 66: S. 174106

[BBL97] B. B. Lakshmi, C. R. Martin, P. K. Dorhout: *Chem. Mater.* (1997), Bd. 9(3): S. 857–862

[BDY03] B. D. Yao, N. Wang, Y. F. Chan: *Appl. Phys. Lett.* (2003), Bd. 81: S. 757–760

[BJN03] B. J. Norris, J. F. Wager D. A. Kszler, J. Anderson: *J. Phys. D*: *Appl. Phys.* (2003), Bd. 36: S. L105

[BKM04] B. K. Meyer, D. M. Hofmann W. Kriegseis et al., H. Alves: *Phys. Stat. Sol. b* (2004), Bd. 241: S. 231–260

[BM03] B. Meyer, D. Marx: *Phys. Rev. B* (2003), Bd. 67: S. 035403

[Boe08] Boerner, S.: *ZnO-Nanodraehte zur Modifizierung von Evaneszenzfeldsensoren und der Entwicklung neuartiger Solarzellen*, Dissertation, Technische Universitaet Clausthal (2008)

[BP08] B. Postels, H. H. Wehmann M. Suleiman T. Weimann P. Hinze A. Waag, A. Bakin: *Appl. Phys. A* (2008), Bd. 91: S. 595–599

[BPZ03] B. P. Zhang, Y. Segawa K. Wakatsuki N. Usami, N. T. Binh: *Appl. Phys. Lett.* (2003), Bd. 83(8): S. 1635–1637

[BSK05] B. S. Kang, Y. W. Heo L. C. Tien D. P. Norton S. J. Pearton, F. Ren: *Appl. Phys. Lett.* (2005), Bd. 86(11): S. 112105

[CJL02] C. J. Lee, S. C. Lyu Y. Zhang H. Ruh H. J. Lee, T. J. Lee: *Appl. Phys. Lett.* (2002), Bd. 81: S. 3648

[CL03] C. Liu, Y. Yao X. Meng C. S. Lee S. Fan Y. Lifshitz S. T. Lee, J. A. Zapien: *Adv. Mater.* (2003), Bd. 15: S. 838

[CLH12] C. L. Hsu, K. C. Chen: *J. Phys. Chem. C* (2012), Bd. 116: S. 9351–9355

[Coo62] Cooper, J.: *Nature* (1962), Bd. 194: S. 269–271

[DCR99] D. C. Reynolds, B. Jogai C. W. Litton G. Cantwell W. C. Harsch, D. C. Look: *Phys. Rev. B: Condensed Matter* (1999), Bd. 60: S. 2340

[Des98] Desgreniers, S.: *Phys. Rev. B: Condensed Matter* (1998), Bd. 58: S. 14102–14105

[DFP00] D. F. Paraguay, J. Morales J. Solis L. W. Estrada, M. Miki-Yoshida: *Thin Solid Films* (2000), Bd. 373: S. 137

[DG03] D. Gruber, J.Mueller, F. Kraus: *Sens. Actuators B* (2003), Bd. 92: S. 81

[Dha06] Dhananjay, S. B. Krupanidhi, J. Nagaraju: *J. Appl. Phys.* (2006), Bd. 99: S. 034105

[DP10] D. Pradhan, K. T. Leung, F. Niroui: *ACS Appl. Mater. Interfaces* (2010), Bd. 2(8): S. 2409–2412

[ECG04] E. C. Greyson, T. W. Odom, Y. Babayan: *Adv. Mater.* (2004), Bd. 16(15): S. 1348–1352

[FFC13a] F. F. Comjani, S. Kontermann W. Schade, U. Willer: *Phys. Status Solidi A* (2013), Bd. 210(10): S. 2219–2223

[FFC13b] F. Fattahi-Comjani, S. Kontermann W. Schade, U. Willer: *AIP ADVANCES* (2013), Bd. 3: S. 102102

[FFC14] F. Fattahi Comjani, S. Kontermann W. Schade, U. Willer: *Appl. Phys. Lett.* (2014), Bd. 104: S. 143113

[GPZ07] G. P. Zhu, X. F. Wu Y. Yang X. W. Sun Y. P. Cui, C. X. Xu: *Journal of Electronic Materials* (2007), Bd. 36(4): S. 494–497

[GZ10] G. Zhu, S. Wang Z. L. Wang, R. Yang: *Nano Lett.* (2010), Bd. 10: S. 3151–3155

[GZ12] G. Zhu, S. Wang R. Yang Y. Ding X. Wang Y. Bando Z. L. Wang, Y. Zhou: *Nanotechnology* (2012), Bd. 23: S. 055604

[GZS06] G. Z. Shen, B. D. Liu D. Golberg C. J. Lee, Y. Bando: *Adv. Funct. Mater.* (2006), Bd. 16: S. 410–416

[HC02] H. Chik, S. G. Cloutier N. Kouklin J. M. Xu, J. Liang: *Appl. Phys. Lett.* (2002), Bd. 84: S. 3376

[Hei10] Heinz, P. D.: *First Principles Study of Thermoelectric Properties of Zinc Oxide Nanowires*, Dissertation, Texas State University-San Marcos (2010)

[HJF04] H. J. Fan, W. Lee K. Nielsch R. Scholz M. Zacharias U. Goesele A. Dadgar A. Krost, F. Fleischer: *Supperlattice Microst.* (2004), Bd. 36: S. 95

[HK96] H. Karzel, M. Koefferlein W. Schiessl M. Steiner et al., W. Potzel: *Phys. Rev. B: Condensed Matter* (1996), Bd. 53: S. 11425–11438

[HM09] H. Morkoc, Ue. Oezguer: *Zinc Oxide : Fundamentals, Materials and Device Technology*, Wiley-VCH Verlag GmbH and Co. KGaA : Weinheim (2009)

[HS01] H. Saeki, T. Kawai, H. Tabata: *Solid State Commun.* (2001), Bd. 120: S. 439–443

[HWR03] H.-W. Ryu, S. A. Akbar W.-S. Lee K.-J. Hong Y.-Jin Seo D.-C. Shin J.-S. Park G.-P. Choi, B.-S. Park: *Sens. Actuator B* (2003), Bd. 96: S. 717

[HY03] H. Yan, J. Johnson M. Law R. J. Saykally P. Yang, R. He: *J. Am. Chem. Soc.* (2003), Bd. 125: S. 4728

[Ike90] Ikeda, T.: *Fundamentals of Piezoelecticity*, Oxford University Press: Oxford (1990)

[JBB06] J. B. Baxter, K. V. Ommering E. S. Aydil, A. M. Walker: *Nanotechnology* (2006), Bd. 17: S. S304–S312

[JCJ03] J. C. Johnson, P. Yang R. J. Saykalley, H. Yan: *J. Phys. Chem. B* (2003), Bd. 107: S. 8816

[JDP08] J. D. Prades, F. H.-Ramirez L. F.-Romero T. Andreu et al., R. J.-Diaz: *J. Phys. Chem. C* (2008), Bd. 112: S. 14639–14644

[JE07] J. Elias, C. Levy-Clement, R. Tena-Zaera: *Thin Solid Films* (2007), Bd. 515: S. 8553–8557

[JE08] J. Elias, C. Levy-Clement, R. Tena-Zaera: *J. Electroanal. Chem.* (2008), Bd. 621: S. 171–177

[JEJ00] J. E. Jaffe, Z. Lin-A. C. Hess, J. A. Snyder: *Phys. Rev. B: Condensed Matter* (2000), Bd. 62: S. 1660

[JHP04] J. H. Park, Y. J. Choi S. H. Sohn J. G. Park, H. J. Choi: *J. Mater. Chem* (2004), Bd. 14: S. 35

[JJW02] J. J. Wu, S. C. Liu: *J. Phys. Chem. B* (2002), Bd. 106: S. 9546–9551

[JL08a] J. Liu, J. Song X. Wang C. Lao R. Tummala Z. L. Wang, P. Fei: *Nano Lett.* (2008), Bd. 8(1): S. 328–332

[JL08b] J. Liu, J. Zhou R. Tummala Z. L. Wang, P. Fei: *Appl. Phys. Lett.* (2008), Bd. 92: S. 173105

[JMR98] J. M. Recio, V. Luana R. Pandey L. Gerward J. S. Olsen, M. A. Blanco: *Phys. Rev. B: Condensed Matter and Materials Physics* (1998), Bd. 58: S. 8949–8954

[JN03] J. Nishii, S. Takagi T. Aita K. Saikusa Y. Ohmaki et al., F. M. Hossain: *Jpn. J. Appl. Phys.* (2003), Bd. 42: S. L347

[JS05] J. Song, E. Riedo Z. L. Wang, X. Wang: *J. Phys. Chem. B* (2005), Bd. 109(20): S. 9869–9872

[JXW06] J. X. Wang, Y. Yang H. Huang Y. C. Lee O. K. Tan-L. Vayssieres, X. W. Sun: *Nanotechnology* (2006), Bd. 17: S. 4995–4998

[KK04] K. Keem, G. T. Kim J. S. Lee B. Min K. Cho M. Y. Sung S. Kim, H. Kim: *Appl. Phys. Lett.* (2004), Bd. 84: S. 4376

[KM10] K. Momeni, R. S. Yassar, G. M. Odegard: *J. Appl. Phys.* (2010), Bd. 108: S. 114303

[KO03] K. Ogata, S. Fujita S. Fujita, K. Maejima: *J. Cryst. Growth* (2003), Bd. 248: S. 25–30

[KPD91] K. P. Donnell, X. Chen: *Appl. Phys. Lett.* (1991), Bd. 58(25): S. 2924–2926

[KY08a] K. Yu, J. Wu L. Li Y. Xu S. Huang Z. Zhu, Q. Zhang: *Nano Res.* (2008), Bd. 1: S. 221

[KY08b] K. Yu, J. Wu L. Li Y. Xu S. Huang Z. Zhu, Q. Zhang: *Nano Res.* (2008), Bd. 1: S. 221–228

[Lan05] Lang, S. B.: *Phys. Today* (2005), Bd. 58: S. 31–36

[LJB11] L. J. Brillson, Y. Lu: *J. Appl. Phys.* (2011), Bd. 109: S. 121301

[MA08] M. Alexe, M. A. Schubert D. Hesse U. Goesele, S. Senz: *Adv. Mater.* (2008), Bd. 20: S. 4021–4026

[MG08] M. Guo, M. Zhang Y. J. Zhang T. Ma X. D. Wang X. D. Wang, C. Y. Yang: *Electrochimica Acta* (2008), Bd. 53: S. 4633–4641

[MHH01a] M. H. Huang, H. Feick H. Yan Y. Wu H. Kind E. Weber R. Russo P. Yang, S. Mao: *Science* (2001), Bd. 292: S. 1897

[MHH01b] M. H. Huang, H. Feick N. Tran E. Weber P. Yang, Y. Wu: *Adv. Mater.* (2001), Bd. 13: S. 113–116

[MHZ04] M. H. Zhao, S. X. Mao, Z. L. Wang: *Nano Lett.* (2004), Bd. 4(4): S. 587–590

[MJ99] M. Joseph, T. Kawai, H. Tabata: *Appl. Phys. Lett.* (1999), Bd. 74(17): S. 2534–2536

[Mr10] M. riaz, O. Nur Z. L. Wang M. Willander, J. Song: *Adv. Funct. Mater.* (2010), Bd. xx: S. 1–6

[NKR07] N. K. Reddy, J. H. Kim M. Devika Y. B. Hahn, Q. Ahsanulhaq: *Nanotechnology* (2007), Bd. 18: S. 445710

[OD02] O. Dulub, U. Diebold, L. A. Boatner: *Surface Science* (2002), Bd. 519: S. 201–217

[OL10] O. Lupana, I .M. Tiginyanub V. V. Ursakib L. Chowc H. Heinrichc T. Pauportea, V. M. Guerina: *Journal of Photochemistry and Photobiology A: Chemistry* (2010), Bd. 211: S. 65–73

[PS03] P. Sharma, K. V. Rao F. J. Owens R. Sharma R. Ahuja J. M. Osorio B. Johansson-G. A. Gehring, A. Gupta: *Nat. Mater.* (2003), Bd. 2: S. 673

[PXG03] P. X. Gao, Z. L. Wang, Y. Ding: *Nano Lett.* (2003), Bd. 3(9): S. 1315–1320

[PY02] P. Yang, S. Mao R. Russo J. Johnson R. Saykally N. Morris J. Pham R. He H. J. Choi, H. Yan: *Adv. Funct. Mater.* (2002), Bd. 12: S. 323–331

[QL10] Q. Li, J. Sun J. Wang Y. Luo K. Sun D. Yu, J. Bian: *Applied Surface Science* (2010), Bd. 256: S. 1698–1702

[REM06] R. E. Marotti, G. Machado E. A. Dalchiele, P. Giorgi: *Solar Energy Materials and Solar Cells* (2006), Bd. 90: S. 2356–2361

[RFZ08] R. F. Zhuo, Q. Liang et al., H. T. Feng: *J. Phys. D: Appl. Phys.* (2008), Bd. 41: S. 185405

[RY09a] R. Yang, C. Li G. Zhu Z. L. Wang, Y. Qin: *Nano Lett.* (2009), Bd. 9: S. 1201

[RY09b] R. Yang, C. Li L. Dai Z. L. Wang, Y. Qin: *Appl. Phys. Lett.* (2009), Bd. 94: S. 022905

[RY09c] R. Yang, L. Dai Z. L. Wang, Y. Qin: *Nature Nanotechnology* (2009), Bd. 4: S. 34–39

[SKK03] S. K. Kim, C. R. Cho, S. Y. Jeong: *Appl. Phys. Lett.* (2003), Bd. 82: S. 562

[SPT70] S. P. Timoshenko, J. N. Goodier: *Theory of Elasticity*, Mac Graw-Hill Book Co.: New York, 7 Aufl. (1970)

[SX10] S. Xu, C. Xu Y. Wei R. Yang Z. L. Wang, Y. Qin: *Nature Nanotechnology* (2010), Bd. 5: S. 366–373

[SXM03] S. X. Mao, M. Zhao: *Appl. Phys. Lett.* (2003), Bd. 83: S. 993–995

[SYL03] S. Y. Li, T. Y. Tseng, C. Y. Lee: *Journal of Crystal Growth* (2003), Bd. 247: S. 357

[TP06] T. Pauporte, B. Viana F. Pelle, D. Lincot: *Appl. Phys. Lett.* (2006), Bd. 89: S. 233112

[TX12] T. Xu, M. He J. Li, P. Ji: *J. Nanomater.* (2012), Bd. 2012: S. 797935

[VS03] V. Staemmler, B. Meyer D. Marx M. Kunat S. G. Girol U. Burghaus Ch. Woell, K. Fink: *Phys. Rev. Lett.* (2003), Bd. 90: S. 106102

[Wan04] Wang, Z. L.: *J. Phys.: Condens. Matter* (2004), Bd. 16: S. R829–R858

[Wan07] Wang, Z. L.: *Appl. Phys. A* (2007), Bd. 88: S. 7–15

[WJM02] W. J. Moon, G. M. Choi, J. H. Yu: *Sens. Actuators B* (2002), Bd. 87: S. 464

[WYW11] W. Y. Weng, C. L. Hsu T. J. Hsueh, S. J. Chang: *ACS Appl. Mater. Interfaces* (2011), Bd. 3(2): S. 162–166

[XF08] X. Fang, U. K. Gautam C. Ye D. Golberg, Y. Bando: *J. Mater. Chem* (2008), Bd. 18: S. 509–522

[XF10] X. Fang, C. Ye L. Zhang, L. Hu: *Pure Appl. Chem.* (2010), Bd. 82(11): S. 2185–2198

[XW07a] X. Wang, J. Liu Z. L. Wang, J. Song: *Science* (2007), Bd. 316: S. 102–105

[XW07b] X. Wang, J. Song Z. L. Wang, J. Liu: *Nano Lett.* (2007), Bd. 7(8): S. 2475–2479

[XYK03] X. Y. Kong, Z. L. Wang: *Nano Lett.* (2003), Bd. 3(12): S. 1625

[YFH10] Y. F. Hu, Y. L. Chang R. L. Snyder Z. L. Wang, Y. Zhang: *ACS Nano* (2010), Bd. 4: S. 4220–4224

[YG07] Y. Gao, Z. L. Wang: *Nano Lett.* (2007), Bd. 7(8): S. 2499–2505

[YG09] Y. Gao, Z. L. Wang: *Nano Lett.* (2009), Bd. 9(3): S. 1103–1110

[YH10] Y. Hu, C. Xu G. Zhu Z. L. Wang, Y. Zhang: *Nano Lett.* (2010), Bd. 10: S. 5025–5031

[YH11] Y. Hu, C. Xu L. Lin R. L. Snyder Z. L. Wang, Y. Zhang: *Nano Lett.* (2011), Bd. 11: S. 2572–2577

[YHL04] Y. H. Leung, J. Gao M. H. Xie Z. F. Wei S. J. Xu W. K. Chan, A. B. Djurisic: *Chem. Phys. Lett.* (2004), Bd. 394: S. 452

[YI92] Y. Ito, H. Kanada H. Takeuchi H. Sugawara H. Onozato, K. Kushida: *Ferroelectrics* (1992), Bd. 134: S. 325–330

[YI95] Y. Ito, K. Sugawara H. Takeuchi, K. Kushida: *IEEE Trans. Ultrasonics, Ferroelectrics, and Frequency Control* (1995), Bd. 42: S. 316–324

[YQ08] Y. Qin, Z. L. Wang, X. Wang: *Nature* (2008), Bd. 451: S. 809–813

[YSL06] Y. S. Lim, S. T. Hong J. Kim, J. W. Park: *Materials Science and Engineering B* (2006), Bd. 129: S. 100–103

[YX09] Y. Xi, S. Xu R. S. Yang Z. Y. Gao C. G. Hu Z. L. Wang, J. H. Song: *J. Mater. Chem.* (2009), Bd. 19: S. 9260–9264

[YY12] Y. Yang, K. C. Pradel G. Zhu Y. Zhou Y. Zhang Y. Hu L. Lin Z. L. Wang, W. Guo: *Nano Lett.* (2012): S. A–F

[YZ10] Y. Zhang, S. Xiang Z. L. Wang, Y. Hu: *Appl. Phys. Lett.* (2010), Bd. 97: S. 033509

[ZG09] Z. Gao, Y. Gu P. Fei Y. Hao G. Bao Z. L. Wang, J. Zhou: *J. Appl. Phys.* (2009), Bd. 105: S. 113707

[ZLW03] Z. L. Wang, J. M. Zuo, X. Y. Kong: *Phys. Rev. Lett.* (2003), Bd. 91: S. 185502

[ZLW06] Z. L. Wang, J. Song: *Science* (2006), Bd. 312: S. 242–245

[ZWP05] Z. W. Pan, S. Dai D. H. Lowndes, S. M. Mahurin: *Nano Lett.* (2005), Bd. 5(4): S. 723–727

Acknowledgment

Here I would like to take this opportunity to thank all those who have helped me during the last few years for this work.

I would particularly like to thank my supervisor Prof. Dr. Wolfgang Schade for his scientific support and advice during my PhD studies and also for giving me the opportunity to present my own ideas and work on them. I would also like to thank him for providing me a flexible working time, especially during the early years of birth of my child.

I would like to thank Prof. Dr. Daniel Schaadt for the acceptance of the judgment of this work and his friendly assistance.

My especial thank belongs to Dr. Ulrike Willer for her valuable advices and discussions during all these years as well as for the correction of my thesis. I would like to thank Dr. Stefan Kontermann for his support and helpful discussions.

I wish to express my gratitude to all my colleagues for the nice working atmosphere, instructive discussions and their technical support in experiments, especially Julia Waltermann, Kay-Michael Guenther, Michael Koehring, Wolfgang Schippers, Mario Mordmueller and the former colleagues Sandra Boerner and Claus Romano. I am also grateful to Prof. Dr.-Ing. Holger Fritze and his working team, especially Silja Schmidtchen, Frank kuewen, Anke Weidenfelder, Hendrik Wulfmeier and Samir Hammadi for the friendly support by using their Laboratory Equipments. I would like to thank Dr. Gerhard Lilienkamp in the working group ″Physics of surfaces and interfaces″and Prof. Dr.- Ing. Stefan Hartmann in ″Institut of Applied Mechanics″for helpful discussions and friendly assistance.

My last but most profound thank belongs to my husband Arash Momeni who always, especially at stress times, stood with words and deeds beside me.

Eidesstattliche Erklärung

Hiermit erkläre ich an Eides Statt, dass ich die bei der Fakultät für Natur- und Materialwissenschaften der Technischen Universität Clausthal eingereichte Dissertation selbständig und ohne unerlaubte Hilfe verfasst und die benutzten Hilfsmittel vollständig angegeben habe.

Clausthal-Zellerfeld, den 27.02.2014

Farzaneh Fattahi Comjani

Hiermit erkläre ich an Eides Statt, dass die eingereichte Dissertation weder in Teilen noch in Ihrer Gesamtheit einer anderen Hochschule zur Begutachtung vorliegt oder vorgelegen hat und dass ich bisher noch keinen Promotionsversuch unternommen habe.

Clausthal-Zellerfeld, den 27.02.2014

Farzaneh Fattahi Comjani